Impact of Dwell Times and Lower Potential Limit During Voltage Cycling on PEM Fuel Cell Catalyst Durability

by

Elaheh Hantoosh Zadeh

B.Sc., Sharif University of Technology, 2019

Thesis Submitted in Partial Fulfillment of the
Requirements for the Degree of
Master of Applied Science

in the
School of Sustainable Energy Engineering
Faculty of Applied Sciences

SIMON FRASER UNIVERSITY
Summer 2024

Declaration of Committee

Name:	**Elaheh Hantoosh Zadeh**
Degree:	**Master of Applied Science**
Title:	**Impact of Dwell Times and Lower Potential Limit During Voltage Cycling on PEM Fuel Cell Catalyst Durability**
Committee:	**Chair:** **Mina Xu** Lecturer, Sustainable Energy Engineering
	Erik Kjeang Supervisor Professor, Mechatronic Systems Engineering
	Colin Copeland Committee Member Associate Professor, Sustainable Energy Engineering
	Vahid Hosseini Examiner Associate Professor, Sustainable Energy Engineering

Abstract

The electrochemically active surface area (ECSA) loss of the cathode electrode remains a critical issue for proton exchange membrane (PEM) fuel cell durability in zero-emission transportation and stationary power applications. Here, cathode catalyst (Pt) degradation in fuel cells was systematically examined through eight square wave voltage cycling accelerated stress tests in H_2/air atmosphere, with varying lower potential limits (LPL) (0.6 and 0.8 V) and dwell times (3 and 10 s). ECSA loss was measured via cyclic voltammetry at the beginning of life and regular cycle intervals. The changes in the catalyst layer structural properties, including Pt particle size distribution and spatial re-distribution was visualized by electron microscopy. It was found that LPL had the greatest impact on ECSA loss due to different rate of oxide removal at various LPLs. Subsequently, longer dwell times at the upper potential limit (UPL) exhibited the most degradation through the anodic dissolution of Pt at high potentials. This was followed by ASTs with longer dwell times at LPL due to slower oxide removal rate at LPL of 0.8 V and enhanced Pt ion mobility for ASTs with prolonged dwell time at LPL of 0.6 V, which was confirmed by observing higher rate of Ostwald ripening and Pt loss into the membrane. These findings could help to better understand the complex underlying mechanisms of Pt degradation in PEMFCs.

Keywords: proton exchange membrane fuel cell (PEMFC); durability; platinum (Pt) degradation; cathode catalyst layer (CCL); hydrogen energy; electrochemical energy storage and conversion

This thesis is dedicated to my mother for her endless love and countless sacrifices for me, and to my father for the encouragement he has always given me throughout my life to pursue my dreams.

This thesis is also dedicated to my wonderful husband, Kiarash, for all his emotional support and for always being there to lift me up during challenging times.

Acknowledgements

First and foremost, I would like to express my deepest gratitude to my supervisor, Dr. Erik Kjeang, for giving me this opportunity, for his invaluable guidance, support, and insightful mentorship throughout the completion of this thesis.

I would also like to thank my committee member, Dr. Colin Copeland, for his valuable feedback on my thesis.

Special thanks to Dr. Mohammad Soroush Shojayian for sharing his expertise and many insightful conversations. I would also like to thank Dr. Paran Sarma, along with my FCReL colleagues Jonas Stoll and Dr. Erigene Bakangura, for all their help with my work. I would like to thank coop students Ji Jeong and Delin Ma for helping me with my experimental work.

This research was supported by the Natural Sciences and Engineering Research Council of Canada, Canada Research Chairs, and Simon Fraser University Community Trust Endowment Fund. Additionally, this work made use of the 4D LABS core facility at Simon Fraser University (SFU) supported by the Canada Foundation for Innovation (CFI), British Columbia Knowledge Development Fund (BCKDF), and Pacific Economic Development Canada (PacifiCan). I would also like to thank Bioimaging Facility at University of British Columbia for providing training in ultramicrotomy techniques.

Table of Contents

List of Tables

List of Figures

List of Acronyms

ACL	Anode Catalyst Layer
AST	Accelerated Stress Test
BOL	Beginning of Life
CCL	Cathode Catalyst Layer
CCM	Catalyst Coated Membrane
CL	Catalyst Layer
CV	Cyclic Voltammetry
DOE	See US DOE
ECSA	Electrochemically Active Surface Area
EDX	Energy Dispersive X-Ray
EIS	Electrochemical Impedance Spectroscopy
EOL	End of Life
EOT	End of Test
FCEVs	Fuel Cell Electric Vehicles
FCReL	Fuel Cell Research Lab
GDE	Gas Diffusion Electrode
GDL	Gas Diffusion Layer
GDM	Gas Diffusion Medium
GHG	Greenhouse Gas
HDV	Heavy Duty Vehicle
HOR	Hydrogen Oxidation Reaction
HRTEM	High Resolution Transmission Electron Microscopy
LCA	Life Cycle Assessment
LDV	Light Duty Vehicle
LPL	Lower Potential Limit
MEA	Membrane Electrode Assembly
MPL	Micro Porous Layer
NREL	See US NREL
OCV	Open Circuit Voltage

ORR	Oxygen Reduction Reaction
PEM	Proton Exchange Membrane
PEMFC	Proton Exchange Membrane Fuel Cell
PSD	Particle Size Distribution
PTFE	Per Sulfonated Polytetrafluoroethylene
Pt	Platinum
Pt/C	Platinum on Carbon
RH	Relative Humidity
SEM	Scanning Electron Microscopy
SHE	Standard Hydrogen Electrode
SLPM	Standard Liter Per Minute
STEM	Scanning Transmission Electron Microscopy
STEM-BF	Scanning Transmission Electron Microscopy Bright Field
TEM	Transmission Electron Microscopy
UNFCCC	United Nations Framework Convention on Climate Change
UPL	Upper Potential Limit
US DOE	United States Department of Energy
US NREL	United States National Renewable Energy Laboratory
VOC	Volatile Organic Compound

Chapter 1.

Introduction

In recent years, the urgency to address the environmental challenges facing our planet has become increasingly evident. From alarming reports by leading scientists (1) to global initiatives urging action (2), the need for sustainable solutions has never been more pressing. One of the critical issues at the forefront of this discourse is the proliferation of greenhouse gases (GHGs) and their detrimental effects on the Earth's climate system. GHGs trap heat in the Earth's atmosphere, leading to a rise in global temperature and disrupting ecosystems worldwide (3). Furthermore, the proliferation of GHGs has also been linked to various health problems, including respiratory illnesses, cardiovascular diseases, and increased susceptibility to heat-related ailments, posing significant risks to human well-being and public health (4). According to the United Nations Framework Convention on Climate Change (UNFCCC), carbon dioxide from the burning of fossil fuels stands out as the single largest source of greenhouse gas emissions resulting from human activities (5). The automotive industry represents a substantial contributor to carbon dioxide emissions, particularly through the combustion of fossil fuels in internal combustion engines (6). In the ongoing global effort to reduce carbon dioxide emissions, sustainable technologies like hydrogen fuel cells have emerged as promising alternatives to conventional combustion engines. However, while fuel cells present a pathway towards reducing greenhouse gas emissions, their widespread adoption is still impeded by the imperative for continuous enhancements in efficiency, durability, and cost-effectiveness. The research outlined in this thesis contributes to improving fuel cell technology by focusing on enhancing durability, particularly in the cathode electrode. Addressing degradation in the cathode electrode, which is one of the primary contributors to fuel cell lifespan, is paramount for realizing the full potential of fuel cell technology.

1.1. Proton Exchange Membrane Fuel Cells

Polymer electrolyte membrane fuel cells (PEMFCs), also called proton exchange membrane fuel cells, are the most promising and common type of fuel cells used in transportation and vehicle applications, such as cars, buses, and heavy-duty trucks (7). Proton exchange membrane (PEM) fuel cells deliver high power density and offer the

advantages of low weight and volume compared with other fuel cells (8). Additionally, PEM fuel cells operate at relatively low temperatures, around 80°C (176°F), which allows them to start quickly with less warm-up time (9).

In Figure 1.1 a schematic picture of a PEM fuel cell is illustrated. In the fuel cell reaction, hydrogen and oxygen/air are supplied to the anode and cathode, respectively, through the flow channels. These reactant gases then diffuse through the gas diffusion medium (GDM) and reach the anode catalyst layer (ACL) and cathode catalyst layer (CCL), respectively. On the ACL catalyst surface, the hydrogen oxidation reaction (HOR) occurs according to Equation 1.1. In this reaction, hydrogen molecules split into protons and electrons, with protons passing through the PEM electrolyte and electrons traveling through the external circuit. On the cathode side, the oxygen reduction reaction (ORR), Equation 1.2, takes place, where protons and electrons originating from the anode site, along with supplied oxygen molecules, converge at the CCL and combine to form water. The overall reaction occurring in the PEM fuel cell, which comes from sum of anode and cathode reactions is expressed in Equation 1.3. (10):

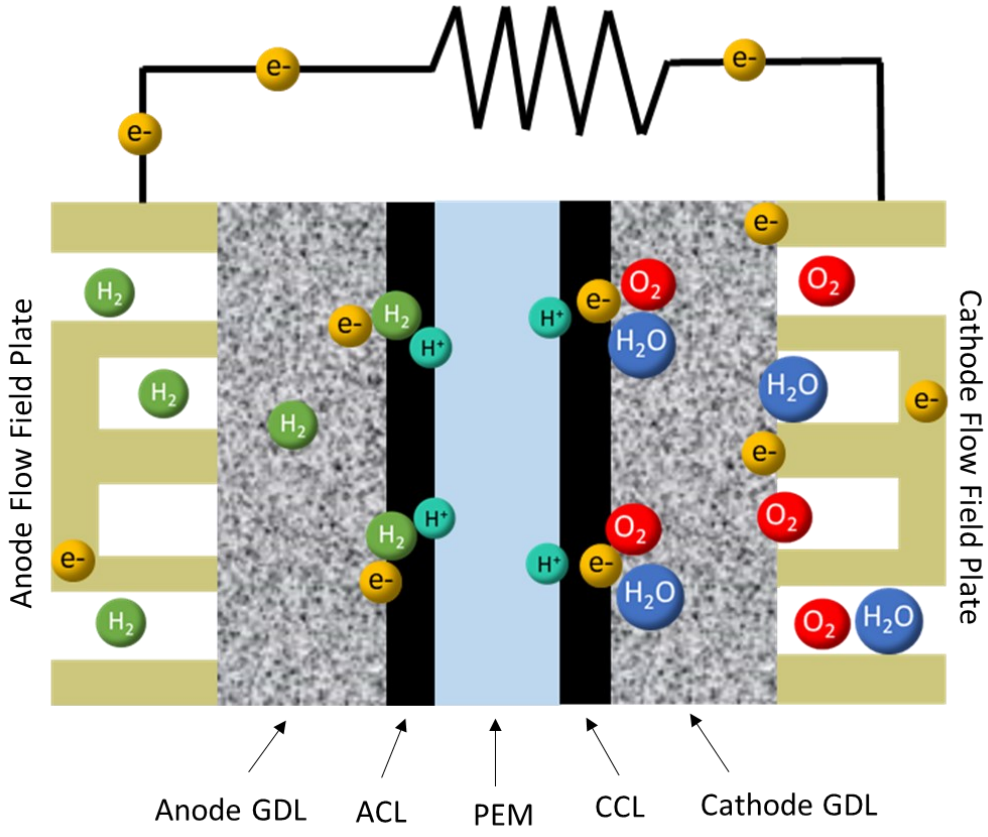

Figure 1.1. Schematic of a PEMFC

$$2H_2 \rightarrow 4H^+ + 4e^- \qquad E_0 = 0\ \text{V vs. SHE} \tag{1.1}$$

$$O_2 + 4H^+ + 4e^- \rightarrow 2H_2O \qquad E_0 = 1.23\ \text{V vs. SHE} \tag{1.2}$$

$$2H_2 + O_2 \rightarrow 2H_2O \tag{1.3}$$

The cell potential produced by the overall electrochemical reaction in PEM fuel cell is obtained from the difference between HOR and ORR standard potentials, as described in Equation 1.4:

$$E_{cell} = E_{cathode,red} - E_{anode,red} \tag{1.4}$$

According to the standard electrode potential table, the HOR is defined as the standard reference electrode, or standard hydrogen electrode (SHE), with a reduction potential of 0.00 V, and the standard potential for ORR is reported +1.23 V. Therefore, using Equation 1.4, the PEM fuel cell reversible voltage at standard-state (25°C and 1 bar) is equal to 1.23 V. In practice, however, various overpotentials, including open circuit voltage (OCV) losses, kinetic activation losses, ohmic losses and mass transport losses, reduce this theoretical voltage (10). Further discussion on these overpotentials will be provided in the Polarization Curve section.

1.1.1. Key Components and Functions

Proton Exchange Membrane

Proton exchange membrane that acts as an electrolyte locates in the center of the PEMFC. PEM conducts protons while is resistant to passing electrons and reactant gases, e.g., oxygen and hydrogen gases. The most common proton exchange membrane material used in fuel cell industry is perfluorosulfonic acid (PFSA) ionomer membranes, known as Nafion, due to their high proton conductivity (10). Generally, Nafion consists of a hydrophobic backbone structure like per sulfonated polytetrafluoroethylene (PTFE), along with perfluorinated side chains, which are ending in hydrophilic sulfonic acid groups ($–SO_3–H^+$) (11). In particular, the chemical structure of Nafion 211, which is used in this work, is shown in Figure 1.2 (12).

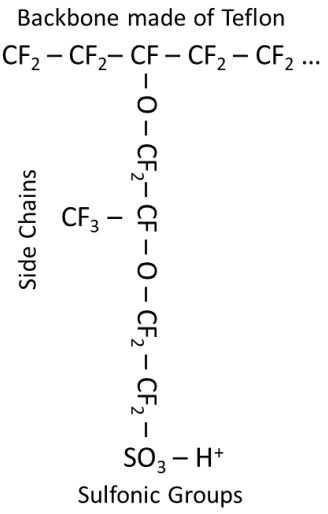

Figure 1.2. Chemical structure of Nafion

The fluoropolymer backbone imparts excellent chemical and mechanical properties to Nafion™, while the hydrophilic sulfonic acid-terminated side chains facilitate exceptional water absorption, resulting in high proton conductivity. Therefore, as conductivity and water content are strongly related, to ensure optimal proton conductivity in the PEM, it is crucial to maintain the membrane in a consistently hydrated state (10).

The durability of Nafion membranes is crucial for the long-term performance and reliability of PEMFCs. However, mechanical and chemical degradation mechanisms pose significant challenges to their stability under harsh operating conditions. Mechanical degradation encompasses issues such as mechanical stress, deformation, and loss of structural integrity that can be caused by relative humidity cycling and membrane dry out (13). Chemical degradation, on the other hand, involves processes such as oxidative attacks and chemical impurities (14). To address these challenges, researchers have been exploring innovative approaches involving both mechanical and chemical reinforcements. Mechanical reinforcements aim to enhance the membrane's mechanical properties, such as strength and toughness, through the incorporation of nanofillers and advanced fabrication techniques. Meanwhile, chemical reinforcements focus on improving chemical stability and resistance to degradation by introducing cross-linking agents, modifying surface properties, and developing novel polymerization methods (15). The most common reinforcements for Nafion membranes include carbon-based nanomaterials such as carbon nanotubes (CNTs) (16) and graphene oxide (GO) (17), as well as expanded polytetrafluoroethylene (ePTFE) (15).

Catalyst Layer

Catalyst layers (CLs) are positioned at both anode and cathode sides between membrane and gas diffusion media (GDM). CL is a porous medium consisting of catalyst particles that accelerate electrochemical reactions at the anode and cathode, and are supported by carbon particles, facilitating electron transport. Furthermore, the porous structure of CL allows access to reaction sites for reactant gases and facilitates the removal of the produced water. Additionally, ionomer is a essential part of catalyst layer for establishing a pathway for hydrogen protons from the membrane (18).

Currently, platinum nanoparticles, commonly found on carbon support, called platinum on carbon (Pt/C) are the most viable option for PEMFCs due to their superior activity compared to other pure metals (19). However, it is important to note that the significant cost associated with platinum, approximately 40% of the fuel cell stack cost (20,21), has prompted ongoing research efforts focused on minimizing platinum loading by making Pt alloys (22,23) and investigating alternative materials, such as ruthenium (24), palladium, and non-precious metals (25).

Gas Diffusion Layer

The gas diffusion layer (GDL), located between flow field plate and CL, is composed of two layers, a macro-porous substrate called gas diffusion medium (GDM) and Micro-Porous Layer (MPL). GDM and MPL are essential components in the structure of modern PEMFCs. The GDM typically is composed of materials like carbon paper or cloth, facilitating the transport of electrons, water, and reactants. Its macro-porous structure, consisting of conductive carbon fibers and a hydrophobic coating such as Teflon, allows for the uniform reactant distribution flow of reactant gases and efficient water management (26,27). On the other hand, the MPL, typically made of carbon nanoparticles, nanotubes, or nanofibers and PTFE, is strategically coated on the surface of the macro-porous substrate within the GDL (28). Its primary functions are to enhance the contact area between the GDM and the catalyst layer and improve liquid water management (29). Together, the GDM and MPL play integral roles in enhancing the efficiency and functionality of PEMFCs.

Flow Field Plates

Flow field plates play a crucial role in the operation of modern PEMFCs. Their primary function is to deliver fuel cell reactants, remove exhaust gases, and facilitate the movement of electrons from the carbon fibers of the gas diffusion media to the current collectors on the opposite side of the flow fields (30,31) . In fuel cell stacks composed of multiple cells, a single flow plate often serves as both the anode and cathode plate for adjacent cells, creating a bipolar plate with separate flow channels for each.

Bipolar plates, which can constitute over 80% of the total weight in a PEMFC stack, must meet stringent criteria, including high electrical conductivity, chemical and mechanical stability, robustness, impermeability to gases, and cost-effectiveness. Bipolar plates can be made from composite graphite, traditional pure graphite, or metals. Composite graphite plates, composed of graphite and a polymer, are cost-effective and easy to process but offer lower performance due to the inadequate electrical conductivity. Pure graphite plates have high electrical and thermal conductivity but are expensive and have poor mechanical properties. Metal plates, typically stainless steel or titanium, provide excellent conductivity and mechanical strength with established manufacturing techniques, but can be prone to corrosion, which could be improved with using corrosion-preventing coatings to some extent. Each material offers a balance of benefits and drawbacks, suited to different fuel cell applications (32).

The optimization of flow field design is essential for efficient and uniform delivery of reactants to the active cell area. While more complex designs exist, the industry generally favors simpler flow field patterns, such as parallel, serpentine, and interdigitated flow channels (33), as depicted in Figure 1.3, for their cost-effectiveness (34).

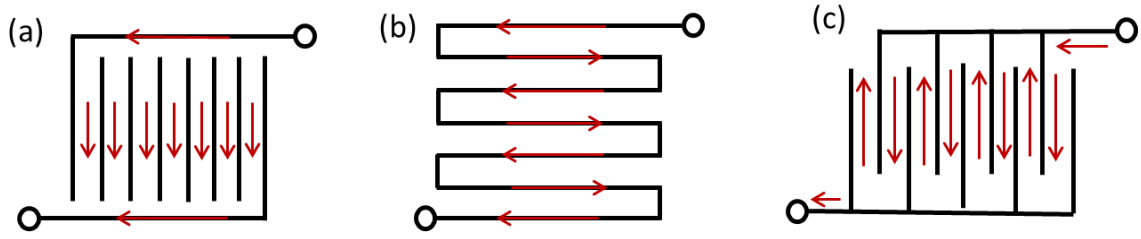

Figure 1.3. Common flow field designs: (a) parallel; (b) serpentine; and (c) interdigitated

1.1.2. Commercialization Challenges

PEMFCs have been applied across diverse sectors, with current major markets in transportation, stationary power, portable power, auxiliary units, backup power, and material handling. In the realm of transportation, manufacturers have started to introduce fuel cell electric vehicles (FCEVs) to the market. Presently, only two hydrogen FCEVs are available in the United States, and they are exclusively sold in California, where the majority of hydrogen refueling stations are located: the 2024 Hyundai Nexo compact crossover and the Toyota Mirai sedan. Despite these successes, the commercialization of PEMFCs in the automotive sector has been slow, primarily attributed to challenges in hydrogen infrastructure and therefore the lack of refueling stations (30). Due to the lack of hydrogen refueling stations for passenger cars, coupled with the declining costs of lithium-ion batteries, which make battery electric vehicles the dominant technology for light duty vehicles (LDVs), we can see a noticeable change in focus from light-duty to heavy-duty applications for PEMFCs in transportation industry. In fact, the advantages of fuel cells over batteries, including cost-effectiveness for extended driving ranges and faster refueling times, become more pronounced in heavy-duty and fleet applications.

However, the shift in focus from light- to heavy-duty vehicles exacerbates durability challenges for fuel cells. For instance, the fuel cell vehicle durability target in miles for HDVs is ca. six times greater than that for LDVs, highlighting the escalated durability requirement for HDV applications. In this regard, US DOE set the ultimate lifetime target for HDVs at 30,000 hours, while the corresponding target for LDVs is a mere 8,000 hours. Furthermore, in meeting peak efficiency requirements, the ultimate target for HDVs exceeds that of LDVs by 2%, with the benchmark set at 72% (35,36). US DOE has also recently published the cost status for 2021 and 2022 years, along with the durability-adjusted cost targets for HDV fuel cells. This data indicates the need to reduce the cost of HDV fuel cells by more than half, from \$179/kW_{net} in 2022 for a manufacturing volume of 50,000 systems/year to \$80/kW_{net} target at 100,000 systems/year by 2030 (37). As cost and durability are closely intertwined, meeting these targets to successfully commercialize PEMFC heavy duty vehicles requires substantially longer lifetimes and a four to five-fold enhancement in the durability of PEMFC stacks (35).

Durability

The degradation of fuel cells is attributed to several key factors, as identified by the US DOE, including membrane deterioration, loss of catalytic surface area, and carbon support corrosion (30). These factors significantly contribute to the reduction in fuel cell durability. Membrane degradation results from both chemical and mechanical stresses. Mechanical stresses, such as membrane swelling and shrinking, are induced by variations in humidity. Chemical degradation, on the other hand, stems from impurities in the fuel and oxidant, as well as the generation of hydrogen peroxide (H_2O_2). The byproducts of H_2O_2, including radicals like hydroxyl (OH) and hydroperoxyl (OOH), actively compromise the chemical structure of the membrane (18,38). The remaining two elements of fuel cell degradation contributors are associated to the fuel cell electrodes. Both the anode and cathode electrodes share similar components and materials. However, due to the slower occurrence of the oxygen reduction reaction on the cathode compared to the hydrogen oxidation reaction on the anode, the cathode electrode is usually attributed greater importance in durability issues (10). The degradation of the cathode electrode alone can contribute to 30-40% of overall fuel cell degradation (39). As a result, it is the subject of substantial studies, including the present study, and will therefore be explored in greater detail in the following section.

1.2. Cathode Electrode Degradation

The cathode electrode degradation results from a complicated interaction of various degradation mechanisms, which can be categorized into ionomer degradation, carbon support degradation and platinum catalyst degradation. Similar to Nafion membranes, the ionomer in the catalyst degrades by contaminants such as OH radicals and hydrogen peroxide, both of which are produced when fuel cell is under operation (40). The carbon support is damaged due to oxidation (or corrosion) of the carbon during start-up/shutdown, which occurs at the start of a trip and at the end of a trip, respectively. The carbon corrosion results in the damage to the carbon support structure, eventually leading to its collapse (40,41).

Lastly, the degradation of the Pt catalyst can occur due to poisoning caused by contaminants, such as carbon monoxide and sulfur, as well as the collapse and thinning of the carbon support that can contribute to the degradation of the catalyst layer since the

platinum particles it supports are compelled to undergo redistribution. Nevertheless, the main contributor to catalyst degradation is the agglomeration or growth of Pt particles. Agglomeration and growth occur because nanoparticles inherently tend to minimize their surface energy. As small particles attach to each other and constitute larger particles, their surface area decreases, leading to lower surface energy. In addition to this inherent tendency, particle growth will happen through dissolution and subsequent redeposition of Pt particle during load cycling, which are a result of acceleration and deceleration during vehicle operation. Throughout these load cycles, the fuel cell engine remains active, and the load demand changes depending on traffic conditions. This load variation leads to Pt catalyst dissolution through various mechanisms, which will be explained in detail in the next section.

1.2.1. Platinum Catalyst Degradation Mechanisms

During typical vehicle operation, when load cycles occur, there will be a rapid dynamic shift in cathode potential, which is known to make Pt electrochemically unstable. There are many fundamental studies which have proposed various models for Pt degradation during potential cycling. According to these studies, it is widely accepted that Pt will ionize with increasing potentials according to Equation 1.5. This is a common failure mechanism during voltage cycling which is known as **anodic dissolution** of Pt (42–48). The direction of the reactions depends on both the applied potential and the respective equilibrium potential of the reaction.

$$Pt \leftrightarrow Pt^{2+} + 2e^{-}, \qquad \mathrm{E}_0 = 1.188\ \mathrm{V\ vs.\ SHE} \tag{1.5}$$

Parallel to Pt dissolution, the oxidation of Pt can also take place at high potentials as shown in Equation 1.6. As the oxide layer forms on Pt surface, the Pt atoms can no longer dissolve according to Equation 1.5, hence, Pt oxide actively counteracts catalyst degradation. In fact, at potentials larger than 1.15 V or at long holding time on high potentials, this protective PtO layer can completely cover the catalyst site and stop Pt from dissolving. The oxide layer formed will be removed during the subsequent cathodic scan (decreasing potential), following the reverse direction of Equation 1.6, exposing bare Pt to dissolution in the next cycle (42–47).

$$Pt + H_2O \leftrightarrow PtO + 2H^+ + 2e^-, \quad E_0 = 0.98\ \text{V vs. SHE} \qquad 1.6$$

In addition to formation of Pt ions directly from Pt in Equation 1.5, Pt ions can also be produced through the **chemical dissolution** (43,45–48) of the formed platinum oxides at high potentials as illustrated in Equation 1.7.

$$PtO + 2H^+ \leftrightarrow Pt^{2+} + H_2O \qquad 1.7$$

As shown in Figure 1.4, when Pt or Pt oxide dissolves and forms Pt cations (Pt^{2+}) at high potentials, Pt cations face two distinct paths afterwards. They may diffuse into the membrane through the ionomer from the electrode. The driving force for the Pt^{2+} movement towards the membrane is the voltage gradient between the anode and cathode, resulting in migration of Pt ions from the cathode catalyst layer through the electrolyte toward the anode (18). Within the membrane, they can interact with the hydrogen originating from the anode side according to Equation 1.8, and therefore deposit there, forming the well-known **Pt band in the membrane** (42,44,45,47). This leads to irreversible catalyst degradation and material loss into membrane as Pt particles deposited in the membrane are no longer able to catalyze the reactions in the electrode.

$$Pt^{2+} + H_2 \leftrightarrow Pt + 2H^+ \qquad 1.8$$

Alternatively, dissolved Pt ions can re-deposit on fresh Pt surface of larger particles according to the reverse direction of Equation 1.5 during the subsequent cathodic scan, resulting in Pt particle growth. This phenomenon is called **Ostwald ripening** (42,44,45,47,48). At anodic scans (increasing potential) where Pt dissolution occurs according to forward direction of Equation 1.5, the smaller particles dissolve more rapidly than large ones due to their higher surface energy. Subsequently, during cathodic potential (decreasing potential), Pt^{2+} ions will re-deposit onto larger particles. This phenomenon results in permanent particle growth and consequently loss of electrochemically active surface area (ECSA). ECSA quantifies the portion of the catalyst surface that actively participates in the electrochemical reactions. In terms of kinetics, a highly rough electrode surface offers a multitude of reaction sites compared to a smooth electrode surface (10). Hence, Pt catalysts are fabricated as nanoparticles to maximize

the available surface area for electrochemical reactions, particularly the oxygen reduction reaction (ORR) at the cathode.

Another mechanism for Pt dissolution that has been recently modeled and proposed in the literature is **place exchange** (44–46). During anodic Pt dissolution shown in Equation 1.5, as the potential exceeds the equilibrium potential, an oxide layer forms on the Pt catalyst surface, reducing the dissolution of Pt. If the potential continues to increase or is held constant for an enough time, the adsorbed oxygen atoms on the surface shift to sub-surface positions through a place exchange mechanism in Equation 1.9, exposing the Pt atoms again. New oxides can then attach to the exposed platinum, and consequently, gradually integrate more deeply into the platinum lattice through the place exchange process. In the next step, during a cathodic potential sweep, in addition to the reduction of the formed oxides, a **cathodic dissolution** (44–46) of the exchanged platinum will occur as described in Equation 1.10. This entire process is illustrated in Figure 1.4.

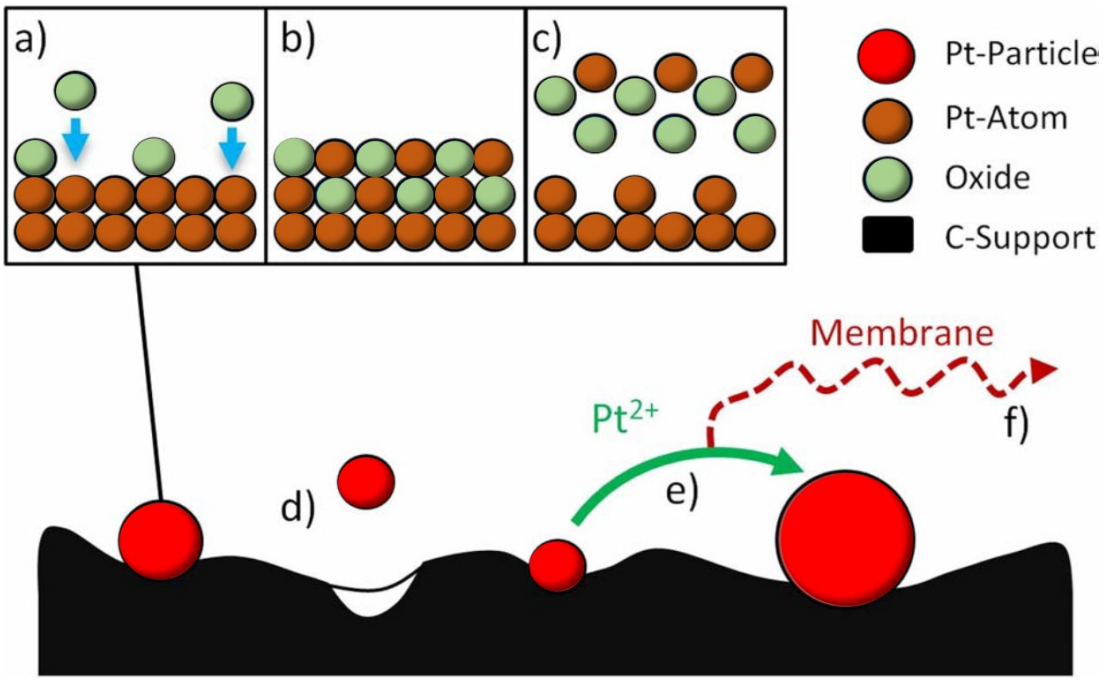

Figure 1.4. **Pt degradation mechanisms: (a) Pt oxidation and PtO surface coverage; (b) Place exchange between Pt lattice and adsorbed O atoms; (c) Oxide reduction and cathodic dissolution of exchanged Pt; (d) Carbon corrosion; (e) Electrochemical Ostwald-Ripening; (f) Pt^{2+} ion dissolution into the membrane, Reprinted from (45) with permission from the Electrochemical Society.**

$$PtO \leftrightarrow O - Pt \quad (1.9)$$

$$O - Pt + 2H^+ \leftrightarrow H_2O + Pt^{2+} \quad (1.10)$$

1.2.2. Degradation Testing

Fuel cell degradation testing is conducted for comprehending materials behavior and degradation mechanisms, as well as for evaluating durability. As these tests could be very time consuming, in most cases, accelerated stress tests (ASTs) on small-scale laboratory setups ranging from five to 50 cm^2 are developed and used to expedite results and conserve resources, including fuel and operator time (49). Common stressors used in ASTs include increased cell voltage, voltage cycling, elevated temperature, high or low humidity, humidity cycling, and increased oxygen concentration, etc. Voltage cycling ASTs are usually used to rapidly induce the cathode degradation due to load cycling in PEMFC. Voltage cycling is one of the most damaging stressors for automotive PEMFC (50), in which the voltage of the PEMFC varies between a fixed upper potential limit (UPL) and lower potential limit (LPL) and is held at each of these voltages for a certain amount of time, which are known as UPL dwell/hold time ($tUPL$) and LPL dwell/hold time ($tLPL$), respectively. These AST profile parameters are derived from stack voltage fluctuations extracted from drive cycles, which reflects regional characteristics and specific vehicle usage purposes (51). Figure 1.5 illustrates a schematic of two square wave voltage cycle ASTs. Figure 1.5a is a symmetric square wave, i.e., a square wave potential with identical dwell time at both lower and upper potential limit, with 0.95 V UPL and 0.6 V LPL. However, Figure 1.5b shows an asymmetric square wave with unequal dwell time at LPL and UPL (52). The AST published by DOE (30) to study cathode electrocatalyst durability is a symmetric square voltage cycling AST ranging from 0.6 V to 0.95 V with 3 seconds at each potential.

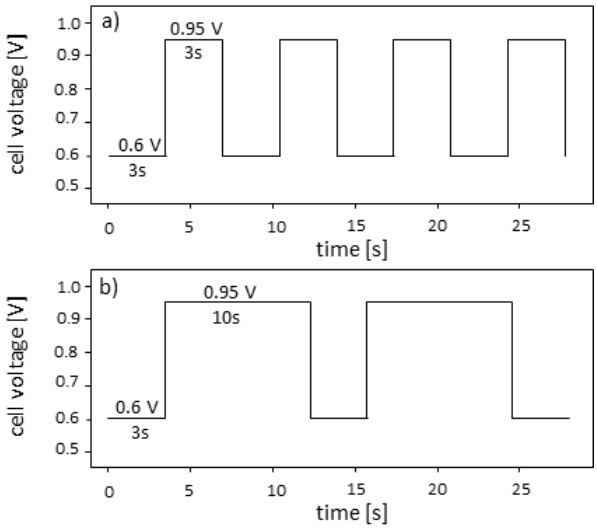

Figure 1.5. Schematic of (a) symmetric and (b) asymmetric square wave voltage cycling ASTs

Studying the impact of voltage cycling AST profile parameters, such as LPL, UPL, and dwell time, on catalyst degradation rate is essential for design of new ASTs that can simulate the degradation occurring during real-world usage of automobiles. Furthermore, determining the effect of AST profile parameters aids in identifying operational conditions that accelerate Pt degradation. This understanding enables the implementation of proactive measures to avoid such scenarios, thereby minimizing Pt degradation and prolonging catalyst lifespan. It can also aid development of degradation models and lifetime prediction tools. In the next section, a review of relevant literature focusing on the voltage cycling AST parametric effect will be provided.

1.3. Voltage Cycling Accelerated Stress Test Parametric Effects

The influence of different voltage cycle profiles on the degradation rate in MEAs has been studied extensively. Also, the parametric effects of temperature and relative humidity (RH) is well-established in the literature. Hereby, increased temperatures and elevated relative humidity values accelerate the loss of ECSA (53–58). For instance, Debe et al. (55) observed a normalized ECSA of approximately 21% after 1890 voltage cycling cycles at 65°C, whereas this value decreased to less than 10% for tests conducted at 95°C. At high temperatures, the processes of platinum dissolution and redeposition are anticipated to occur more rapidly, resulting in the faster degradation of platinum.

Regarding the effect of RH, Bi et al. (58) found out that reducing RH from 100% to 50% decreased the loss rates of catalyst active surface area by approximately half. They proposed that the catalyst's accelerated degradation was a result of increased Pt ion diffusion within the polymer electrolyte's expanded and enlarged water channel networks under conditions of 100% RH. Nevertheless, there exists a trade-off between operating PEM fuel cells at lower temperature and RH levels compared to higher values. While lower temperatures and RH may offer some benefits such as reduced risk of catalyst degradation, higher temperatures promote faster electrochemical reactions, thus enhancing overall cell performance. Furthermore, maintaining a fully humidified system at elevated temperatures ensures optimal hydration of the membrane and electrodes, crucial for efficient proton conduction. Therefore, balancing the advantages and drawbacks of operating at different temperature and RH levels is essential for optimizing PEM fuel cell performance.

In terms of the influence of the upper potential limit on the degradation of the cathode electrode, it has been established in the literature that high UPLs accelerate ECSA loss (59–62). For example, Zihrul et al. (60) investigated the relative change in percent (i.e., normalized to its BOL value) of the ECSA during voltage cycling for three different upper potential limits (UPL=1.0 V, 0.9 V, and 0.8 V), while keeping LPL at 0.6 V and dwell time at each vertex 30 s. They observed the normalized loss in electrochemically active surface area per cycle increases significantly as UPL increases. In fact, while cycling to a UPL of 0.8 V results in around 20% ECSA loss after 20,000 cycles, cycling up to a UPL of 1.0 V leads to more than 80% ECSA loss after the same number of cycles. With a UPL of 0.9 V, the ECSA loss lies in between that observed for 0.8 and 1.0 V UPL.

The effect of LPL, on the other hand, is more complicated as it impacts the Pt oxide reduction and its interplay with Pt dissolution. When LPL exceeds the potential for Pt oxide reduction, a decrease in the rate of ECSA loss is observed, indicating the crucial involvement of Pt oxide reduction (50,63). Messing et al. (64), investigated the effect of LPL on ECSA loss by conducting a series of voltage cycling tests under H_2/air atmosphere with a constant upper potential of 0.98 V but varying lower potentials of 0.6V, 0.7V, and 0.8V, and they found no significant change in ECSA loss across ASTs. Uchimura et al. (65) performed similar experiments to those of Messing et al. but in H_2/N_2 atmosphere and their findings revealed more ECSA loss with decreasing LPL value. In another study, Zhang et al. (50) studied the effect of LPL by keeping the UPL constant at 1.35 V and

varying the LPL at 0.1 V, 0.4 V, 0.6 V, 0.7 V, 0.75 V, 0.8 V, 0.85 V, 0.9 V and 1.0 V. As opposed to Uchimura et al. [6] who observed minimum degradation at LPL of 0.8 V, they found a maximum degradation rate between LPLs of 0.6 V and 1.0 V with a peak at 0.8 V. These findings suggest that the impact of LPL can depend on the absolute value of the UPL and needs more experiments to further explain how it impacts Pt dissolution rate. In this work, thus, the effect of LPL was studied on Pt degradation at two different levels, which will be explained in the next section Design of Experiments.

The impact of dwell time within AST cycles has been also a subject of several studies (59,60,63,66–69). Uchimura et al. (69) delved into the impact of cycle duration by conducting symmetric ASTs with total cycle durations of five and ten seconds and potential limits of 0.6 and 0.95 V. They observed that the duration of the cycle had a minimal impact on the catalyst degradation. However, contrasting results emerged in more recent studies (59,66,67), who observed an increased ECSA loss per cycle with longer cycle durations. For instance, Kneer et al. (67) found that the ECSA loss rate more than doubled when extending the cycle duration from four seconds to 60 seconds in H_2/air environment. Seeking deeper insights, they conducted ASTs with identical cycle durations but varying dwell times at each vertex, employing the following dwell times for LPL and UPL, respectively: 30s-30s, 2s-58s, and 58s-2s. They concluded that the heightened ECSA loss in longer cycle durations is not attributed to the overall duration of the voltage cycle but rather to the prolonged dwell time at the UPL. In a parallel research effort, Zihrul et al. (60) investigated the influence of dwell time at a UPL of 0.9 V in an H_2/N_2 atmosphere. They conducted experiments quite similar to those of Kneer et al. (30s-30s, 50s-10s, 10s-50s) and observed that while ECSA loss increased with longer dwell times at high potential, this effect was considered minor compared to other factors, such as UPL.

Table 1.1 provides a summary of the literature discussed above, highlighting the LPL and UPL along with their corresponding dwell times. As shown in Table 1.1, the previous experiments in the literature have been designed in a way that both UPL and LPL dwell time have changed simultaneously across experiments, whether in the symmetric or asymmetric cycles, which makes the results unreliable as two factors are changing from one experiment to another. The only paper, to the best of author's knowledge, that investigated the effect of LPL/UPL dwell time while the other one kept fixed was published by Young et al. (68) in 2013. They varied dwell time at high potentials (5, 20, 60, 300, 600 s) during square wave voltage cycling between 0.6 – 1.4 V while the

LPL dwell time was constant (30 s) across all experiments. They found an increasing degradation per cycle with increasing dwell time at high potentials. Nevertheless, at this elevated UPLs (1.4 V), in addition to platinum dissolution, carbon corrosion is also contributing to the ECSA loss. Therefore, the effect of LPL dwell time and UPL dwell time on Pt degradation remains convoluted in the literature. In this work, therefore, a set of ASTs was designed and conducted to fill the knowledge gap and determine the exclusive impact of LPL and UPL dwell times on Pt ECSA loss. Indeed, these experiments allow to measure the impact of LPL and UPL dwell times across different levels of LPL solely on Pt catalyst degradation, without carbon corrosion, during normal automotive operation condition with OCVs lower than 1.0 V. The details of these experiments will be explained in the next section Design of Experiments.

Table 1.1. Summary of LPL, UPL, and their dwell time in studies investigating the effect of voltage cycling AST profile parameters on PEMFC durability

LPL [V]	UPL [V]	LPL-UPL dwell time [s]	Reference
0.6	0.85,0.95,1	Symmetric [1-1, 2-2, 8-8]	(59)
0.6	OCV	Symmetric [2.5-2.5, 10-10, 20-20]	(66)
0.6, 0.7, 0.8	0.98	Symmetric [3-3]	(64)
0.6	OCV	Symmetric [2-2, 4-4, 8-8, 30-30, 300-300], Asymmetric [30-30, 58-2, 2-58]	(67)
0.6	0.8,0.9,1	Asymmetric [30-30, 50-10, 10-50]	(60)
0.1, 0.4, 0.6, 0.7, 0.75, 0.8, 0.85, 0.9,1	1.35	Symmetric [2-2]	(50)
0.6	0.9, 1, 1.1, 1.2, 1.3, 1.4	Asymmetric [30-5, 30-20, 30-60, 30-300, 30-600]	(68)
0.6, 0.7, 0.75, 0.8	0.95	Asymmetric [2.5-10]	(65)
0.6	0.95	Symmetric [2.5-2.5, 5-5]	(69)
0.1, 0.5, 0.88	1.3	symmetric [30-30, 600-600]	(63)

1.4. Design of Experiments

In this study, a set of AST experiments were designed with the purpose of deconvoluting the effect of LPL dwell time and UPL dwell time on the development of Pt ECSA across different levels of LPL. The ASTs involved square wave voltage cycling between LPL and UPL in a H_2/air atmosphere, while maintaining one of the LPL and UPL dwell times

constant from one experiment to another. The UPL was set at 0.95 V for all experiments to replicate the OCV, which typically falls below 1.0 V during regular operation. LPL, resembling the stack potential during high power demands, was set at two levels: 0.6 V and 0.8 V. These levels were chosen to evaluate the significant impact of Pt removal rate extremes. It was ensured that LPL stayed below 0.880 V, known as the platinum oxide reduction potential, to cause substantial degradation (63) . The LPL and UPL dwell times were chosen at two levels: 3 seconds and 10 seconds, resulting in combinations of 3-3, 3-10, and 10-3, where the first number represents the LPL dwell time, and the second number represents the UPL dwell time. The 3-3 s dwell time was selected based on DOE guidelines for testing electrocatalyst durability (30). The 10-3 second dwell time was chosen to ensure thorough oxide layer removal at LPL, crucial for investigating degradation mechanisms (48). The 3-10 s was selected to accommodate the extended holds at high potentials observed in heavy-duty vehicles according to drive cycle analysis (51). The AST 0.6-0.95V_3-3, DOE standard AST protocol, was considered our baseline and repeated three times, while the rest of experiments were repeated only once. Figure 1.6 shows a schematic of the voltage profiles of the experiments.

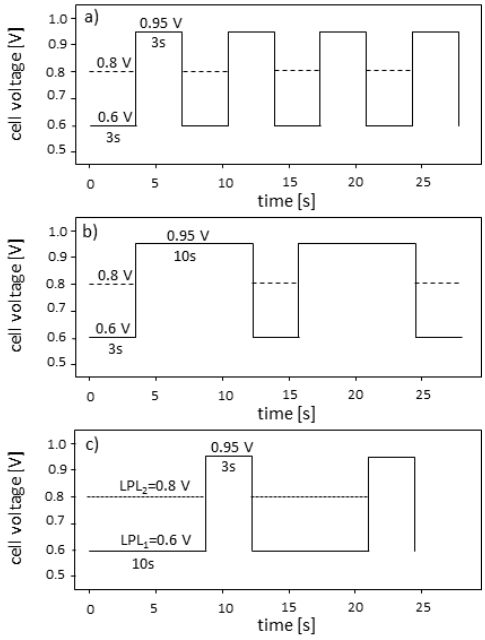

Figure 1.6. Voltage profiles of load cycling between LPL of 0.6 (solid line) or 0.8 (dashed line) to UPL of 0.95 V with LPL dwell times and UPL dwell times of (a) 3s –3s, (b) 3s – 10s, and (c) 10s – 3s, respectively

The temperature was set at 80°C, as recommended by the US DOE for optimizing electrochemical reactions facilitated by Pt catalysts (30). RH was maintained at 95% to achieve near-full hydration for optimal membrane functionality, while avoiding 100% to prevent flooding during experiments. The main response variable was Pt ECSA loss of the cathode electrode, which was measured through cyclic voltammetry at regular intervals.

The tests were stopped either after 30,000 cycles, as recommended by the US DOE with corresponding targets in a standardized protocol for studying electrocatalyst durability, or when a 10% voltage loss from the BOL cell voltage at 0.6 A/cm² occurred, considered as the failure criterion (30). This criterion is employed to identify the threshold where degradation reaches a level deemed unacceptable by the US DOE for achieving the desired performance of the fuel cell stack (70). In this study, the proposed 30,000 cycles by US DOE were sufficient to observe meaningful degradation of Pt ECSA and performance between ASTs. As discussed in the section, two out of the six tests met the 10% failure criterion before reaching 30,000 cycles, while the remaining tests retained 90-95% of their performance after completing 30,000 cycles. Table 1.2 shows a summary of experiments.

Table 1.2. Voltage cycling accelerated stress tests conducted in this study

Number	AST Procedure	LPL [V]	UPL [V]	LPL dwell time [s]	UPL dwell time [s]	EoL/EoT NoC [#]	No. of repeats
1	0.6-0.95V_3-3s	0.6	0.95	3	3	30,000	3
2	0.8-0.95V_3-3s	0.8	0.95	3	3	30,000	1
3	0.6-0.95V_10-3s	0.6	0.95	10	3	30,000	1
4	0.8-0.95V_10-3s	0.8	0.95	10	3	30,000	1
5	0.6-0.95V_3-10s	0.6	0.95	3	10	20,000	1
6	0.8-0.95V_3-10s	0.8	0.95	3	10	25,000	1

The equivalent use-level lifetime of AST cycles is complex to determine, as this value will vary for each drive cycle, which is characteristic of the vehicle specifications and operating conditions. For this purpose, extracting the vehicle's voltage profile from the drive cycle is necessary. In this regard, Messing et al. (52) proposed a methodology to correlate accelerated test data with real-world operating conditions by counting equivalent

voltage cycles from voltage profiles. In their approach, voltage cycles from the driving cycle are deemed equivalent to AST cycles if they start at OCV and exceed a specified voltage drop threshold. Using this method, for instance, they predicted the lifetime of a bus, using the drive cycle described in (71), to be 1100 hours with a 10% voltage loss criterion. As shown in section 4.2, after 25,000 cycles of AST 0.8-0.95V_3-10s, which includes representative cycles for heavy-duty applications due to prolonged dwell time at UPL, a 10% voltage loss was reached. This suggests that approximately 25,000 cycles of AST 0.8-0.95V_3-10s may equate to 1100 hours of bus use-level. This is an estimated value as their model considers start-up/shutdown cycles in addition to load cycling; therefore, the lifetime assumed solely due to load cycling in this work could be higher.

1.5. Objectives

This thesis aims to systematically investigate the impact of cycle profile in voltage cycling ASTs on the degradation of cathode Pt catalyst in PEM fuel cells. Specifically, the main objective of the work is to determine the effect of LPL, LPL dwell time, and UPL dwell time parameters on the development of Pt ECSA throughout the aging process. The experiments aim to complement previous findings in the literature by systematically adjusting potential limits and dwell times, thereby enhancing our understanding of the underlying mechanism of Pt loss during load cycle operation.

To achieve this goal, 5 cm^2 active area fuel cells were fabricated and assembled in-house and were subjected to degradation through the set of voltage cycling ASTs proposed in the previous section. Regular in-situ electrochemical characterization was conducted during the tests to monitor the degradation of the Pt catalyst within cathode electrode, as well as performance loss of the cells. Additionally, to enhance our understanding, postmortem analyses were performed on degraded cells using electron microscopy techniques, specifically scanning electron microscopy (SEM) and transmission electron microscopy (TEM). The materials and methods for these steps were detailed in Chapter 2.

After collecting the data, statistical analysis was performed to determine significant differences in the results and identify which variables explained most of the variability in Pt ECSA loss (Chapter 3). In the following chapter, the experimental findings along with potential degradation mechanisms were discussed. Also, the experimental

results were corroborated through the application of a previously developed physical model (48) by other researchers at SFU Fuel Cell Research Laboratory (FCReL) (Chapter 4). Lastly, Lastly, a summary of the results and recommendations for fuel cell system design and operation is provided based on the findings (Chapter 5).

Chapter 2.

Experimental

2.1. Fuel Cell Fabrication

In fuel cell fabrication process, membrane electrode assembly (MEA) is the heart of the fuel cell compared to other components. This assembly comprises a membrane, catalyst layers (CL), and gas-diffusion layers (GDL), as illustrated in Figure 2.1.

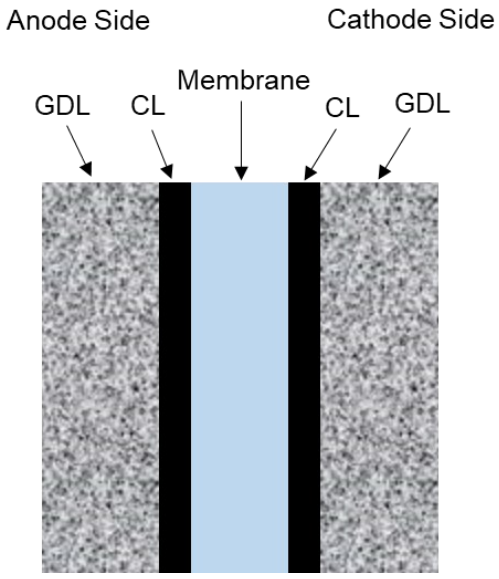

Figure 2.1. Membrane electrode assembly

Commercially available components for MEAs are accessible from various vendors. The membrane and gas diffusion media exhibit consistent specifications across different suppliers. However, notable differences arise in the catalyst layer due to each vendor employing their proprietary recipe. Consequently, despite detailed parameter specifications, significant performance variations exist among catalyst layers from different vendors. To ensure optimal consistency, the catalyst layer was produced in-house for this work. Table 2.1 presents the consumable materials utilized in each fuel cell, along with details about their manufacturers.

Table 2.1. Material details for fuel cell fabrication

Name	Purpose	Manufacturer	Supplier
Nafion NR-211	Membrane	Chemours	Ion Power
Sigracet 22 BB	GDL	SGL	Fuel Cell Store
Pt/C 50 wt% Pt, High Surface Area Carbon	Catalyst Powder	Tanaka	Tanaka
D2021 1100 EW at 20 wt%	Ionomer Dispersion	Chemours	Ion Power
Teflon Sheet	Gasket	DuPont	Fuel Cell Store
Polyimide Adhesive Film	Support	3M	Digi-Key

2.1.1. Catalyst Layer Fabrication

The primary goals in creating a catalyst layer are to effectively manage the catalyst loading, control the layer thickness, and achieve consistent layer porosity in a reliable and reproducible manner. These aims can be accomplished, with different degrees of success, through various catalyst ink coating techniques such as doctor blade/decal transfer, hand painting, air spraying, pulse spray swirl, ultrasonic spray deposition, and inkjet printing (72,73). In manufacturing, catalyst layers can be coated on the membrane (52) forming a catalyst-coated membrane (CCM) composite, or on gas diffusion layers, forming gas diffusion electrodes (GDEs) (74). Given the prevailing consensus that CCMs generally exhibit superior performance compared to GDEs (75), this study focused on producing CCMs.

In this study, the CCMs were meticulously fabricated utilizing a Sono-Tek ExactaCoat sonic spray coater situated at SFU 4DLabs (4dlabs.ca), a distinguished materials science research institute providing comprehensive services for the design, development, demonstration, and delivery of advanced functional materials and nanoscale devices. The selection of the ExactaCoat spray coater was driven not only by its convenient availability but also by its previous successful use within our research group (64), ensuring a reliable and repeatable operation. The subsequent section elucidates a detailed explanation of the spray coating process and the optimization of its parameters.

Spray Coating

Achieving optimal results in any ultrasonic spray coating system necessitates precise adjustments to key variables, including surface temperature, flow rate, shaping air, run power, and idle power. Table 2.2 summarized the value of these parameters that were used in this research. These parameters were derived from the thesis of Marvin

Messing (52), a former member of our research group who had previously fine-tuned these variables for the fabrication of Pt/C CCM.

Table 2.2. Spray coater configuration for CCM fabrication

Neme	Value	Unit	Description
T_s	85	°C	Table temperature
V_{ink}	0.37	ml/min	Ink flowrate
P_{air}	0.78	kPa	Shaping air pressure
P_{run}	3	W	Sonicator run power
P_{idle}	0.5	W	Sonicator idle power

After setting all the parameters on the sonic spray coater, a 16 cm^2 membrane piece was utilized to achieve a final 5 cm^2 active area sample. Subsequently, the thick and thin backing layers of the membrane were carefully removed, and the membrane was positioned beneath a mask featuring locating markers, aligning it precisely on the spray coater surface. This mask had a 6 cm^2 cut-out, resulting in the creation of a 6 cm^2 CCM. The catalyst frame derived from the difference between 5 and 6 cm^2 was used during assembly as described in 2.1.2. Both sides of the membrane underwent a uniform coating process, with the number of coating cycles varying based on their respective catalyst loading requirements.

To achieve the desired catalyst loadings, 0.45 mg/cm^2 and 0.25 mg/cm^2 for cathode and anode respectively, it was determined that 14 to 16 coating cycles were needed for the anode side and 26 to 28 coating cycles for the cathode side. The loading was assessed by measuring the weight of each side of the CCM during fabrication and comparing it to the weight of the bare membrane. After an estimated number of cycles for each side, the weight of the warm membrane was measured and compared to the bare membrane until the target Pt loading was reached. Due to weight fluctuations with membrane temperature, measurements were taken 90 seconds after removing the sample from the heated surface at each step (bare membrane, anode side coated, anode and cathode sides coated), with the bare membrane heated for at least five minutes before weight measurement. For example, for a Pt loading of 0.25 mg/cm^2 on the anode side of a 5 cm^2 active area, 1.25 mg of Pt is required. Using 50 wt% Pt/C powder in this work, the Pt/C weight will be 2.5 g. The difference between the bare membrane and the CCM when only the anode is coated is the weight of solid components, which includes Pt, carbon,

and ionomer. By calculating the Pt weight percentage, the Pt loading can be found from weight measurements.

Catalyst Ink

In the process of manufacturing CCM, it is necessary to prepare a catalyst ink for subsequent deposition onto the substrate using the spray coater. A standard Pt catalyst ink formulation includes Pt/C powder, ionomer dispersion, deionized water (Di water), and alcohol (usually methanol). The ink contains 0.5-1 wt% solids and is prepared with an alcohol-to-water ratio varying from 50:50 to 75:25, depending on substrate solubility and mechanical strength. For the purposes of this research, the inks were prepared with a 1% solids weight and a specified ratio of 75:25 for Alcohol to H_2O. In terms of ionomer concentration, it has been consistently demonstrated that 30 wt% of ionomer solids are the optimal loading across all Pt loadings. For instance, in a 100 g ink, 1 g of total solids would comprise 0.30 g of dry ionomer + 0.70 g of supported platinum nanoparticles on carbon (Pt/C), with the remaining ink consisting of methanol and H_2O (76).

To complete the ink calculations, the composition of the ionomer dispersion is essential. In this work, a 20 wt% D2021 Nafion™ dispersion was used, which is alcohol-based and contains 46 wt% volatile organic compounds (VOCs), including 1-propanol and ethanol, 34 wt% H_2O, and 20% dry ionomer. Moreover, for every round of spray coating, a minimum of 40 g of ink was utilized to fabricate six samples per batch. Given the information above, the weight distribution of the ink components can be determined based on the specified total weight (M), such as 40 g in this scenario. $Ionomer$ is the variable signifying the quantity of dry ionomer in the ink (52):

$$\mathrm{Ionomer\ [g]} = \mathrm{M} \times 1\% \times 30\% \tag{2.1}$$

$$\mathrm{Ionomer\ dispersion\ (D2021)\ [g]} = \frac{\mathrm{Ionomer}}{20\%} \tag{2.2}$$

$$\mathrm{Pt/C\ [g]} = \mathrm{M} \times 1\% \times 70\% \tag{2.3}$$

Considering 75:25 Alcohol: H_2O,

$$\mathrm{MeOH\ [g]} = 0.75 \times (\mathrm{M - Ionomer - Pt/C}) - \mathrm{D2021} \times 46\% \quad (2.4)$$

$$\mathrm{H_2O\ [g]} = 0.25 \times (\mathrm{M - Ionomer - Pt/C}) - \mathrm{D2021} \times 34\% \quad (2.5)$$

After determining the component weights for a 40 g batch of ink, the following steps were undertaken (76):

1. Pt/C powder was introduced into a beaker, and all water was added to it.
2. A 20% D2021 Ionomer dispersion was diluted in 2 g of methanol and subjected to sonication for 1 minute.
3. The majority of the MeOH, specifically MeOH [g] – 4 g, was slowly incorporated into the Pt/C solution while stirring. It is crucial to avoid quick addition or incomplete mixing, as Pt-based catalysts may react and lose their effectiveness.
4. The ionomer mixture, prepared in step 2, was added dropwise using a pipette at a rate of 1-2 drops per second.
5. The container holding the ionomer mixture and the pipette were rinsed into the Pt/C solution with the remaining 2 g of methanol.
6. The solution was stirred for over an hour, subjected to sonication for 10-20 minutes, and continuously stirred until ready for use. Before each use, the solution underwent sonication again to ensure homogeneity.

2.1.2. Membrane Electrode Assembly

Once the CCM was manufactured, it underwent the assembly process for integration into the fuel cell hardware. Both sides of the CCM were meticulously enclosed with 80 µm thick Kapton® polyimide adhesive film (orange film in Figure 2.2). This film served a dual purpose: acting as a primary gasket to prevent any potential leakage and providing adequate thickness to keep the CCM securely in place within the fuel cell hardware, particularly when fitted with locating holes. This encapsulation process effectively sealed the CCM within the assembly. Figure 2.2 demonstrates the rigid frame sealed CCM within the adhesive films. Ideally, we did not want any air trapped within the

sample. However, the air was released due to compression in the stacking device later during the test.

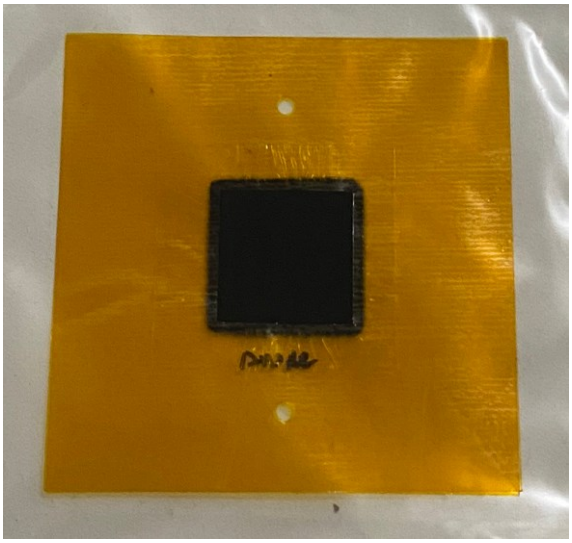

Figure 2.2. Sealed CCM within the Kapton® polyimide adhesive film

Following the encapsulation, a precise sequence of steps was followed to ensure proper alignment and integration of various components. First, a 75 µm thick PTFE Teflon® sheet with a 5 cm^2 cut-out was positioned on one of the stacking device plates. Subsequently, the GDL was inserted into the designated window within the Teflon sheet. The encapsulated CCM was then carefully aligned and placed atop the GDL. Figure 2.3 depicts a schematic side view of half of an MEA along with the components employed for assembly.

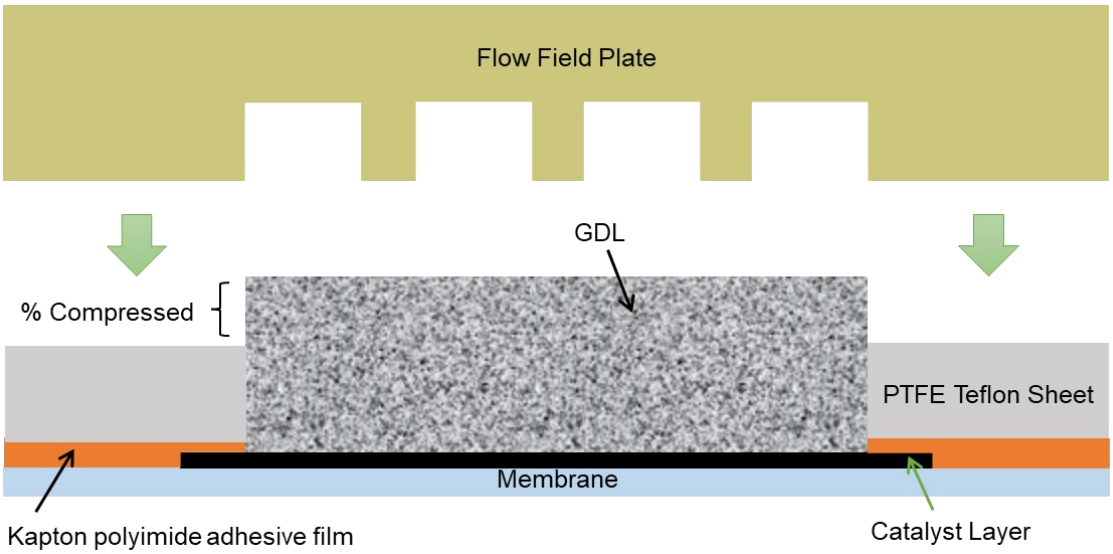

Figure 2.3. MEA components and gasket layers

To complete the setup, another Teflon sheet is aligned, along with an additional GDL placed at its center. Subsequently, the other stacking device plate is carefully placed to prevent any potential damage or displacement of the CCM and GDLs. Finally, the assembly is secured using a torque wrench set to 10 lb in. Figure 2.4 displays two stacking device plates for the anode and cathode sides.

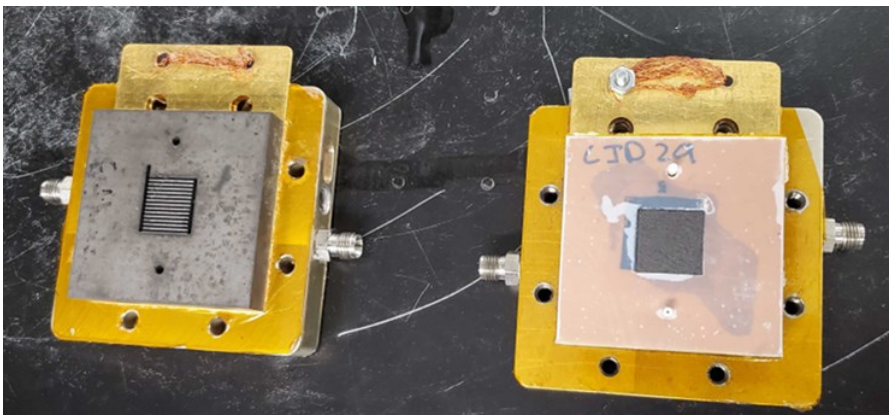

Figure 2.4. Left: Anode fuel cell stacking plate without components, Right: Cathode fuel cell stacking plate featuring MEA and Teflon gasket on top

2.2. Degradation Testing

The in-house fabricated MEAs underwent testing using a fuel cell test station. This section will detail the testing hardware and test protocols employed to condition, recover, and degrade the cells in the laboratory.

2.2.1. Test Station and Fuel Cell Hardware

The MEAs were positioned between two 5 cm^2 flow field Poco graphite blocks featuring straight and parallel channels in co-flow mode. In addition to graphite plate, the hardware incorporates current collectors plated with gold and endplates equipped with resistive heating rods designed to maintain a consistent temperature within the cell. Figure 2.5 shows the hardware and its components.

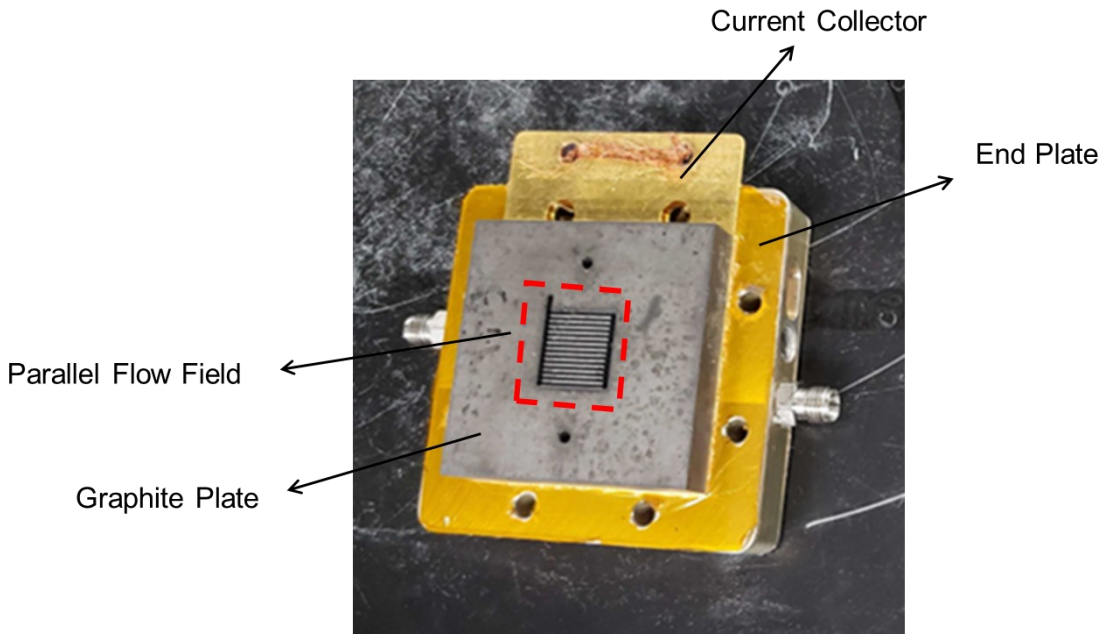

Figure 2.5. Fuel Cell Hardware

The fuel cell needs to be constantly supplied with hydrogen and oxygen gasses under controlled operating conditions, including flow rate, back pressure, dew point temperature, and inlet gas temperature throughout the testing period. The operating condition control was facilitated by a Greenlight Innovation G20 fuel cell test station in this study, which also subjected the fuel cells to varying loads. The cells were assembled at a torque of 1.13 Nm. Furthermore, load cycling, cyclic voltammetry (CV), and

electrochemical impedance spectroscopy (EIS) were conducted using a Gamry Interface 5000 potentiostat. The load cycle protocol involved operating at 80 °C, 95% relative humidity (RH), 180 kPa absolute back pressure, and H_2/air flow rates of 0.5/1.5 standard liter per minute (slpm). Figure 2.6 displays an image of the fuel cell hardware connected to the G20 test station.

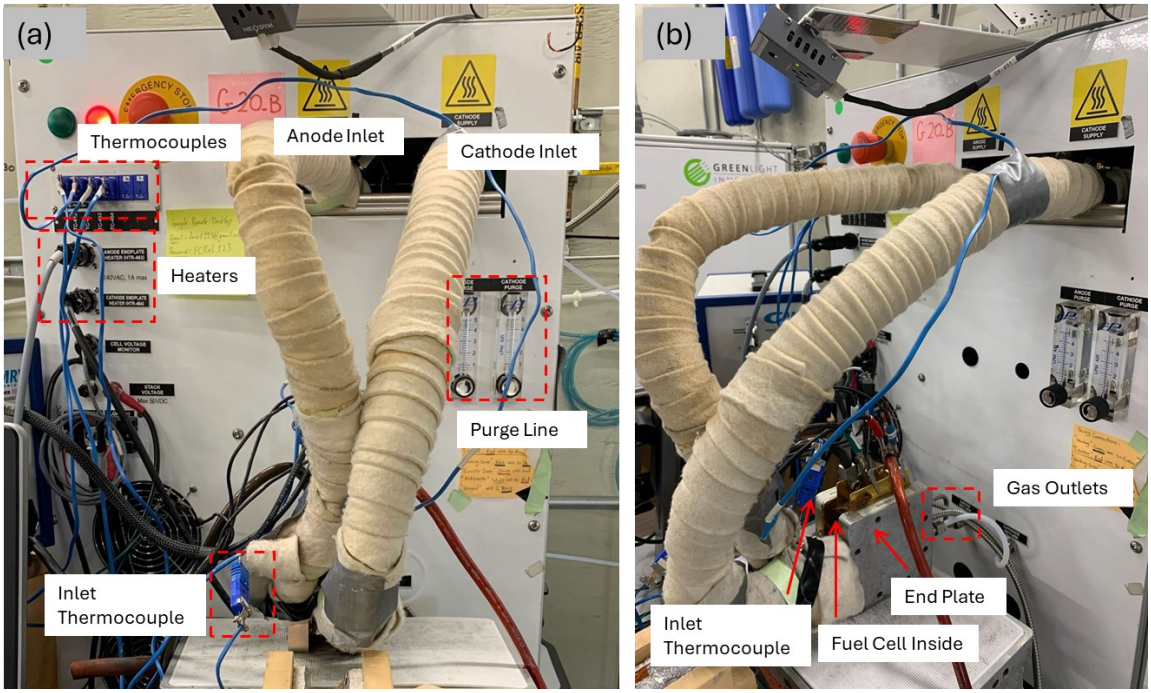

Figure 2.6. (a) Greenlight Innovation G20 fuel cell test station, (b) Fuel cell hardware connected to the test station

2.2.2. Fuel Cell Conditioning

The fuel cell conditioning procedure involved several steps to prepare the cell for optimal performance. CV was employed initially. This step included applying repeated cycles of voltage sweeping between 0.2 and 0.8 V at a scan rate of 50 mV/s. Hydrogen and nitrogen were flowed to the anode and cathode at flow rates of 0.1/0.1 slpm. During CV, the platinum surface undergoes cyclic oxidation and reduction reactions, reconstructing into a crystalline structure, which enhances catalyst activity. Following CV, air starvation cycles were performed. Initially, hydrogen and air were flowed to the anode and cathode to stabilize the OCV. Then, the cathode airflow was switched to nitrogen, inducing an OCV drop. Once the OCV drops to 0.2 V, airflow was switched back to air. This process reduced platinum oxide back to platinum, increasing catalyst availability and

was repeated five times every six hours. Finally, a steady-state operation was conducted in between air starves sets at elevated temperature (80 °C) and humidity (95% RH) for a total duration of 24 h. Hydrogen and air were flowed to the anode and cathode at flow rates of 0.5/1.5 slpm, and a current density of around 3 A is maintained. This step conditioned the ionomer phase in the membrane and catalyst layers, opened water channels, and improved component interfaces. Overall, the conditioning aims to maximize stable performance by enhancing catalyst activity, ensuring membrane hydration, improving interfaces, and stabilizing operation (77).

2.2.3. Fuel Cell Recovery

The recovery process is an essential preliminary step before diagnosing fuel cell performance, designed to mitigate reversible losses and restore optimal function. These losses, stemming from contaminants like CO and CO_2, flooding, and fuel starvation can impede access to the cathode catalyst layer, thus diminishing overall performance. By addressing these reversible losses, the recovery process allows for a focused analysis on irreversible degradation modes such as catalyst dissolution (18). The recovery protocol developed by the US Department of Energy (DOE) with minor adjustment on the flow rates (30) was utilized for this task, as outlined in Table 2.3. The cell was subjected to 80°C temperature and 95% RH throughout the recovery phase.

Table 2.3. MEA recovery protocol

Step	Step Name	Anode Composition	Anode Flow [slpm]	Cathode Composition	Cathode Flow [slpm]	Duration [s]
1	N_2 soak	N_2	3	N_2	3	120
2	Air soak	N/A	0	Air	3	900
3	N_2 soak	N_2	3	N_2	3	120
4	H_2 soak	H_2	3	N/A	0	600
5	H_2-air back on	H_2	0.5	Air	1.5	5

2.2.4. Voltage Cycling Accelerated Stress Test Protocol

Voltage cycling experiments were carried out to simulate fuel cell aging under controlled conditions, which approximate load cycling in vehicle operation. The details of the experiment designs were discussed in Section 1.4. The experiments were performed under operating conditions specified in Table 2.4. The conditions in this table were applied consistently for load cycling and throughout other steps, unless explicitly stated otherwise.

The tests were run until 30k load cycles were completed, i.e., EOT, or when the cells reached 10% voltage loss as the failure criterion, i.e., EOL, whichever comes first. The Gamry Interface 5000E potnetiostat along with internal G20 station load bank was used to reach the LPL and UPL and implement the voltage cycling between them. A set of in-situ electrochemical diagnostics were performed at 0, 1k, 3k, 5k, 10k, 20k, 30k cycles, which are explained in the next section.

Table 2.4. General fuel cell operating conditions

Temperature [°C]	RH [%]	Pressure [kPaabs]	Anode Flow [slpm]	Cathode Flow [slpm]	Anode Gas	Cathode Gas
80	95	180	0.5	1.5	H_2	Air

2.3. In-situ Electrochemical Diagnostics

In situ diagnostics play a pivotal role in comprehensively evaluating the performance and degradation of fuel cells over their operational lifespan or after degradation testing. These diagnostics were initially performed at the beginning of life (BOL) after conditioning, and subsequently at certain intervals, 1k, 3k, 5k, 10k, 20k, and 30k cycles, throughout accelerated stress testing (AST) until reaching either the end of test (EOT) or the end of life (EOL) criterion. The primary diagnostic techniques employed in this study encompass polarization curves, cyclic voltammetry, and impedance spectroscopy. A Gamry Interface 5000E potentiostat was used to implement the diagnostics. Fuel cell operating conditions used for diagnostics are described in Table 2.5.

Table 2.5. Diagnostic fuel cell operating conditions

Temperature [°C]	RH [%]	Pressure [kPaabs]	Anode Flow [slpm]	Cathode Flow [slpm]	Anode Gas	Cathode Gas
80	95	180	0.1	0.1	H_2	N_2

2.3.1. Polarization Curve

The fuel cell polarization curve, referred to as the I-V curve, illustrates the cell voltage corresponding to different cell currents. This characteristic curve is a common tool to assess the performance of a fuel cell. Figure 2.7 presents a typical polarization curve of a fuel cell used in this study, which shows the performance of the fuel cell potential at various current densities. At different current densities, different losses lower the cell

potential from the theoretical cell potential (1.23 V), which can be used to identify potential faults in the various components of the fuel cell.

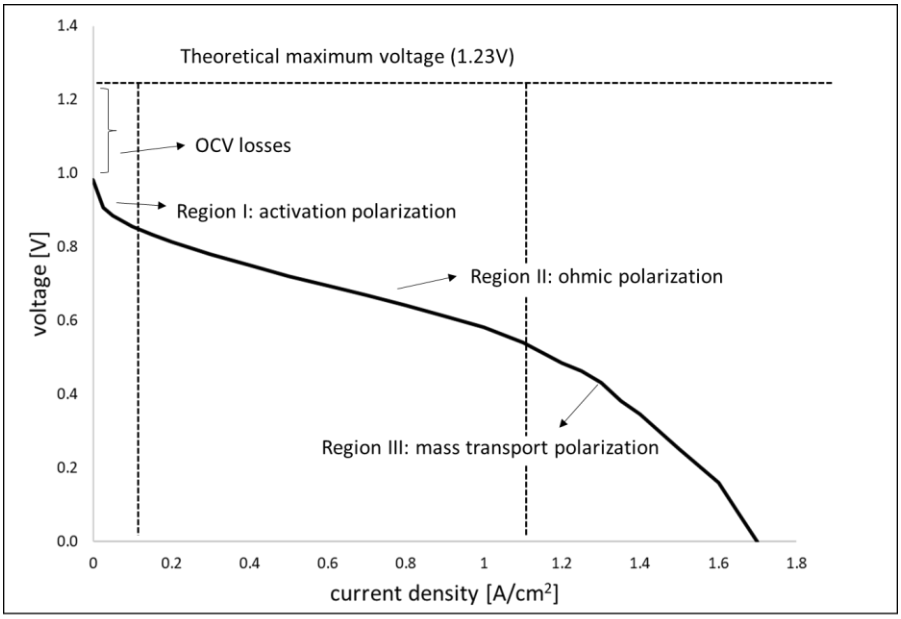

Figure 2.7. Sample polarization curve

The initial loss of standard potential, in a PEMFC involves a substantial 0.2 V drop, accounting for a significant 20% efficiency loss at the open circuit without any useful electron draw. The OCV losses are mostly caused by crossover of reactants through the electrolyte and subsequent mixed-potential reaction at the opposite electrode, as well as electrical short circuits in the fuel cells as a result electron transfer through the electrolyte. Additionally, impurities and contaminants in the reactants can also decrease the voltage at open circuit significantly. Even though by eliminating contaminants and using efficient materials, the OCV losses can be minimized, ultimately, as a very small amount (even milliamperes per cubic centimeter) of species crossover will cause a large decrease in OCV, it is nearly impossible to completely eliminate this problem in polymer electrolyte systems (18).

Region I is losses associated with activation polarization, which dominates losses at low current density. The activation polarization loss is the voltage overpotential required to overcome the activation energy of the electrochemical reaction on the catalytic surface. This loss is significantly influenced by the catalyst layer and its morphology. Increasing the active surface area of the catalyst and ensuring the absence of catalyst poisons and impurities in the reacting flow could minimize this loss. Regarding operating parameters,

elevating the temperature and concentration of the reacting species will reduce activation polarization loss (18).

In region II, reduction in voltage is mainly due to internal ohmic losses through the fuel cell, leading to the nearly linear trend. The ohmic polarization usually stems from the combined ohmic and ionic resistance of various cell elements, including the ionic resistance of the electrolyte, as well as the electric resistance of bipolar plates and contact points between cell components. Therefore, employing materials with the highest possible ionic or electronic conductivity and fabricating components with the thinnest feasible thickness could mitigate the loss to some extent (18).

Region III shows concentration polarization, also called mass transport losses, which is caused by a reduction in the reactant surface concentration. The transport rate of the reactants to the catalyst could be slow due to many factors, including gas-phase diffusion restrictions, liquid water build-up in the pores, and accumulation of inert gasses and impurities. Thus, a steady supply of reactants and effective water management within the cell are required to mitigate the loss (18).

In this study, polarization curve measurement was performed using the internal load bank of the G20 fuel cell test station and it involved 30 min steady state at 2.5 A to ensure reduction of Pt oxides, followed by stepwise sweep from low to high current density with 2 min hold at each, averaging the last 10 seconds. The measurement was stopped once the voltage dropped below 0.2 V.

2.3.2. Cyclic Voltammetry

While polarization curves offer insights into a fuel cell's overall performance, understanding the specific reasons behind potential faults and their correlation with different components requires the use of additional electrochemical diagnostics. Cyclic voltammetry (CV) is a technique commonly used in PEM fuel cell studies for obtaining specific data about the electrochemical behavior of the catalyst layer and membrane. This method involves applying a triangle voltage waveform to the electrode of interest and measuring the resulting current. By plotting the current versus the applied potential, a voltammogram is generated, which can be used for determining fuel cell performance parameters such as platinum electrochemical surface area (ECSA) and double layer

capacitance (C_{dl}). Figure 2.8 represents a voltammogram example output in this study. The voltage was swept from 0.05 V to 0.8 V, with a consistent sweep rate maintained at 20 mV/s using a Gamry® Interface 5000E potentiostat. The flow of gas during CV is detailed in Table 2.5. As the oxygen reduction reaction (ORR) occurring at the cathode is slower and critical in a PEM fuel cell, the ECSA measurement is conducted for the ORR occurred at the cathode.

In a fuel cell CV experiment, hydrogen is introduced at the anode while a low flow of an inert gas like nitrogen is supplied at the cathode. At the cathode, hydrogen protons attach to specific sites on the catalyst layer and combine with electrons. As shown in Figure 2.8, as the voltage is gradually increased during the forward scan, there is a noticeable peak in the lower potential range, indicating the desorption of hydrogen from the reaction sites.

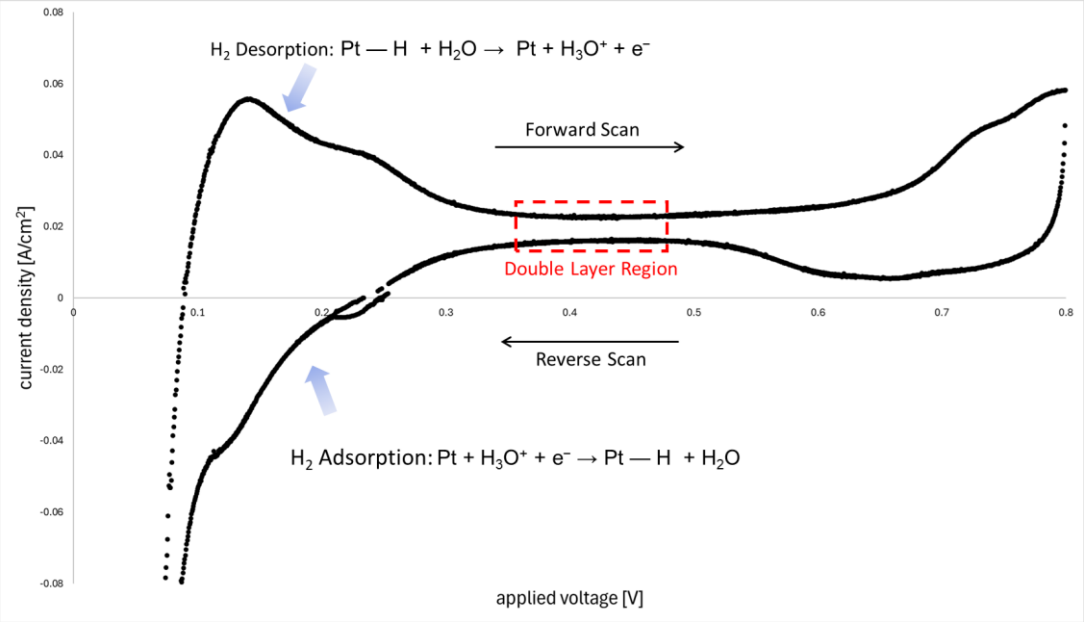

Figure 2.8. Sample cyclic voltammogram

At low voltages, hydrogen atoms adsorbed to platinum reaction sites release electrons, initiating a current through the electrochemical reaction outlined by Equation 2.6:

$$Pt — H + H_2O \rightarrow Pt + H_3O^+ + e^- \qquad 2.6$$

As the voltage increases further, the current declines as all hydrogen ions are liberated until a stable exchange current is attained in the middle of the curve. This current arises from the capacitance formed by an electrochemical double layer. In the reverse scan, when the voltage falls below about 300 mV, hydrogen ions start to be adsorbed again, causing a reduction current as the reverse reaction of Equation 2.6 takes place.

ECSA, which is an indication of how much platinum is accessible and takes part in the fuel cell reactions, is an important parameter that can be extracted from the H_2 voltammogram. The ECSA was measured for the cathode catalyst layer in this study due to the sluggish and more critical kinetics of the ORR. ECSA can be determined using the following formula:

$$\mathrm{ECSA} = \frac{\int \mathrm{I(t)dt}}{\mathrm{SC}} \qquad 2.7$$

Where S is the proportionality constant for Pt in C/m^2 and C is the platinum loading of catalyst layer in gram. In Equation 2.7, the integration of current with respect to time in numerator is the cumulative charge produced during the hydrogen desorption reaction. Given that the voltammogram provides a plot of current against potential and the scan rate is specified, the total charge can be calculated using Equation 2.8, where the scan rate, r, is set at 0.05 V/s.

$$\int \mathrm{I(t)dt} = \frac{\int \mathrm{I(v)dv}}{\mathrm{r}} \qquad 2.8$$

Hence, the ECSA Equation can be expressed as follows, denoted in units of $[m^2/g_{Pt}]$:

$$\mathrm{ECSA} = \frac{\int \mathrm{I(v)dv}}{\mathrm{rSC}} \qquad 2.9$$

The integration of current with respect to voltage in the numerator is the area under the hydrogen desorption peak in the voltammogram. Figure 2.9 shows the area of interest on the voltammogram. The baseline current observed within the potential range of 0.35 to 0.5 V is the non-faradaic or capacitive current emerges from the charging and discharging of the electrical double layer capacitance at the electrode-electrolyte interface, as well as H_2 crossover current. Unlike faradaic currents, the non-faradaic current involves the accumulation of charge without any accompanying chemical reactions or charge transfer

processes. It's crucial to account for the electrical charge related to double layer charging during the analysis to prevent overestimating the charge attributed to electrocatalytic activity.

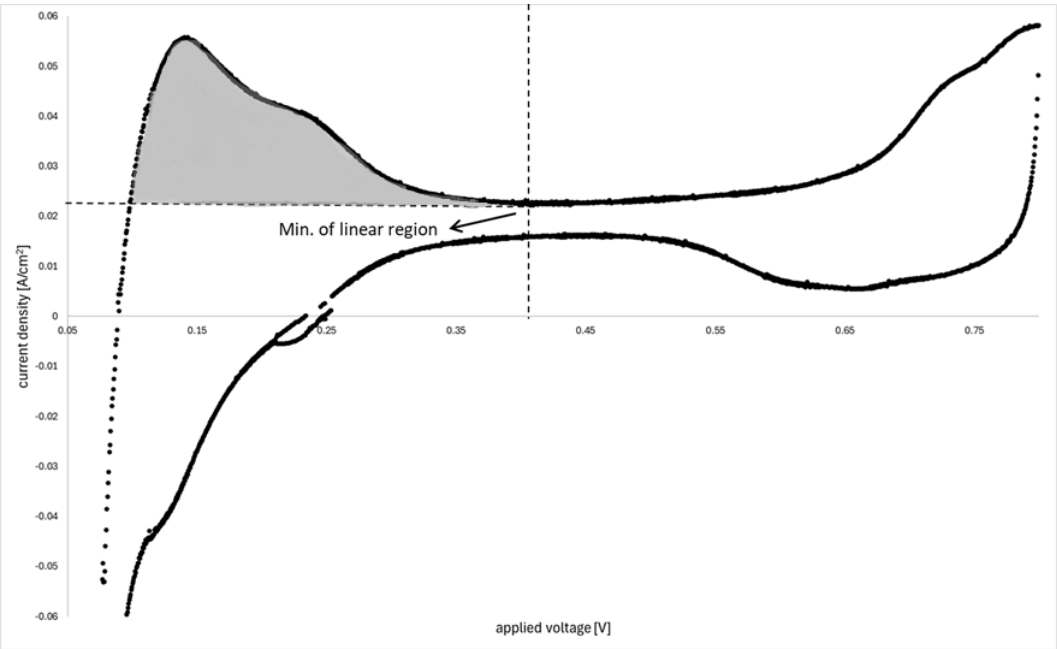

Figure 2.9. ECSA integration through hydrogen desorption peak

The catalyst loading, represented by C, should be specified in grams of catalyst. In this study, the fuel cells have a cathode catalyst loading of 0.45 mg/cm^2, and the active area is 5 cm^2. Therefore, the calculation is as follows:

$$\mathrm{C} = 0.45\ \frac{\mathrm{mg}}{\mathrm{cm2}} \times 5\ \mathrm{cm}^2 = 2.25\ \mathrm{mg\ platinum}$$

The proportionality constant S is the charge required to reduce a monolayer of protons on Pt. The proportionality constant of Pt equals 210 μC/cm^2 (18)The average value for the ECSA of the cells used in this work is 35 m^2/g Pt.

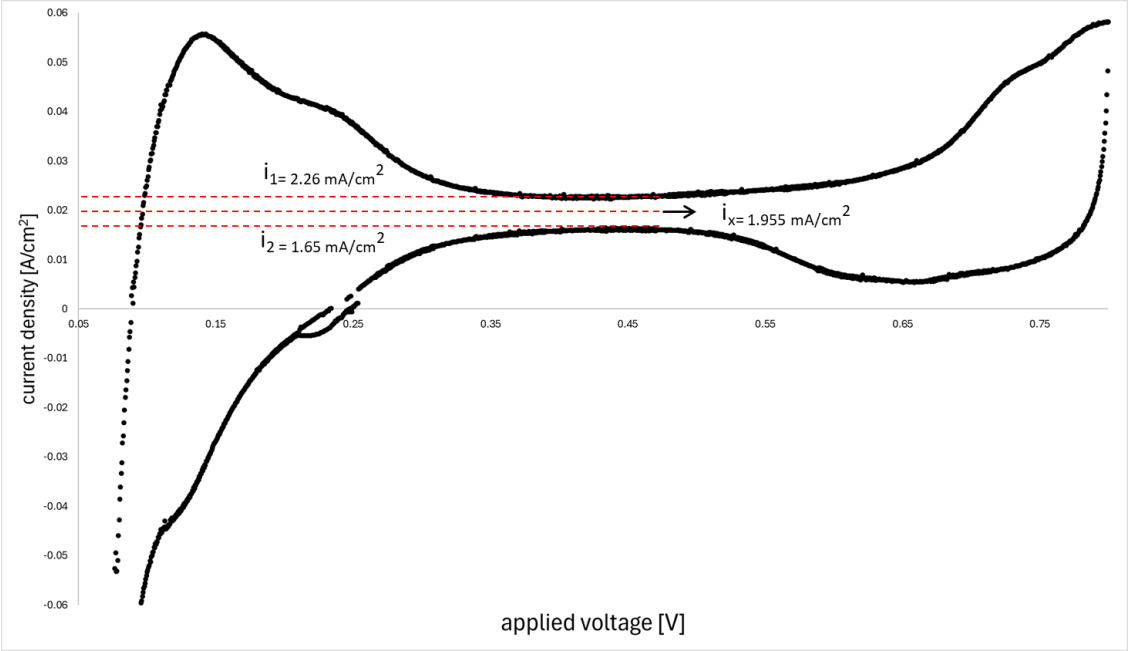

Figure 2.10. Extracting double layer capacitance current and crossover current from cyclic voltammogram

The double layer capacitance can also be determined by examining the double layer region of the voltammogram (0.35-0.5 V), as shown by the red rectangle in Figure 2.8. According to Equation 2.10, the current associated with double layer charging is half of the difference between the minimum current density of the upper portion i_1 in forward scan and the maximum current density of the lower portion i_2 in reverse scan. The currents are displayed in Figure 2.10.

$$i_{dl} = \frac{i_1 - i_2}{2} \qquad 2.10$$

By utilizing the double layer charging current, the double layer capacitance can be determined using Equation 2.11, where r represents the scan rate of the cyclic voltammogram:

$$\mathrm{C_{dl}} = \frac{\mathrm{i_{dl}}}{\mathrm{r}} \qquad 2.11$$

Furthermore, the current density linked to fuel (H_2) crossover from the anode to the cathode, as outlined in Equation 2.12 is represented by the midpoint between i_1 and i_2:

$$i_x = \frac{i_1 + i_2}{2} \qquad 2.12$$

Typical value for the C_{dl} for the cells used in this study is 30.5 mF/cm^2, and for the i_x is 4.4 mA/cm^2.

2.3.3. Electrochemical Impedance Spectroscopy

Electrochemical Impedance Spectroscopy (EIS) is another diagnostic technique used in electrochemistry to understand the behavior of systems like fuel cells. Unlike CV, which involves a linear sweep of voltage, EIS applies a sinusoidal wave with small amplitude and varying frequency. This wave is superimposed onto the system's voltage or current, and the response is measured. EIS provides insights into phenomena like charge transfer, mass transfer, and the double layer. The data obtained from EIS is typically presented in Nyquist plots, which display imaginary impedance (Z_{Im}) against real impedance (Z_{Re}) as shown in Figure 2.11. By varying the frequency and observing the system's response, parameters can be derived to model the system using equivalent electrical circuits.

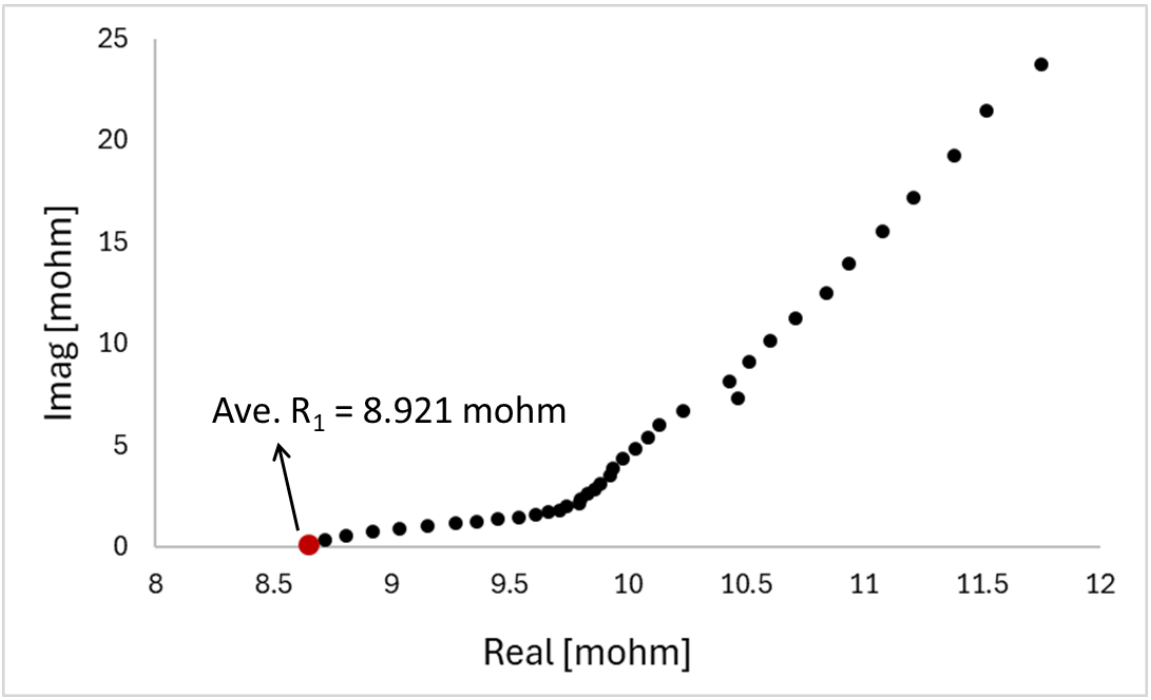

Figure 2.11. Nyquist plot

The Nyquist plot allows for the extraction of various parameters to create an equivalent electrical circuit model for a fuel cell. However, in this study, the focus is on the ohmic resistance, R1, also know as high frequency resistance (HFR). In physical terms, it indicates the total internal resistance within the cell. This resistance corresponds to the real component of the complex impedance at or near zero phase.

2.4. Post-Mortem Analysis

Electron microscopy techniques offer powerful tools for post-mortem analysis of PEM fuel cells, providing detailed insights into their structural and compositional characteristics at the micro- and nano-scale levels. Particularly, in this study, scanning electron microscopy (SEM) was used to obtain information about the MEA layer thicknesses. In addition, we employed transmission electron microscopy (TEM) techniques, including high-resolution transmission electron microscopy (HRTEM) and scanning transmission electron microscopy (STEM), to capture detailed images of the catalyst platinum nanoparticles. These images were used to obtain the size distribution of platinum catalyst nanoparticles in both fresh and degraded samples, which can provide useful information regarding the cathode electrode mechanisms. Furthermore, elemental analysis was performed using STEM energy dispersive X-ray spectroscopy (EDX) mapping to obtain elemental distribution of each MEA throughout its cathode electrode and membrane layers.

2.4.1. Scanning Electron Microscopy

MEA samples for SEM imaging were cut as rectangular (25 mm × 10 mm) sections from the middle of the cell and embedded in EpoThin epoxy resin, polished with the Struers Labo polishing system and carbon coated using Leica EM ACE200 vacuum coater. The Tescan Vega 3 SEM was used to acquire SEM images of the cross-sections at 2000x magnification, using the accelerating voltage of 20-25 kV, working distance 10-11 mm and backscattered electron mode. The thickness of the electrode was determined by integration of the electrode area with ImageJ and dividing by the length of the image for three arbitrary positions.

2.4.2. Transmission Electron Microscopy

Transmission Electron Microscopy (TEM) imaging and Energy Dispersive X-ray (EDX) mapping were performed using FEI Tecnai Osiris at 200 kV. For TEM analysis, MEA cross-section samples were prepared by cutting small sections using ultramicrotomy. Ultramicrotomy is a specialized technique in the field of microscopy that involves the preparation of ultrathin sections of specimens for examination under high-resolution TEM. The primary objective of ultramicrotomy is to produce slices of specimens that are thin enough (~100 nm) to allow electrons to pass through, enabling detailed imaging at the atomic or molecular level. The process typically begins with the embedding of the specimen in a resin or plastic material. For this work, after removing the GDL, a rectangular piece (~ 3 mm * ~10 mm) of the CCM samples were cut from the middle of the sample, placed into PELCO ® 20 Cavity Embedding Molds and cured in Araldite 502 resin overnight. Figure 2.12 shows the cured resin block encompassing the CCM sample.

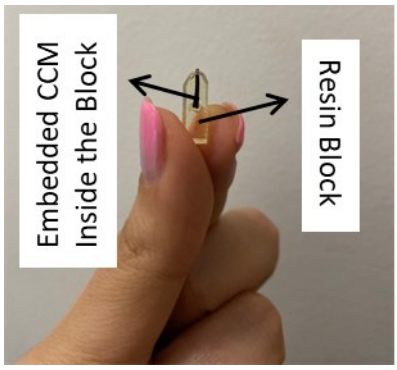

Figure 2.12. Cured resin block encompassing the CCM sample

This embedded specimen block, was then mounted onto a Leica UC7 ultramicrotome, and a double-edged razor blade was used for trimming the block. The goal of the trimming was to shape a very small trapezoid around the specimen. A tungsten knife was then used to cut ~ 300 nm thick section from the surface of the trapezoid. This is referred to as the facing step to ensure that the trapezoid face is smooth and even before the actual cutting process with diamond knife. The cutting was continued until reaching to the specimen. Subsequently, a diamond knife filled with DI water, as indicated in Figure 2.13 was used to cut the final sections with 100 nm thickness.

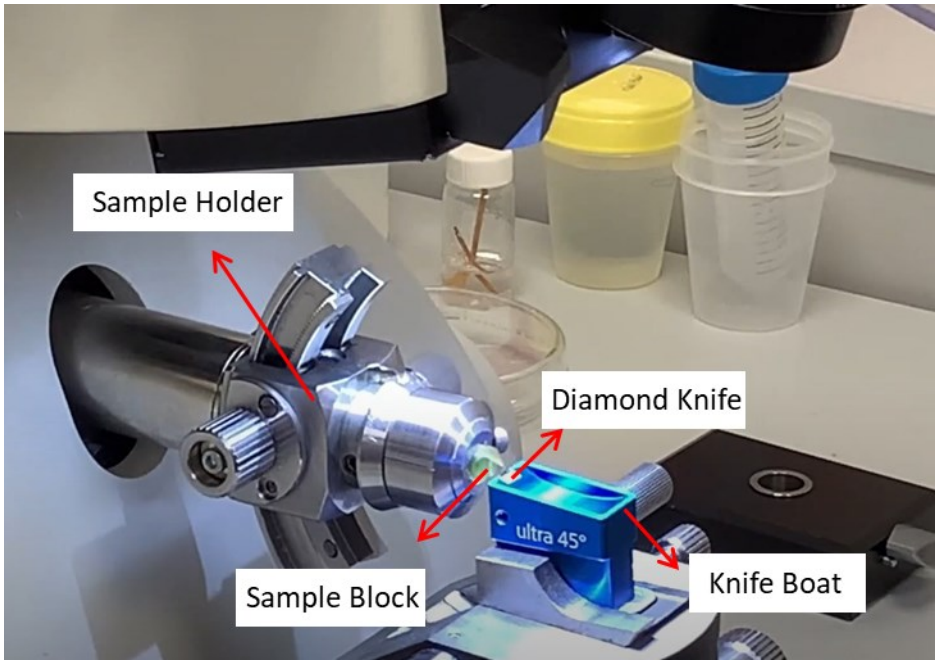

Figure 2.13. Ultramicrotomy setup

The resulting ultrathin sections floated on the water surface, as shown in Figure 2.14, were subsequently collected, and transferred onto 100-mesh Cu TEM grids. These grids provide structural stability and facilitate the handling of the ultrathin sections during subsequent microscopy procedures.

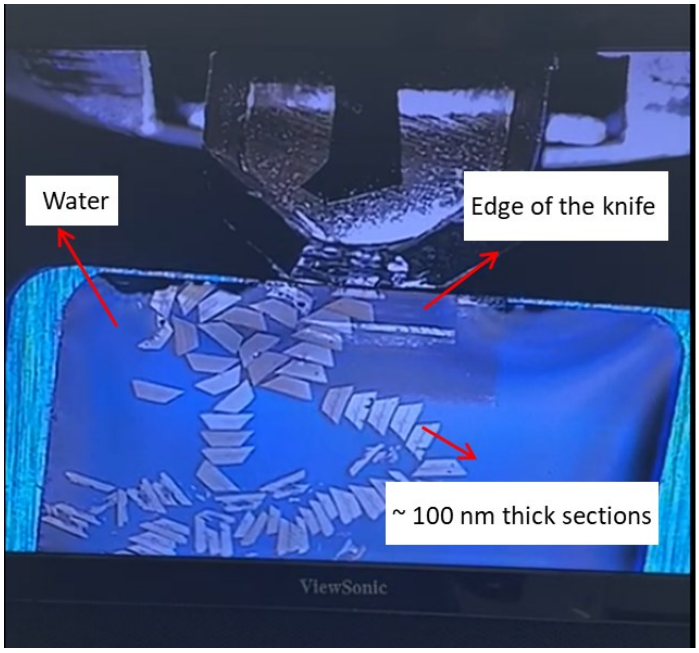

Figure 2.14. 100 nm thick CCM sections floated on water inside knife boat

After sample preparation, high-resolution STEM images were collected at 900 kx magnification, and Image J image processing software was utilized to measure 200 particles' size for each sample. Elemental analysis was conducted by collecting EDX elemental maps (600 × 900 pixels) at 7000x magnification with beam dwell time of 500 µs in STEM mode, using the Bruker SuperX EDX detectors.

Chapter 3. Statistical Analysis

In this work, we have studied the effect of three predictor variables including LPL, UPL dwell time, and LPL dwell time on the normalized ECSA, which is a continuous variable ranging from 0 to 1, after certain number of cycles. We treated the predictor variables as categorical variables, considering the smaller value for each predictor as the 'low/short' value and the larger value as the 'high/long' value. For example, the 0.6 V level of LPL is considered a low LPL level, while the 0.8 V level of LPL is considered a high LPL level. The goal it to compare the mean normalized ECSA across all LPL/ UPL dwell time/ LPL dwell time combinations. Each of these factors have 2 levels as summarized in Table 3.1. Therefore, the total number of experiments is equal to $2^3 = 8$. We have conducted only 6 out of the total eight number of possible experiments with the combination of these factors.

Table 3.1. Three independent factors along with their levels

Factor	LPL	UPL dwell time	LPL dwell time
Levels	0.6 and 0.8 V	3 and 10 s	3 and 10 s

Assuming that the fabricated MEAs were randomly assigned to each of the 6 experiments conducted in this study, one option to consider for statistical analysis could be a 3-way ANOVA model. As two experiments (LPL=0.6, UPL dwell time = 10 s, LPL dwell time = 10 s and LPL=0.8, UPL dwell time = 10 s, LPL dwell time = 10 s) have not been performed in this study, the terms for the interaction effects of UPL dwell time and LPL dwell time, as well as the term for the interaction effect of all three variables, have not been included in the ANOVA model. Equations 3.1- 3.3 represent the ANOVA model used here, along with its assumptions (78).

$$Y_{ijkl} = \mu + a_i + b_j + c_k + d_{ij} + e_{ik} + \varepsilon_{ijkl} \quad 3.1$$

where

$$a_1 = b_1 = c_1 = d_{1j} = d_{i1} = e_{1k} = e_{i1} = 0, \qquad for\ all\ i, j, k \quad 3.2$$

Assuming:

$$\varepsilon_{ijkl} \sim N(0, \sigma) \; and \; the \; \varepsilon'_{ijkl}s \; are \; independent \qquad 3.3$$

Definition of model variables are as follows:

Each of the factors can have any number of levels, denoted by i, j, and k for the LPL, UPL dwell time, and LPL dwell time factors, respectively, where:

LPL has i = 2 levels (1 = 0.6 V, 2 = 0.8 V);

UPL dwell time has j = 2 levels (1 = 3 s, 2 = 10 s);

LPL dwell time has k = 2 levels (1 = 3 s, 2 = 10 s);

Y_{ijkl}: The observed value of the normalized ECSA after 20,000 cycles in the lth MEA for the ith level of the LPL, the jth level of the UPL dwell time, and the kth level of the LPL dwell time;

μ: The mean of the normalized ECSA after 20,000 cycles for the AST with LPL of 0.6 (i = 1), UPL dwell time of 3 seconds (j = 1), LPL dwell time of 3 seconds (k = 1). This AST is considered the reference category;

a_i : The main effect of ith level of the LPL. The interpretation of a_i is the deviation of the normalized ECSA after 20,000 cycles for MEA aged by the AST with LPL of i from the mean normalized ECSA at LPL level of 0.6 V;

b_j: The main effect of jth level of the UPL dwell time;

c_k: The main effect of kth level of the LPL dwell time;

d_{ij}: The interaction effect between the ith level of the LPL and the jth level of the UPL dwell time;

e_{ik}: The interaction effect between the ith level of the LPL and the kth level of the LPL dwell time;

ε_{ijkl}: The random error term representing the variability of the l[th] MEA not explained by the model.

Examining model assumptions, assuming that the fabricated MEAs were randomly assigned to each of the 6 experiments, the Y_{ijkl}'s (normalized ECSA after 20,000 cycles) can reasonably be treated as independent. The next assumption concerns the homogeneity of variance across groups of experiments. In this study, the reference AST was repeated three times, resulting in a standard deviation of 0.07 for the mean normalized ECSA after 20,000 voltage cycles. The other 5 ASTs were repeated only once, and therefore, the standard deviation cannot be defined for them. However, the experimental conditions, such as temperature, pressure, flow, and measurement techniques, were ensured to be as similar as possible. Therefore, the assumption that the variability observed in the reference AST is representative of the variability in the other five ASTs sounds reasonable. Lastly, the normality of the residuals should be assessed. According to Figure 3.1, which shows the histogram of residuals, the distribution of the residuals is approximately symmetric, and a normal distribution provides a reasonable approximation. Considering that some of the assumptions might be inaccurate to some degree, we cautiously proceeded with formal inference about the mean normalized ECSA using the ANOVA model.

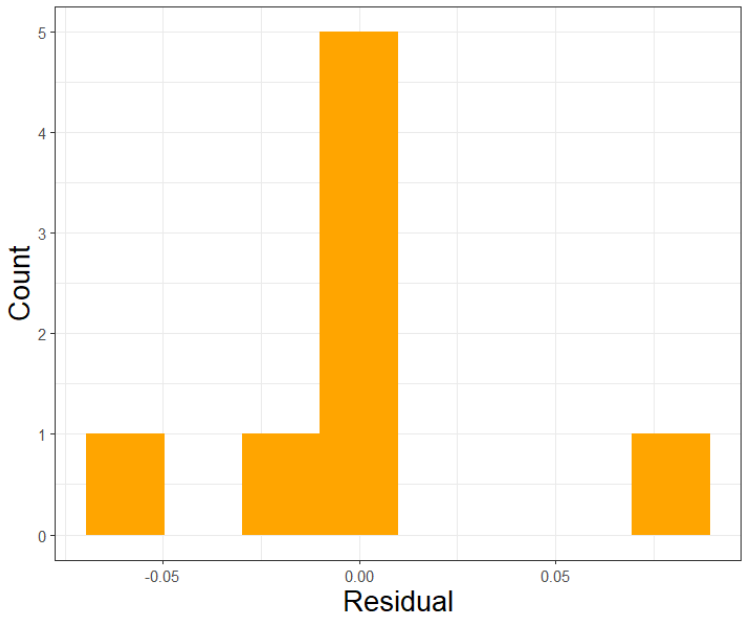

Figure 3.1. The histogram of the residuals that follows the normal distribution

After fitting the model, Table 3.2 and Table 3.3 summarize the parameters of the model and other statistical measures calculated, respectively:

Table 3.2. Model parameters when considering LPL: UPL dwell time and LPL: LPL: LPL dwell time interaction effects

Model Parameters	Estimate	Standard Error	t-value	P-value (Pr (> |t|))
μ	0.448	0.041	11.071	0.008
a_2	0.262	0.081	3.238	0.084
b_2	-0.281	0.081	-3.470	0.074
c_2	-0.269	0.081	-3.320	0.08
d_{22}	-0.072	0.128	0.568	0.628
e_{22}	0.194	0.128	1.516	0.269

Table 3.3. Statistical measures

Statistical Measures	Value
Residual standard error (â)	0.0701
R-squared (R^2)	0.963
Overall F-statistic on 5 and 2 degrees of freedom	10.48
p-value for the overall F-test	0.0894

According to the table, R-squared is equal to 0.96, which means that LPL, UPL dwell time, and LPL dwell time explain ca. 96% of the variation in the normalized ECSA after 20,000 cycles, which is a significant number. Furthermore, the p-value of the overall F-test, 0.089, suggests that at the 10% significance level LPL, UPL dwell time, and/or LPL dwell time affect the mean normalized ECSA after 20,000 cycles. In other words, the difference between the mean normalized ECSA across the various LPL/UPL dwell time/LPL dwell time combinations is statistically different at 10% significance level for at least two of the experiments. To obtain more information, the results of the ANOVA analysis is also summarized in Table 3.4.

Table 3.4. ANOVA parameters when considering LPL: UPL dwell time and LPL: LPL: LPL dwell time interaction effects

Response: normalized ECSA after 20,000 cycles					
	Df	Sum of Squares	Mean Squares	F-value	P-value (Pr (>F))
LPL	1	0.145	0.145	29.416	0.032
UPL_dwell_time	1	0.055	0.055	11.261	0.078
LPL_dwell_time	1	0.046	0.046	9.427	0.092

LPL: UPL_dwell_time	1	0.000	0.000	0.002	0.97
LPL: LPL_dwell_time	1	0.011	0.011	2.297	0.269
Residuals	2	0.01	0.005		

According to Table 3.5, there is no statistically significant interaction effect between either LPL and UPL dwell time or LPL and LPL dwell time at the 5% level, as their p-values of the F-test are greater than 0.05. This means that the effect of LPL on ECSA loss is the same for both short (3 seconds) and long UPL/LPL (10 seconds) dwell times, aligning with the results in the next chapter. Comparing the difference in ECSA loss between AST 0.6-0.95V_3-3s and 0.8-0.95V_3-3s (blue circles/curve and orange circles/curve in Figure 4.6, respectively) with the difference in ECSA loss between AST 0.6-0.95V_10-3s and 0.8-0.95V_10-3s (yellow circles and green circles/curve in Figure 4.6, respectively) shows that regardless of whether the LPL dwell time is 3 seconds or 10 seconds, changing the LPL value from low (0.6 V) to high (0.8 V) results in a significant decrease in ECSA loss. This suggests that the main effect of LPL can explain most of the variability in ECSA loss across both short and long LPL dwell times. The same holds true for the interaction effect of LPL and UPL dwell time. Therefore, the model was refitted without considering the interaction effects to draw stronger conclusions about the main effects. Table 3.5 and Table 3.6 present the model parameters and the results of the ANOVA analysis, respectively, for the case when all interaction effects are omitted from the model.

Table 3.5. Model parameters when neglecting all interaction effects

Model Parameters	Estimate	Standard Error	t-value	P-value (Pr (> |t|))
μ	0.429	0.039	11.044	0.0004
a_2	0.338	0.054	6.157	0.0035
b_2	-0.264	0.064	-4.092	0.0149
c_2	-0.191	0.064	-2.962	0.0415

Table 3.6. ANOVA parameters when neglecting all interaction effects

Response: normalized ECSA after 20,000 cycles					
	Df	Sum of Squares	Mean Squares	F-value	P-value (Pr (>F))
LPL	1	0.145	0.145	27.369	0.006
UPL_dwell_time	1	0.055	0.055	10.477	0.032
LPL_dwell_time	1	0.046	0.046	8.771	0.041

Residuals	4	0.021	0.005

Neglecting the interaction effects led to smaller P-values for both t-tests and F-tests, compared to values in Table 3.2 and Table 3.4, leading to stronger conclusions regarding the main effects. With no evidence of interaction effects, we can informally draw some inferences on the main effects of the factors. The interpretation of the conclusions about the main effects of the predictors should be treated cautiously as, due to the multiple testing problem, the family-wise error rate will not be controlled at the 5% level. However, they are still beneficial for providing some preliminary statistical insight.

Figure 3.2 demonstrates the pareto chart of absolute model coefficients derived from Table 3.5 for the main effects. The longest bar corresponds to the LPL with the highest absolute coefficient, which is 0.338, representing that it contributes the most to the ECSA loss. Furthermore, as noted in the ANOVA results presented in Table 3.6, LPL has also the largest sum of squares, 0.145. With the highest sum of squares value, LPL explains the largest variability of the normalized ECSA, suggesting that LPL could be the most influential factor in determining the normalized ECSA. After explaining the variability due to LPL, the sum of squares for UPL dwell time is the next largest, with a p-value of 0.006, noted in Table 3.6. This suggests that UPL dwell time is also a significant factor in determining normalized ECSA at the 5% level, depicted in the pareto chart as the second most important variable with -0.264 as its coefficient in the model. Adjusting for these two factors, LPL dwell time is also significant in explaining the variability of the normalized ECSA at the 5% level, indicated by its p-value being smaller than 0.05. Its coefficient in the model, noted as -0.191 in Table 3.5, is the smallest coefficient, in absolute value, among the three variables. These suggest that although LPL dwell time is still influential, its impact on ECSA loss is lower than that of the other two factors after controlling for their effects.

The red line in Figure 3.2 represents the cumulative percentage of the total absolute coefficients of the variables, illustrating the cumulative contribution of each variable to the overall ECSA loss. It is worth mentioning that a significant portion, over 75%, of the cumulative impact of these variables is attributed to the main effects of LPL and UPL dwell time.

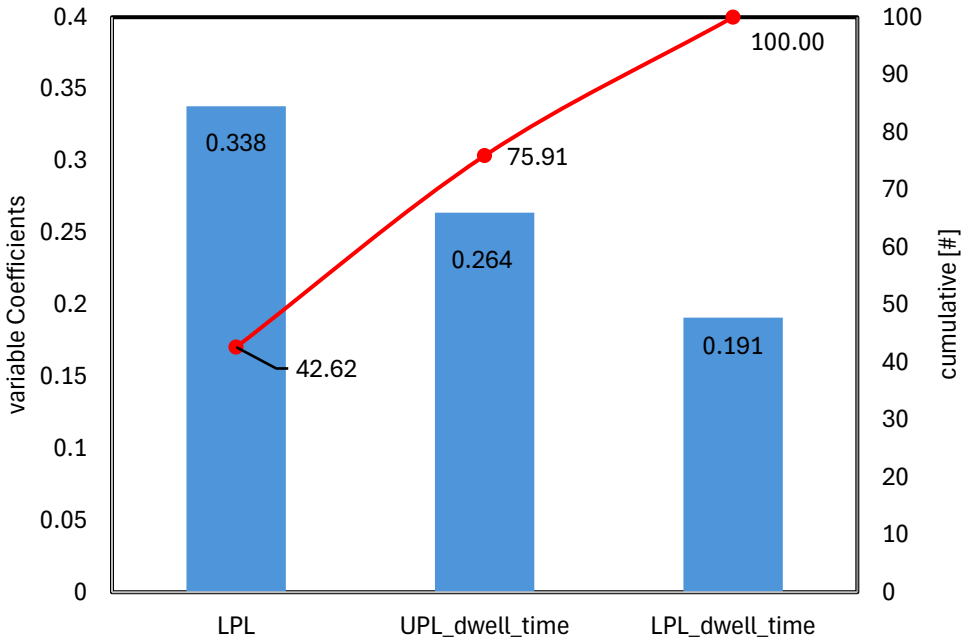

Figure 3.2. Pareto chart of absolute model coefficients for main effects

Chapter 4.

Results and Discussion

The sections below present the results obtained through the methods outlined in the preceding chapter. Initially, baseline experiments were conducted to ensure repeatability and to assess the variability between fuel cells. Secondly, post-mortem analyses were discussed to offer insights into the degradation mechanisms. Thirdly, the degradation data from the AST experiments were compared to investigate the impact of LPL and dwell time on ECSA loss. Finally, the possibility of membrane degradation and carbon corrosion during voltage cycling AST was examined.

4.1. Baseline

4.1.1. Beginning of Life

In this study, the fuel cells tested were fabricated and assembled in a standardized manner, and experimental procedures, explained in Chapter 2, were kept constant to ensure consistency. However, because of the complex processes involved in fuel cell fabrication and operation, the performance of the fuel cell specimens exhibited variability. The first objective of the work was to characterize this variance in the beginning of life (BOL) performance. Table 4.1 provides a summary of the fuel cell specimens analyzed, with eight BOL samples subjected to degradation testing – 3 for baseline load cycling (AST 0.6-0.95V_3-3s) and five for other ASTs.

Table 4.1. Summary of degraded fuel cells

Number of BOL cells	Number of degraded cells	Mean Pt loading (Ca/An) [mg/cm^2]	Std. dev. of Pt loading (Ca/An) [mg/cm^2]
8	8	0.45/0.25	0.02/0.05

It's important to note that while eight samples are presented in Table 4.1, the total number of fuel cell specimens tested initially before refining the experimental design was over 40. The analysis presented in this section only focuses on the samples shown in Table 4.1, which were tested under fully optimized circumstances in terms of fabrication,

assembly, and testing procedures using the test station. This ensures that the results are based on standardized conditions for comparison and evaluation.

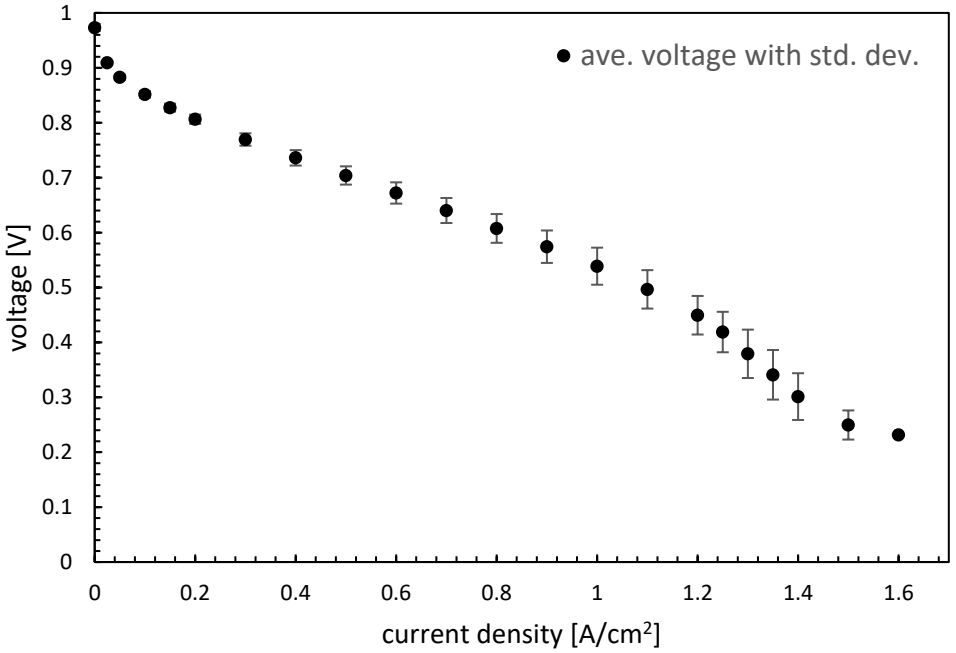

Figure 4.1. Average fuel cell polarization data with standard deviation for all 8 cells at their BOL

Figure 4.1 displays the average performance of fuel cells, including their standard deviations, across varying current densities. The performance variance is less than 6 mV up to 0.1 A/cm^2, and the variance ranges between 7 mV and 20 mV up to 0.6 A/cm^2. From there, it will increase as current density increases until it reaches the maximum variance of ca. 45 mV at 1.3 A/cm^2. The variation in performance primarily stems from slight disparities in the catalyst layer structure, which is highly dependent on factors such as size and distribution of particles in the catalyst ink, as well as the uniformity of ink deposition. The structural variability significantly influences water management within the fuel cell, as evidenced by the substantial performance differences in mass-transport region (above 1 A/cm^2) illustrated in Figure 4.1. Additionally, it was observed that performance in this region was significantly impacted by slight changes in gas temperatures. Even minor deviations of 1°C in temperature can significantly affect water management, thereby influencing overall performance. In contrast, fuel cell assembly being simpler to regulate, had a lesser impact on performance variation.

Alongside assessing the fuel cell performance under load using a polarization curve, two other diagnostic techniques were utilized to monitor degradation: cyclic voltammetry (CV), to observe changes in ECSA, cross-over current, and double-layer capacitance; and electrochemical impedance spectroscopy (EIS), to monitor shifts in ohmic resistance. The mean ECSA, determined from CVs as explained in Section 2.3.2, was 40.9 m^2/g of platinum, with a standard deviation of 8.3 m^2/g of platinum. Hence, as the minimum ECSA loss resulting from the degradation of these eight cells amounts to almost 16 m^2/g (associated with AST 0.8-0.95V_3-3s after 30,000 cycles), the ECSA loss is distinguishable across all cells considering the calculated ECSA variation, especially when monitoring the changes to a given MEA with known ECSA at BOL.

The average fuel cell cross-over current density i_x and double-layer capacitance C_{dl} were calculated to be 4.4 mA/cm^2 and 30.5 mF/cm^2 with standard deviations of 1.2 mA/cm^2 and 6.2 mF/cm^2, respectively. Furthermore, the average ohmic resistance R_1 calculated from the Nyquist plot as explained in Section 2.3.3 was found to be 45.5 $m\Omega.cm^2$ with a standard deviation of 3.5 $m\Omega.cm^2$. Table 4.2 provides a summary of the means and standard deviations derived from the CVs and Nyquist plots, presenting measurements for ECSA, i_x, C_{dl}, and R_1, frequently utilized in degradation tracking.

Table 4.2. Electrochemical measurements for all BOL samples

	ECSA [m^2/g]	Crossover current density [mA/cm^2]	Double layer capacitance [mF/cm^2]	R_1 [$mohm.cm^2$]
Mean	40.9	4.4	30.5	45.5
Std. dev.	8.3	1.2	6.2	3.5

4.1.2. End of Test

To establish a baseline for the degradation process, the standard cathode AST recommended by DOE to evaluate electrocatalyst degradation (30), which is square wave voltage cycling with LPL=0.6 V and 3 seconds spent at each vertex, was conducted three times. Figure 4.2 illustrates comparison of the average polarization curves of these three degraded cells after 30,000 cycles, including standard deviation, against the average polarization curve of all eight cells at BOL. As depicted in Figure 4.2, the voltage error bars begin to overlap around 0.7 A/cm^2. Consequently, voltages associated with currents below

0.7 A/cm^2 offer a more suitable reference for monitoring voltage degradation throughout the process.

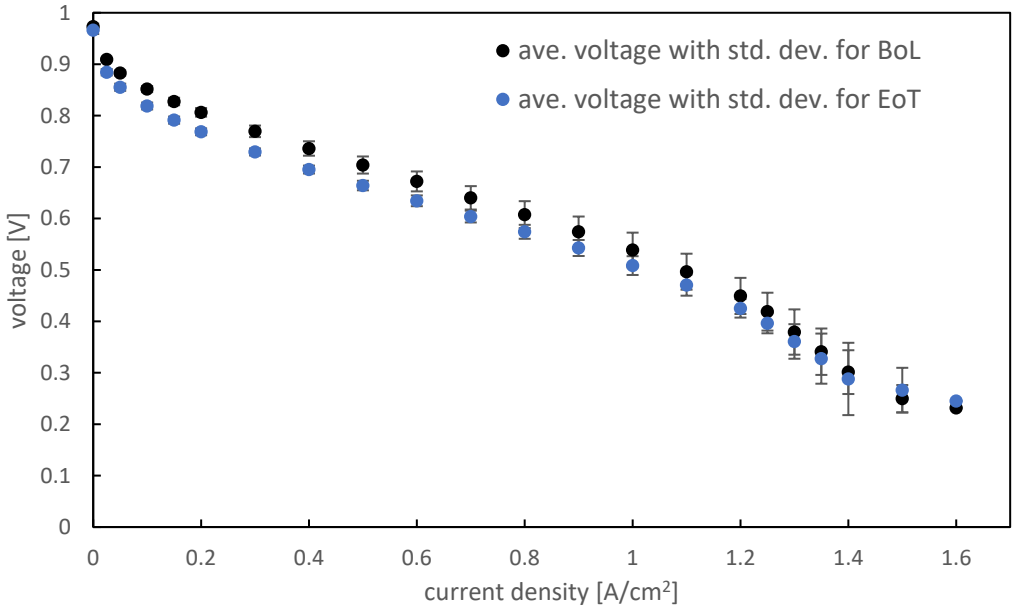

Figure 4.2. Performance comparison between eight BOL samples and three degraded samples from the baseline AST.

The failure criterion for determining the EOL of the MEAs in this work was considered 10% of the BOL cell voltage at 0.6 A/cm^2 current density, which is a common threshold for degradation studies (79,80). To incorporate the variations introduced by the degradation process, the average normalized cell voltage with its standard deviation was plotted for the baseline AST in Figure 4.3. According to the plot, the normalized voltage after 30,000 cycles for baseline AST with three repeats is 92.7% of the initial voltage at 0.6 A/cm^2 with 0.5% standard deviation. This means 7.3% voltage degradation with the same standard deviation, which corresponds to only $\frac{0.5\%}{\sqrt{3}} \simeq 0.3\%$ standard error for the mean percentage of voltage degradation. Therefore, 10% voltage loss at 0.6 A/cm^2 will allow for tracking of changes in performance of fuel cells.

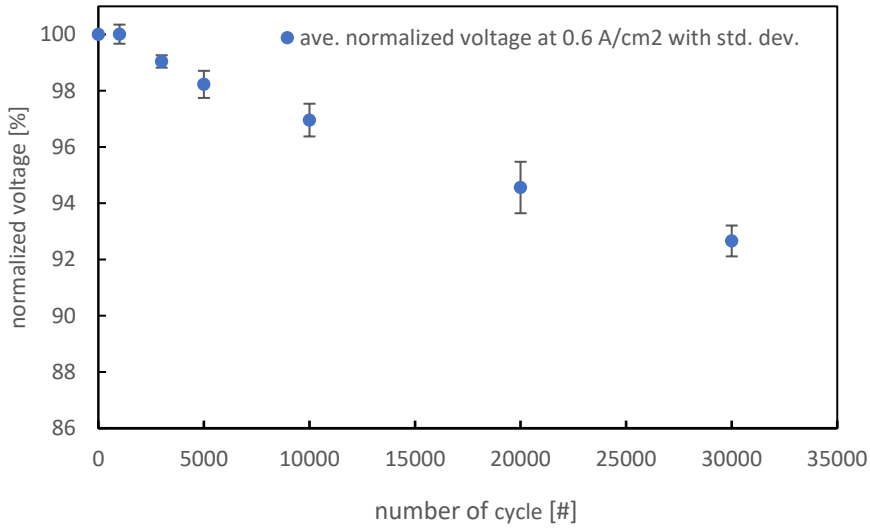

Figure 4.3. Average normalized cell voltage at 0.6 A/cm^2 for three degraded cells through baseline AST

The main focus of the study is to monitor normalized ECSA loss throughout the aging process across various ASTs, therefore it is imperative to determine the variation of this parameter. Figure 4.4 depicts the relative change in ECSA to its initial value ($ECSA_{BOL}$), during voltage cycling in the baseline AST experiment, conducted three times. The average ECSA loss caused by the baseline degradation is roughly 65% after 30,000 cyles with 5% standard deviation. variance.

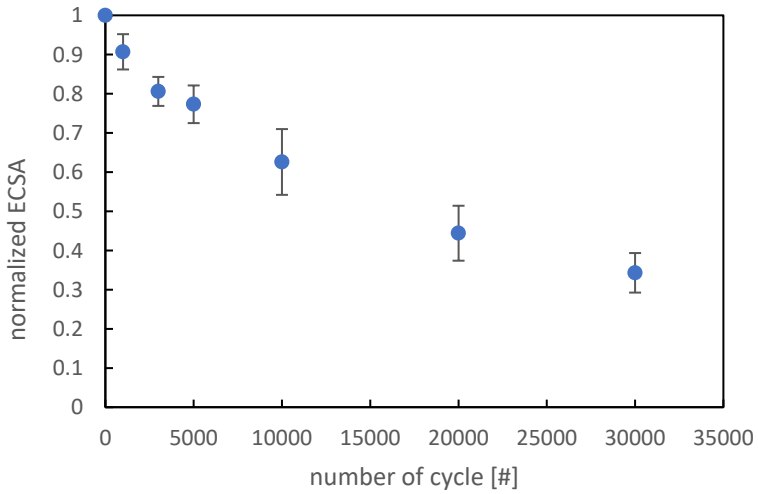

Figure 4.4. Average normalized ECSA to its initial value with the standard deviation for three degraded cells by baseline AST

4.2. Catalyst Degradation

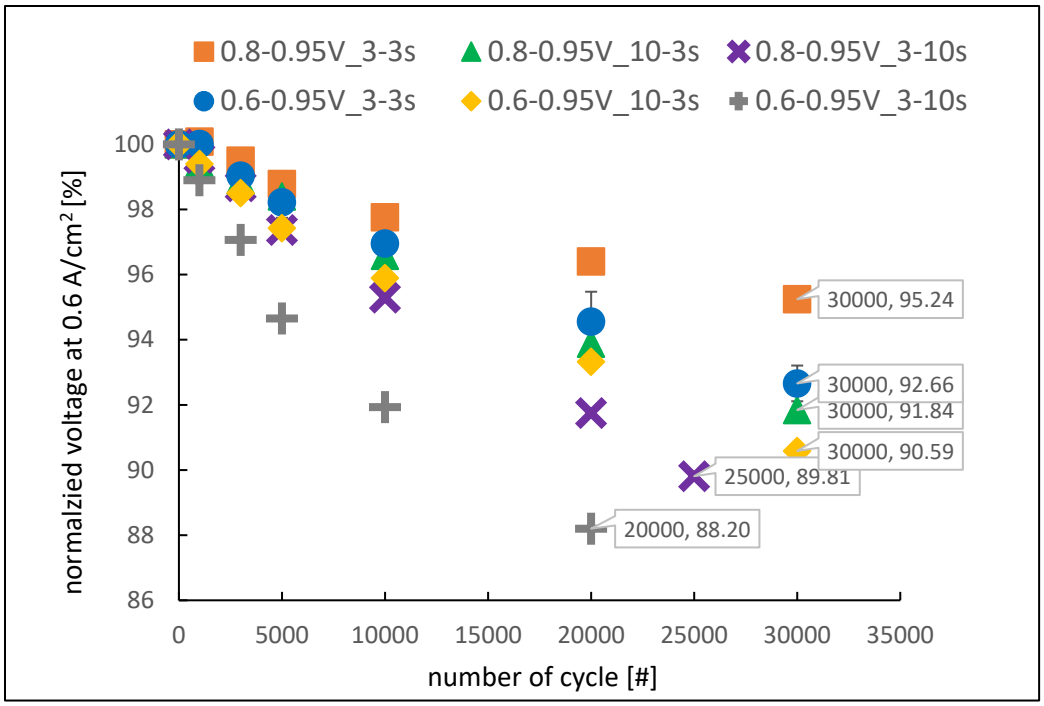

Figure 4.5. Normalized cell voltage at 0.6 A/cm² over the number of voltage cycles; the error bars of baseline AST 0.6-0.95V_3-3s represent the standard deviation from three measurements.

Figure 4.5 shows the normalized cell voltage at 0.6 A/cm² relative to the cell voltage at BOL, extracted from the polarization curve data, versus the number of voltage cycles (NoC) over the aging course. The cell voltage decreases for all cells as the number of cycles increases throughout the aging process. The rate of performance loss varies depending on the AST profile, which will be discussed later. As shown in the plot, cells were stopped at cycle numbers below 30,000 if they reached the 10% failure criterion, which was the case for AST 0.8-0.95V_3-10s (purple circles) and AST 0.6-0.95V_3-10s (grey circles).

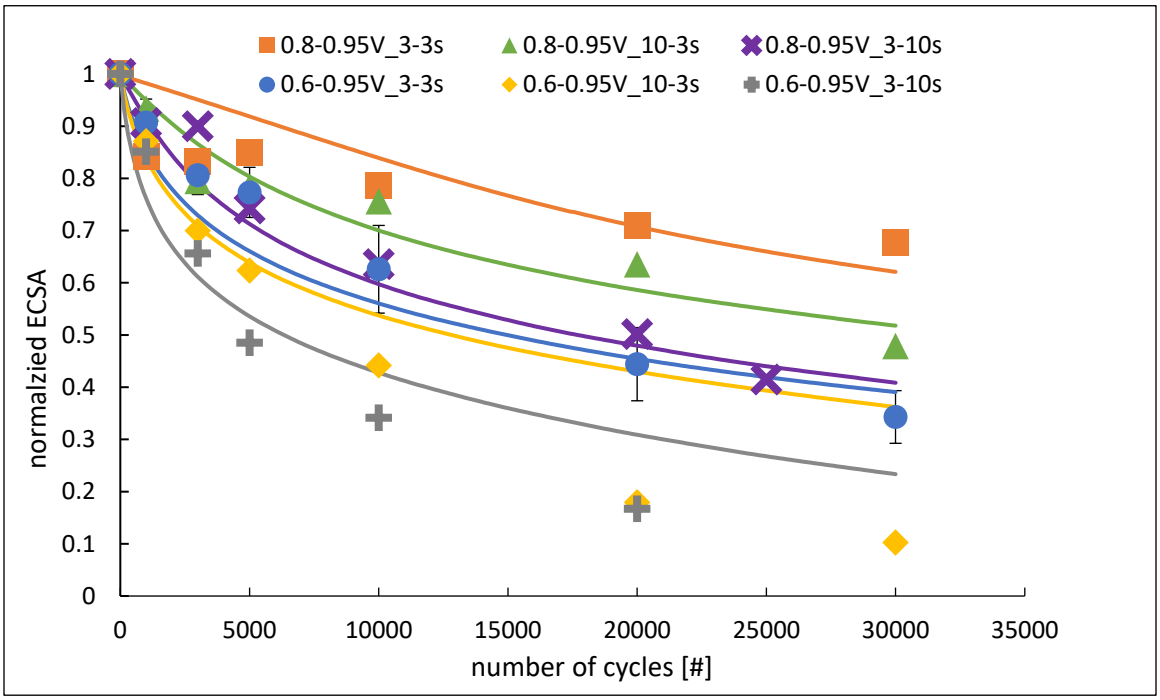

Figure 4.6. Normalized cathode ECSA (i.e., ECSA/ECSA$_{BoL}$) plotted vs the number of cycles. The circles show the measured experimental data, and the solid line is the prediction from a theoretical model. The error bars of the baseline AST 0.6-0.95V_3-3s represent the standard deviation from three measurements.

Figure 4.6 shows the development of the normalized ECSA to its initial value (ECSA$_{BOL}$) over the number of voltage cycles throughout the aging process for all six ASTs at two potential limits (LPL=0.6 V and 0.8 V) for various combinations of LPL and UPL dwell times (see Table 1.2), but with fixed UPL of 0.95 V. As mentioned previously, AST 0.6-0.95V_3-3s (blue circles) was repeated three times as the baseline experiment to obtain the variance of the degradation tests while the rest of the experiments were conducted once. The error bars of AST 0.6-0.95V_3-3s (blue circles) indicate the standard deviation. The circles show the measured data, and the solid lines show normalized ECSA results from a theoretical model for Pt degradation recently proposed by Shojayian and Kjeang (48). The model was executed to specifically simulate the six ASTs conducted in this study, and the simulation results are included in the thesis to provide theoretical support for the experimental outcomes. In this model, the main Pt degradation processes within the cathode electrode that are expected to occur under load cycling, including platinum dissolution and redeposition (Equation 1.5), platinum oxide formation (Equation 1.6), and platinum ion formation through chemical dissolution during operation (Equation

1.7), were simulated using the Butler-Volmer kinetic approach detailed in Reference (43). The assumed reaction rate equations utilized in the model for these reactions are explained in Appendix A. Shojayian and Kjeang adopted a zero-dimensional model to minimize the computational cost while capturing the essential cathode degradation dynamics. Consequently, spatial phenomena such as platinum ion migration and temperature and concentration gradients were disregarded, aligning with previous research efforts (53,81,82). The developed Pt degradation model has been rigorously validated with a variety of operating conditions including different UPLs, LPLs, temperatures, and potential cycles. The reader is referred to Reference (48) for the details of the model and the validation results.

The ECSA decay trend predicted by the model is in a reasonable agreement with the measured ECSA from the experiments for most of the cases, considering the ECSA degradation variation observed at the baseline (0.6-0.95V_3-3s) AST (blue circles). Only for AST conditions labeled as 0.6-0.95V_10-3s (yellow circles/curve) and 0.6-0.95V_3-10s (grey circles/curve), the experimental measurements deviate from the model prediction after 5000 cycles. This deviation could potentially arise from the constraints inherent in the zero-dimensional nature of the model. A comprehensive discussion addressing this hypothesis will be presented later in the thesis.

It is worth noting that the observed trend of normalized ECSA over cycles is consistent across all AST profiles and aligns with existing literature (59,60,64,67,83). Initially, there is a rapid decrease in ECSA as the number of cycles increase, followed by a slowdown in the rate of ECSA loss. This pattern was also observed in experiments involving potential cycling in a rotating disk electrode configuration (84). It is explained by the concept of a critical "quasi" stable particle size. Once the platinum reaches this stable particle size, its degradation rate decreases, leading to a slower decline in ECSA.

4.2.1. Discussion on the Catalyst Degradation Mechanism

STEM bright field (STEM-BF) images depicted in Figure 4.7 illustrate the platinum catalyst particles near the cathode-membrane interface within degraded MEA samples at their EOT condition. Upon comparison with Pt particles at the same cathode location at BOL condition in Figure 4.8, notable particle growth is evident across all degraded samples. In addition to visual observation from images, a quantitative comparison was

made by measuring the mean particle size of platinum particles at two specific locations within the catalyst layer: near the cathode-membrane interface, denoted as "cathode-membrane" and adjacent to the cathode–GDL interface, labeled as "cathode-GDL." These measurements along with their standard deviations are summarized in Table 4.3.

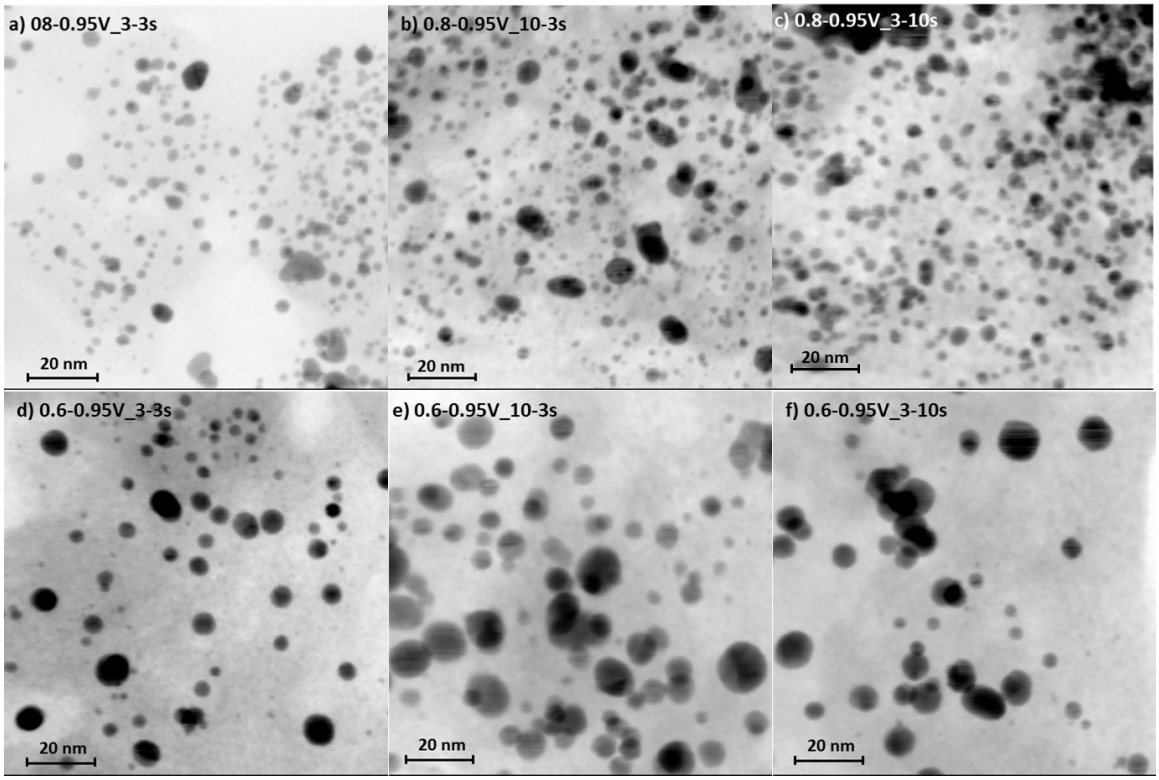

Figure 4.7. Post mortem STEM-BF images (at 900 kx magnification) of Pt particles in the cathode catalyst layer close to the membrane interface for the six MEAs degraded by AST: (a) 0.8-0.95V_3-3s, (b) 0.8-0.95V_10-3s, (c) 0.8-0.95V_3-10s, (d) 0.6-0.95V_3-3s (baseline), (e) 0.6-0.95V_10-3s, (f) 0.6-0.95V_3-10s

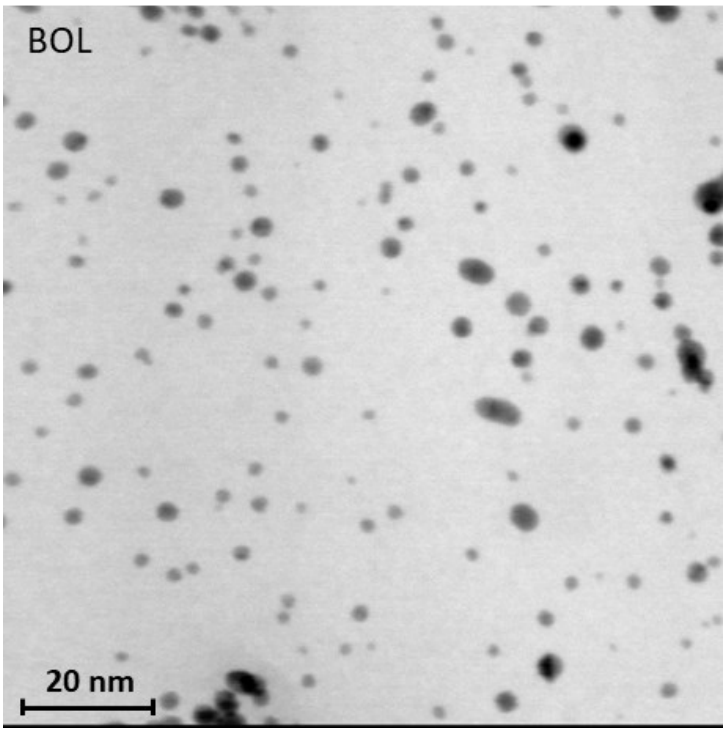

Figure 4.8. Reference STEM-BF image (at 900 kx magnification) of Pt particles in the cathode catalyst layer region close to the membrane interface from the pristine MEA at BOL condition

The quantitative analysis reveals a notable increase in particle size in the cathode-membrane interface location compared to the BOL condition, with growth rates varying significantly across different stress tests. Specifically, the mean particle size exhibited a 20% increase from BOL in the least degrading AST (0.8-0.95V_3-3s) with lowest of ECSA loss (see orange circles/curve in Figure 4.6), while experiencing a remarkable 150% increase from BOL in the harshest AST (0.6-0.95V_3-10s) with highest ECSA loss (see grey circles/curve in Figure 4.6). Accordingly, Figure 4.9 is a scatter plot demonstrating the correlation between normalized ECSA and the overall mean particle size of Pt particles in CCL, including particles at cathode-membrane and cathode-GDL interfaces, at EOT. In this plot, only the point corresponding to the baseline AST, which was repeated three times, shows error bars that represent the standard deviation. The rest of the experiments were repeated only once and therefore do not include error bars. The plot clearly shows that as the Pt particles become larger the normalized ECSA decreases. The difference in the particle size growth rate for different ASTs is caused by the variations in LPL levels, as well as dwell times, which will be thoroughly discussed in subsequent sections. The Pt particles located on the opposite side of the catalyst layer, in proximity to the GDL, have

also undergone size enlargement; nevertheless, for most cases their particle growth is comparatively slightly less than that observed for particles close to the cathode-membrane interface.

Table 4.3. Mean particle size of cathode Pt particles with their standard deviation for two locations within the catalyst layer close to the cathode-membrane and cathode-GDL interfaces

Procedure	Mean particle size (nm)_cathode-membrane	Standard deviation (nm)_ cathode-membrane	Mean particle size (nm)_cathode-GDL	Standard deviation (nm)_cathode-GDL
BOL	2.5	0.9	2.3	0.8
0.8-0.95V_3-3s	3.0	1.1	3.2	1.6
0.8-0.95V_10-3s	3.4	1.9	3.2	0.9
0.8-0.95V _3-10s	3.1	1.2	3.5	1.3
0.6-0.95V _3-3s	4.8	2.1	4.1	1.8
0.6-0.95V _10-3s	6.3	2.4	3.8	1.3
0.6-0.95V _3-10s	6.3	2.8	5.7	3.0

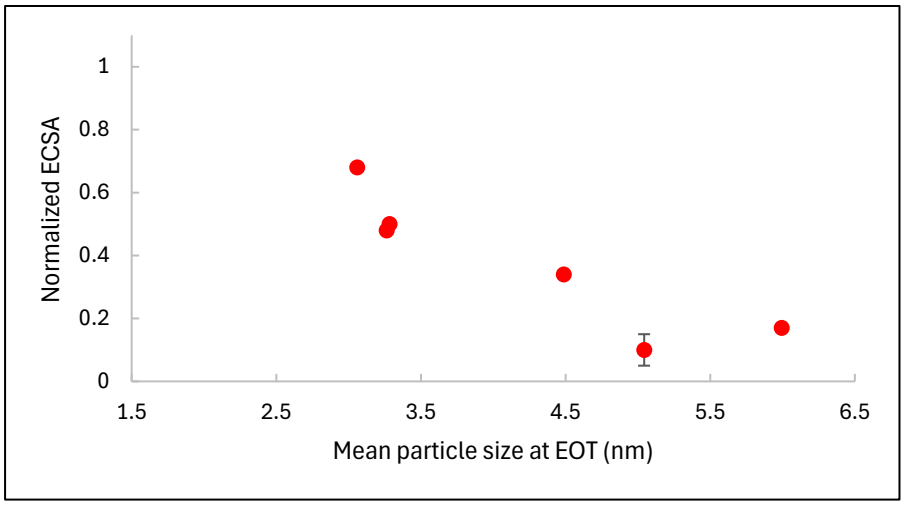

Figure 4.9. Scatter plot illustrating the direct relationship between the mean size of Pt particles in CCL at EOT and normalized ECSA; the point with error bars corresponds to the baseline AST, which was repeated three times. The error bars represent the standard deviation.

The particle growth near the cathode-membrane interface observed in the STEM-BF images is believed to be due to Pt dissolution/redeposition leading to Ostwald ripening phenomenon. The SEM images of the MEA cross-sections, shown in Figure 4.10, corroborate this hypothesis. While there is no Pt band in the membrane in the SEM image

at the BOL state (Figure 4.11), a Pt band can be seen at ca. 5 μm into the membrane for all six ASTs (see Figure 4.10). The position of the Pt band is affected by the hydrogen and oxygen partial pressures during voltage cycling (85), and since these parameters remained constant across all experiments, the Pt band consistently appears at ca. 5 μm within the membrane. Additionally, a distinct ca. 4 μm thick dark Pt-depleted region in the cathode catalyst layer along its interface with the membrane is observed in all samples, while concurrently, Pt is retained on the opposite side of the cathode near the GDL. This heterogeneous distribution of Pt within the catalyst layer is reported to be strong evidence pointing towards dominating Pt dissolution/redeposition mechanism (86,87). Even though the dark Pt-depleted region is difficult to recognize for some of the samples, the presence of the Pt band in all cases indicates that Pt must have undergone dissolution near the membrane interface, creating Pt ions that are able to move and deposit into the membrane.

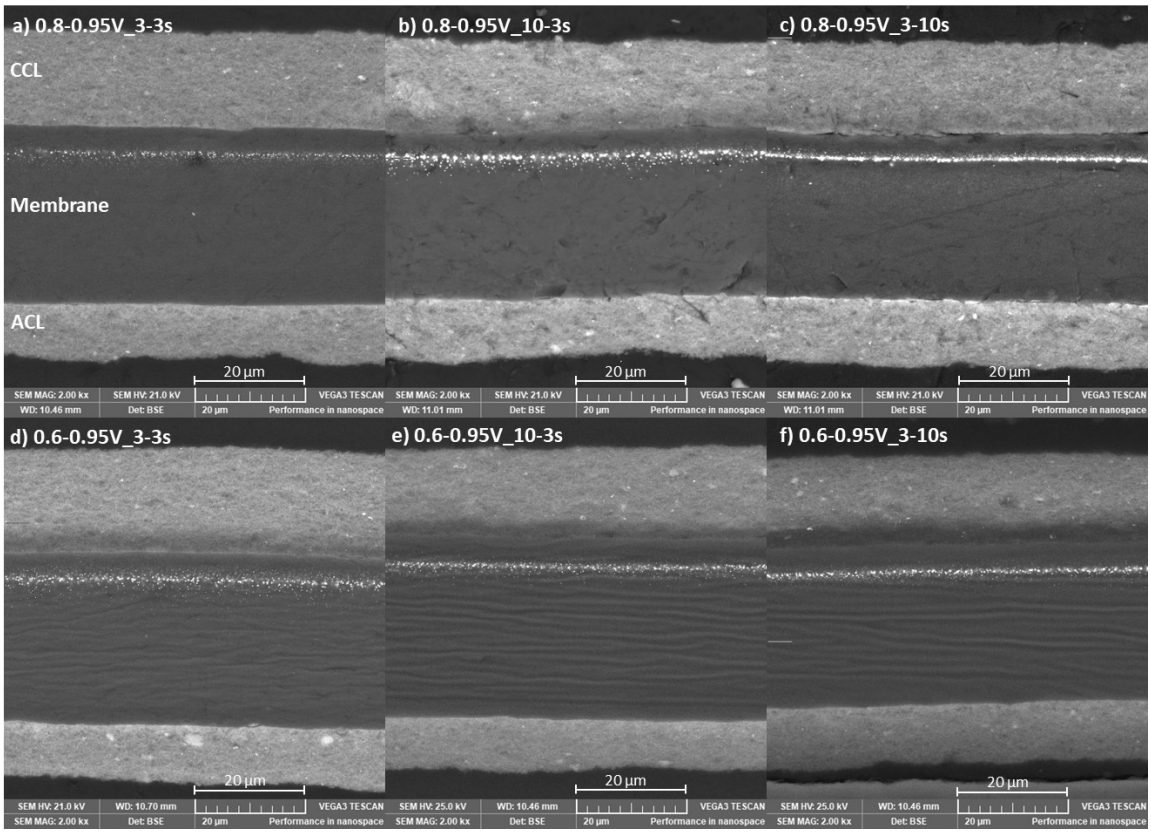

Figure 4.10. Post-mortem SEM cross-sectional images (at 2,000x magnification) of the six MEAs degraded by AST: (a) 0.8-0.95V_3-3s, (b) 0.8-0.95V_10-3s, (c) 0.8-0.95V_3-10s, (d) 0.6-0.95V_3-3s, (e) 0.6-0.95V_10-3s, (f) 0.6-0.95V_3-10s

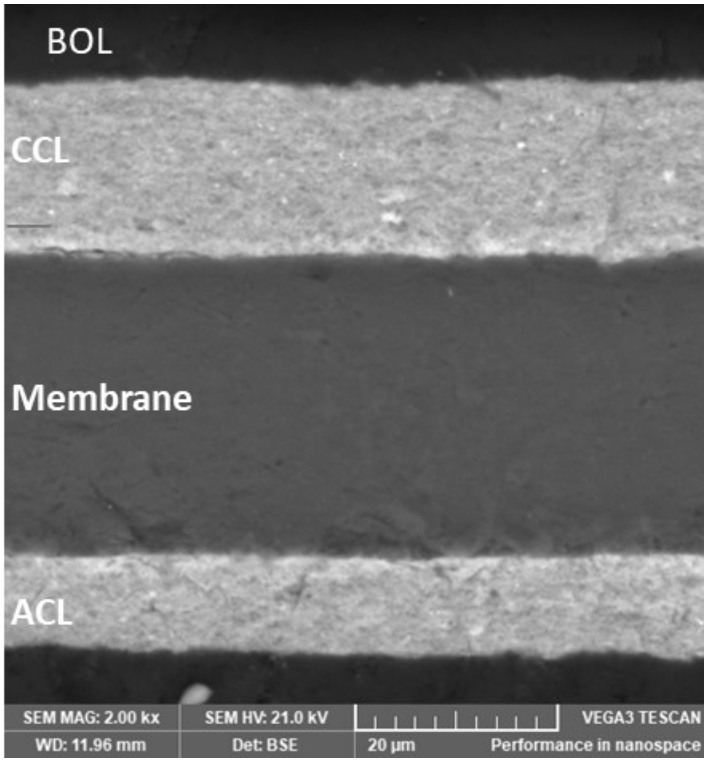

Figure 4.11. Reference SEM cross-sectional image (at 2,000x magnification) of the pristine MEA at BOL condition

Furthermore, the STEM-EDX analysis also confirms the presence of a platinum band, as well as Pt-depleted layer in the cathode catalyst layer adjacent to the membrane for all degraded samples, as depicted in Figure 4.12. In this figure, red signifies the presence of platinum, while green indicates the predominant fluorine element, characteristic of the ionomer/membrane phase. The top layer shows the catalyst layer while the green layer below is the membrane, which is a fluorine dominated region. The STEM-EDX map of the BOL sample, shown in Figure 4.13, reveals a predominantly red color in the cathode electrode, representing the pristine MEA with the highest Pt concentration next to the membrane area. While all six degraded samples show a decrease in red color compared to the BOL, indicating Pt loss in those areas, it is noteworthy that the Pt-depleted cathode area near the membrane exhibits the most pronounced green coloration, with minimal traces of red, for the most degraded sample aged by AST 0.6-0.95V_3-10s (grey circles/curve in Figure 4.6), suggesting the highest loss of Pt into the membrane due to the greatest Pt dissolution and Pt ion formation among the samples tested . Notably, the morphology of the catalyst layer remains intact in all

cases even at the harshest AST (0.6-0.95V_3-10s) (see Figure 4.12) within the Pt-depleted region, confirmed by the clearly distinguishable green ionomer structure.

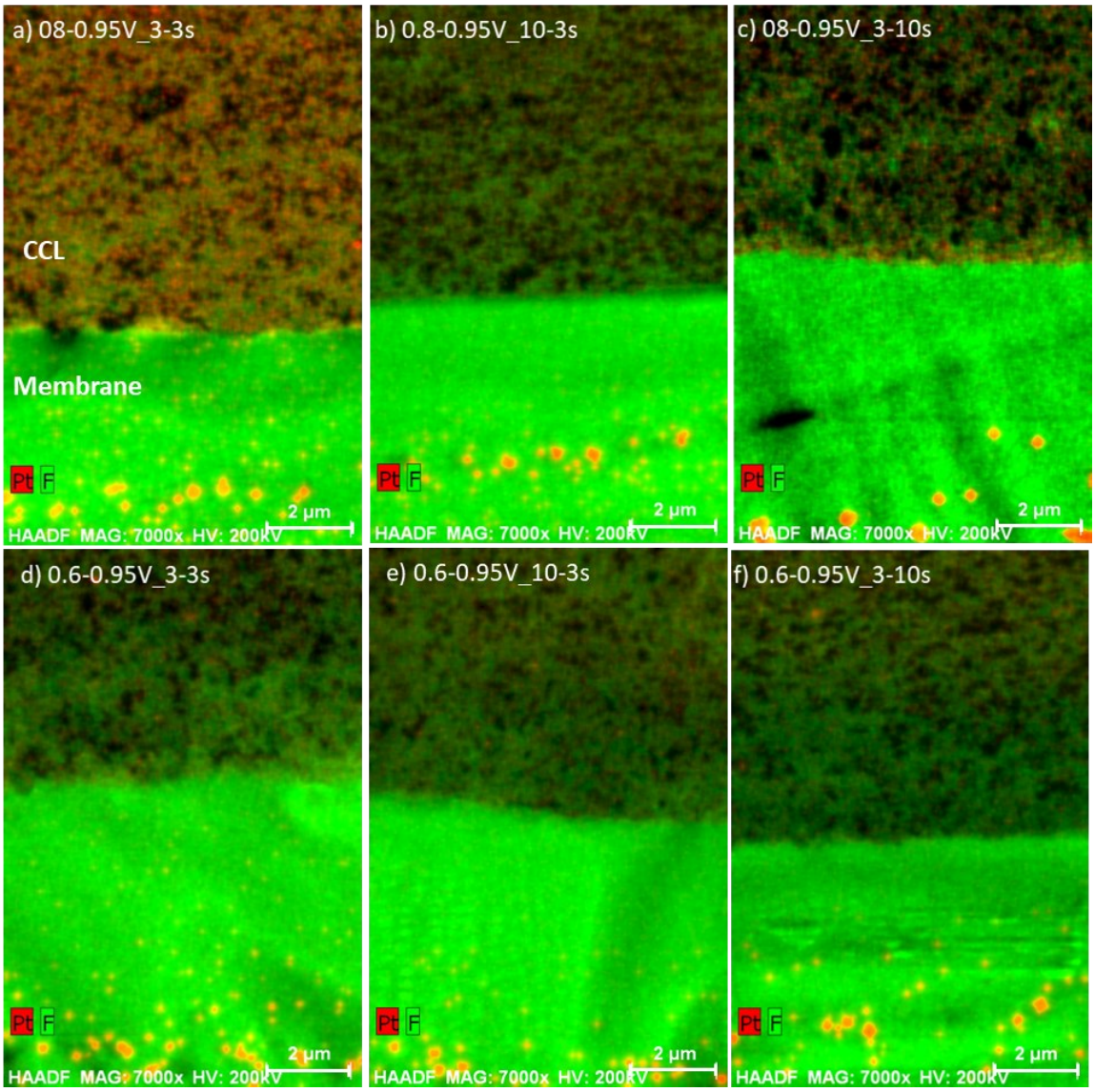

Figure 4.12. Post-mortem STEM-EDX cross-sectional images (at 7000x magnification) of the cathode-membrane interface from the six MEAs degraded by AST: (a) 0.8-0.95V_3-3s, (b) 0.8-0.95V_10-3s, (c) 0.8-0.95V_3-10s, (d) 0.6-0.95V_3-3s, (e) 0.6-0.95V_10-3s, (f) 0.6-0.95V_3-10s

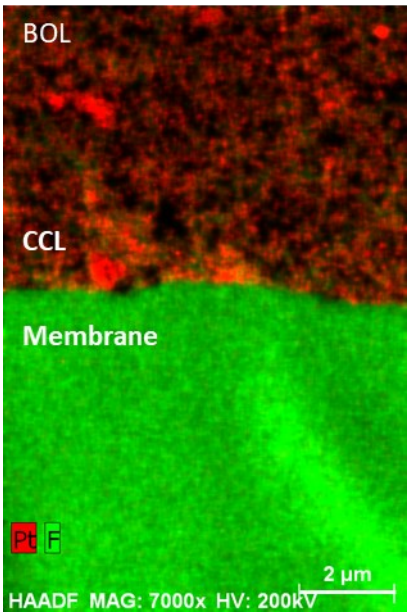

Figure 4.13. Reference STEM-EDX cross-sectional image (at 7000x magnification) of the cathode-membrane interface from a pristine MEA at BOL condition

4.2.2. Effect of Lower Potential Limit on Pt degradation

To gain insights into the specific effect of LPL on degradation rate, the six voltage cycling ASTs were divided into three pairs for systematic comparisons. Each pair was characterized by uniform conditions, with the sole variable being the LPL. Figure 4.14a-c illustrates the normalized ECSA over the number of cycles for these three pairs of experiments. As shown in Figure 4.14a, in the case of symmetric voltage cycling with a 6-second cycle length (LPL dwell time = UPL dwell time = 3 seconds), the AST conducted at LPL=0.6 V (blue circles/curve) exhibited almost double the ECSA loss compared to its counterpart at LPL=0.8 V (orange circles/curve), consistent with observations documented in the literature (65). This trend persisted across two additional pairs of experiments involving asymmetric ASTs with a 13-second cycle duration (LPL dwell time = 10 seconds, UPL dwell time = 3 seconds in Figure 4.14b; and LPL dwell time = 3 seconds, UPL dwell time = 10 seconds in Figure 4.14c), whereby under similar circumstances the AST cycle with the lower LPL caused more degradation. Indeed, despite the more severe conditions of the ASTs with LPL=0.8 V, specifically 0.8-0.95V_3-10s (purple circles/curve), characterized by extended dwell time at high potentials, it demonstrated ECSA loss comparable to that of the least degrading AST at LPL=0.6 V (0.6-0.95V_3-3s, blue circles/curve). Similarly, AST 0.8-0.95V_10-3s (green circles/curve), featuring a longer

cycle duration, maintained significantly higher ECSA at the end of the test, with a normalized ECSA of ca. 47% after 30,000 NoC compared to AST 0.6-0.95V_3-3s (blue circles/curve), which showed around 34% at 30,000 NoC. This emphasizes the consequential role of LPL compared to other stressors, such as cycle duration and exposure time to high potentials, in influencing the degradation dynamics observed in these stress tests.

For a deeper comprehension of the degradation mechanism and understating the effect of voltage cycling AST parameters on ECSA loss, the Pt oxide fractional coverage and Pt ion concentration over time were obtained from the model for the ASTs conducted in this study shown in Figure 4.14d-f and Figure 4.14g-i, respectively. Similar to the normalized ECSA plots, these plots are also organized into three separate pairs for clarity and facilitating easier comparison.

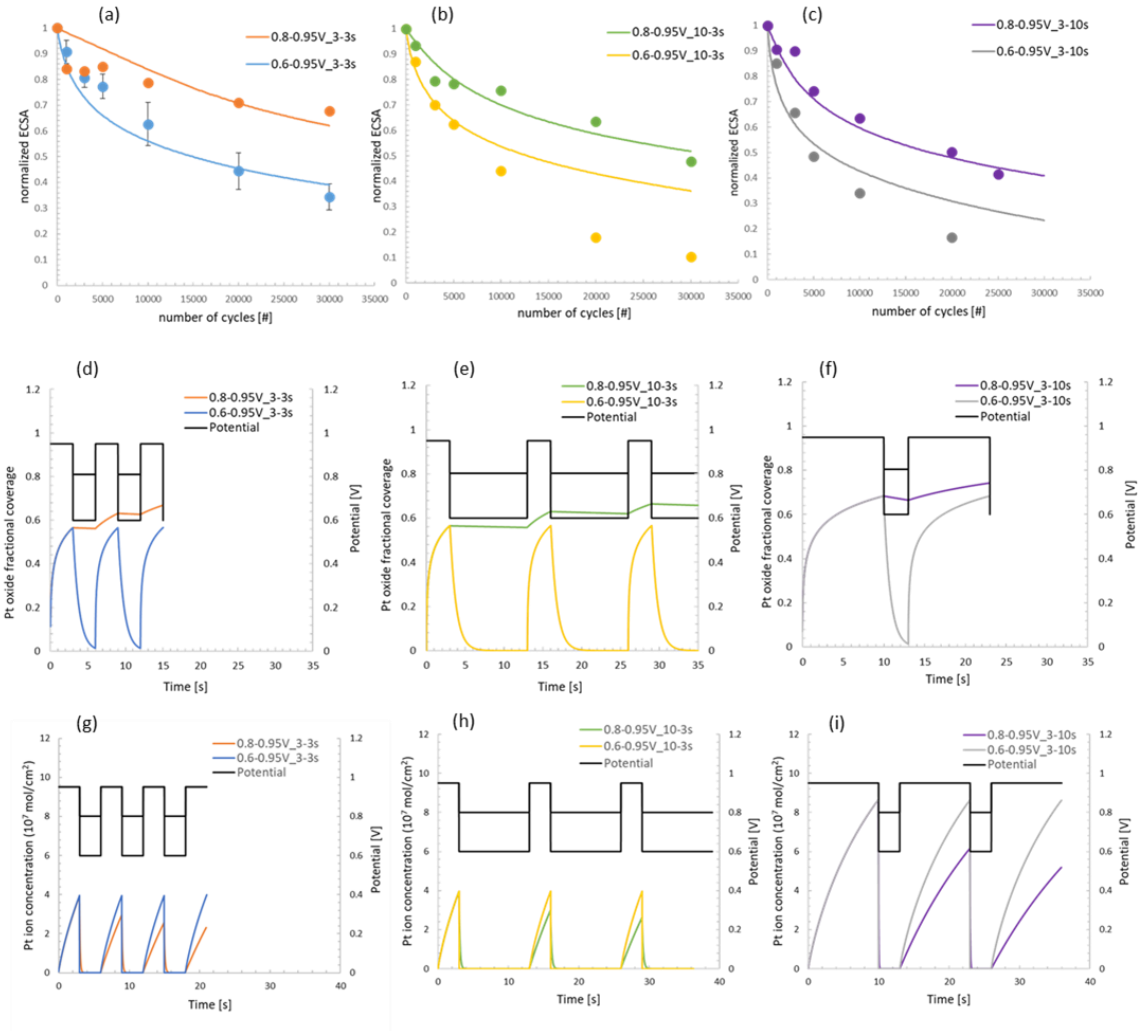

Figure 4.14. Measured and simulated normalized cathode ECSA (i.e., ECSA/ECSA$_{BoL}$) versus the number of AST cycles (a-c), simulated Pt oxide fractional coverage (d-f), and simulated Pt ion concentration (g-i) for pairs of ASTs: 0.8-0.95V_3-3s and 0.6-0.95V_3-3s, 0.8-0.95V_10-3s and 0.6-0.95V_10-3s, and 0.8-0.95V_3-10s and 0.6-0.95V_3-10s from left to right. a-c) The circles show the measured experimental data, and the solid line is the simulated results.

Figure 4.14d-f demonstrates the platinum surface oxide fraction over time during voltage cycling AST with varying dwell times. According to the Figure 4.14d-f, the rate of Pt oxide removal at LPL is notably slower at the LPL of 0.8 V compared to 0.6 V across all three cases. Consequently, at the end of an equivalent duration at the LPL, a larger portion of the Pt surface remains covered at LPL=0.8V, potentially leading to the accumulation of Pt oxide over subsequent cycles. For example, when comparing ASTs 0.6-0.95V_3-3s and 0.8-0.95V_3-3s (blue and orange curves in Figure 4.14d), after

spending 3 seconds at LPL, more than 50% of the Pt catalyst is still covered with an oxide layer at LPL of 0.8V, while the oxide coverage fraction for LPL of 0.6V is close to zero. This higher oxide coverage of the Pt at LPL=0.8 V protects the Pt from dissolution during the subsequent UPL dwell time in the next cycle, leading to less Pt dissolution and therefore lower Pt ion concentration compared to its previous cycle. The corresponding Pt ion concentration over time can be seen in Figure 4.14g-i. As the number of voltage cycles increases, the concentration of Pt ions consistently decreases due to the accumulation of Pt oxide for all three ASTs at LPL=0.8 V. However, in the case of LPL=0.6V, after 3 seconds almost all the formed Pt oxide layer will be removed during LPL, and initial bare Pt surface will be again exposed to dissolution. Thus, the Pt ion concentration stays at the same level at UPL as the number of cycles increases throughout the aging process. In the following paragraphs, the results of post-mortem analyses, with a particular focus on the effect of LPL on ECSA loss, will be discussed.

The particle size distribution (PSD) of fresh and aged samples is depicted in Figure 4.15. The particle size distribution of aged samples from experiments conducted with an LPL of 0.8 V are only slightly wider than at BOL, showing less than 1 nm increase in the mean particle size compared to the BOL samples (see Table 4.3). Conversely, samples subjected to cycling from 0.6 V exhibit a significantly broader distribution that also shifts towards larger particle sizes by approximately 2-4 nm (see Table 4.3). This increase in the average size of the Pt nanoparticles accompanied by a noticeable widening of the size distribution is indicative of the dominant Ostwald ripening mechanism (86). As explained earlier, this mechanism involves the dissolution of the smallest nanoparticles due to their higher surface energy, followed by the re-deposition of the resulting Pt ions onto larger nanoparticles to establish equilibrium within the system. Consequently, smaller Pt nanoparticles decrease in size, while larger ones grow, leading to a broader distribution of particle sizes until the smaller nanoparticles are completely dissolved (88).

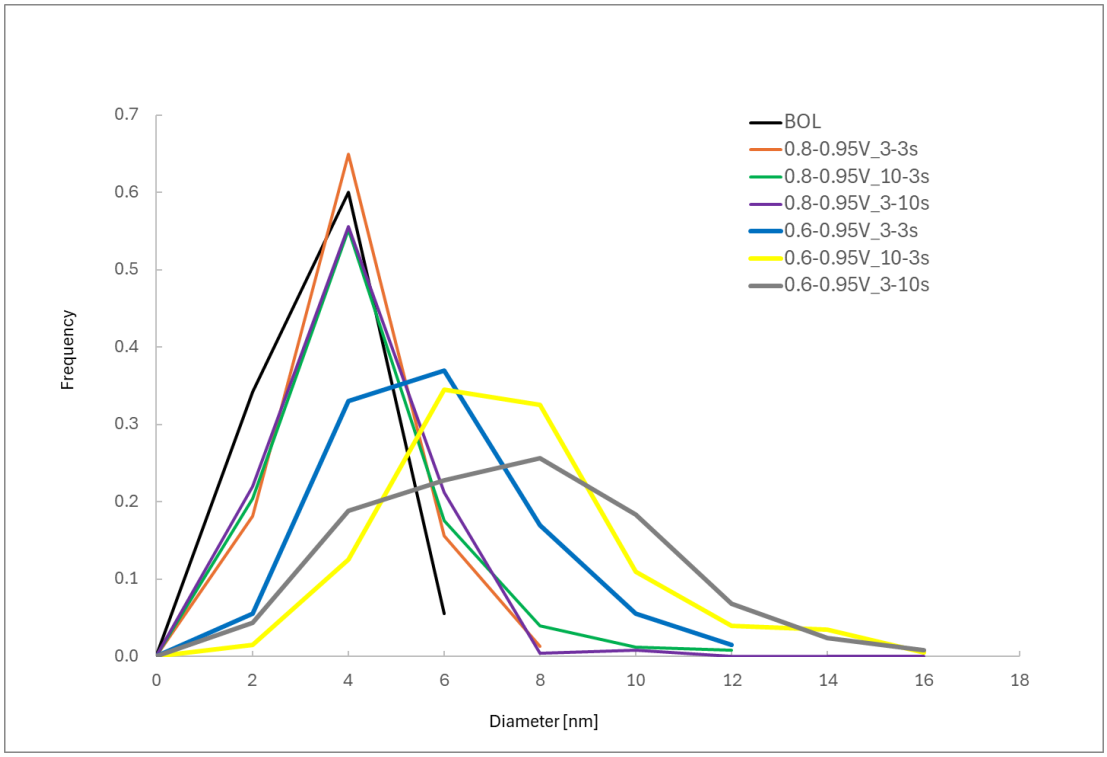

Figure 4.15. PSD for BOL and EOT with two different LPLs

The dark Pt-depleted area in the cathode along the membrane interface is more pronounced in the SEM images (Figure 4.10) for the ASTs performed at LPL=0.6 V. This Pt-depleted region can also be recognized in the STEM-EDX maps, which show the cathode-membrane interface in higher resolution compared to SEM images. Specifically, each image in the bottom row of Figure 4.12, corresponding to an AST with an LPL of 0.6 V, shows less Pt content in the cathode catalyst layer compared to the image at the top, associated with the same AST cycles but at LPL of 0.8 V. These observations also suggests a higher rate of Pt dissolution and therefore permanent Pt loss into the membrane in the samples degraded through AST with an LPL of 0.6 V for each pair, which aligns with the higher Pt ion concentrations observed for ASTs with lower LPL value, as predicted by the model presented in Figure 4.14g-i.

In summary, the higher ECSA loss observed at EOT for MEAs degraded by ASTs with an LPL of 0.6 V, compared to those with an LPL of 0.8 V, is attributed to the faster rate of oxide removal at lower LPLs, leading to faster Pt dissolution and higher concentration of Pt ions during the subsequent UPL hold. Post-mortem analyses confirmed this hypothesis by revealing larger Pt particle size growth due to increased rates of Pt dissolution/deposition at an LPL of 0.6 V. Additionally, observations of a darker and

less red cathode area at the membrane interface in SEM and STEM-EDX mapping, respectively, indicate more material loss into the membrane due to the higher Pt ion concentration at lower LPLs.

4.2.3. Effect of Dwell Time at Upper Potential Limit on Pt Degradation

With these six ASTs, the effect of dwell time at high potentials can be investigated at two different LPL levels of 0.6 V and 0.8 V. Considering LPL=0.6 V first, the AST 0.6-0.95V_3-3s (blue circles/curve in Figure 4.6) and AST 0.6-0.95V_3-10s (grey circles/curve in Figure 4.6) share all the parameters except for the UPL dwell time, which is varied from 3 seconds to 10 seconds. This allows to isolate the effect of UPL dwell time while all other parameters are fixed within a given cycle. As shown in Figure 4.6, the voltage cycling AST with 10 seconds at UPL (grey circles/curve in Figure 4.6) caused more than 80% ECSA loss after 20,000 cycles and reached the failure criterion, which was considered 10% of the voltage loss at 0.6 A/cm^2.in this study. On the other hand, the AST with 3 seconds UPL dwell time (blue circles/curve in Figure 4.6) showed less than 60% ECSA loss after 30,000 cycles.

Likewise, the other pair of experiments with the same parameters but LPL of 0.8 V illustrated the same trend, by which the AST with more dwell time at UPL (purple circles/curve in Figure 4.6) showed more ECSA loss. AST 0.8-0.95V_3-10s (purple circles/curve in Figure 4.6) lost more the 50% of its ECSA and more than 10% voltage loss after 25,000 cycles. While its counterpart with lower UPL dwell time (AST 0.8-0.95V_3-3s, orange circles/curve in Figure 4.6) maintained more than 70% of the initial ECSA. Other studies (59,60,67) have observed an increased degradation of ECSA in ASTs characterized by longer UPL dwell time. However, their conclusions were drawn from comparisons of ASTs where both LPL dwell time and UPL dwell time changed between experimental runs, making it complicated to isolate the individual effects of these two factors.

While Kneer et al. attributed the observation of higher ECSA degradation at long UPL dwell times to the formation of subsurface oxides due to enhanced place exchange mechanism in the presence of oxygen, the model proposed by Shojayian and Kjeang (48) suggests that anodic dissolution of the Pt during UPL is mainly responsible for this phenomenon. Indeed, as indicated by the outcomes of the model for Pt ion concentration

depicted in Figure 4.14g-i, the ASTs with a UPL dwell time of 10 seconds at both LPL levels (the grey curve at LPL=0.6 V and the purple curve at LPL=0.8 V in Figure 4.14i) consistently exhibit elevated Pt ion concentrations throughout the aging process when compared to ASTs with a UPL dwell time of 3 seconds (the blue curve at LPL=0.6 V and the orange curve at LPL=0.8 V in Figure 4.14g) under the same LPL. It is important to highlight that in the case of LPL=0.8 V, even though both ASTs (0.8-0.95V_3-3s and 0.8-0.95V_3-10s) experienced reduced Pt ion concentration over time due to oxide accumulation, the AST with a longer UPL dwell time (purple curve) maintained higher Pt ion concentrations overall during the aging process. The higher rate of Pt dissolution and subsequent deposition for ASTs with longer dwell times at UPLs was also demonstrated through particle size measurements, which revealed larger particle sizes compared to ASTs with shorter UPL dwell times for both LPL levels (see Table 4.3). Notably, the largest Pt particle measured, sized at 17.1 nm, was observed under the conditions of an LPL of 0.6 V with a 10-second dwell time at the UPL.

Additionally, the elevated rate of Pt dissolution caused by long dwell times at UPL results in higher rate of material loss into membrane. This conclusion is supported by the SEM image of the MEA cross-section degraded by AST 0.6-0.95V_3-10s, which reveals a conspicuous dark band in the catalyst layer along the membrane, indicating the greatest Pt loss in that region among all the ASTs. We believe that this high degree of material loss occurred during this AST is the reason for the slightly higher values of ECSA loss after 5,000 cycles compared to the model prediction, considering that the model has not accounted for 1D migration of the Pt ions into the membrane, as mentioned previously.

Furthermore, the SEM images indicate a darker Pt-depleted region along the membrane for ASTs 0.8-0.95V_3-10s and 0.6-0.95V_3-10s compared to their counterparts with a shorter dwell time ASTs 0.8-0.95V_3-3s and 0.6-0.95V_3-3s, respectively, suggesting a higher rate of Pt ion migration to the membrane for the ASTs with longer UPL dwell time. This phenomenon is further evident for LPL of 0.8 V by observations in the STEM-EDX maps, where AST 0.8-0.95V_3-10s exhibits fewer traces of red color (representing Pt elements) remaining in the cathode near the membrane compared to AST 0.8-0.95V_3-3s.

Overall, our investigation revealed that prolonged exposure to high potentials correlates with a more substantial loss in ECSA at both LPL levels, i.e., 0.6 and 0.8 V.

This loss primarily stems from anodic dissolution, consequently elevating the concentration of Pt ions. The heightened availability of Pt ions facilitates their redeposition onto smaller Pt particles during cathodic scan (decreasing potentials), thereby accelerating the phenomenon of Ostwald ripening, which was supported by the presence of larger Pt particles in ASTs with extended UPL dwell times, as opposed to their counterparts subjected to shorter exposure periods. Additionally, ASTs characterized by prolonged UPL dwell times exhibited an increased migration rate of dissolved Pt ions towards the membrane. This was shown by the observation of a darker Pt-depleted region along the membrane and a diminished red coloration evident in STEM-EDX maps.

4.2.4. Effect of Dwell Time at Lower Potential Limit on Pt Degradation

The impact of LPL dwell time on ECSA loss is also valuable to study as it can offer insight into the Pt degradation mechanism of the cathode catalyst layer. With the experimental design in this study, the explicit effect of LPL dwell time can be analyzed at two distinct voltage levels of 0.8 V and 0.6 V. Initially focusing on an LPL of 0.8 V, both AST 0.8-0.95V_3-3s and AST 0.8-0.95V_10-3s have identical parameters except for the LPL dwell time. Comparing the ECSA loss of the degraded cells after running 30,000 AST cycles in Figure 4.6 shows ca. 10% more ECSA loss for the MEA degraded by AST with higher dwell time at LPL even though the MEAs spent identical time at higher potentials. According to the model, this can be explained by the slow rate of Pt oxide removal at LPL of 0.8 V. In AST 0.8-0.95V_10-3s, the 10-second dwell time at LPL allows for more Pt oxide to be stripped off the Pt surface compared to only 3 seconds. Therefore, the lower amount of protective Pt oxide layer in AST 0.8-0.95V_10-3s exposes more amount of bare Pt to dissolution, leading to a higher Pt ion concentration (Figure 4.14h). The increased average size of Pt particles (see Table 4.3) for the AST with a higher LPL dwell time, AST 0.8-0.95V_10-3s, and the presence of a more distinctly Pt-depleted cathode region near the membrane compared to AST 0.8-0.95V_3-3s (Figure 4.12b and Figure 4.12a) also suggests that there is a greater likelihood of Pt particle dissolution and migration, contributing to the observed higher rate of ECSA degradation.

The effect of dwell time at LPL when LPL is equal to 0.6 V can also be investigated. To this end, the comparison of normalized ECSA between AST 0.6-0.95V_3-3s and AST 0.6-0.95V_10-3s is undertaken, noting their common parameters except for their variance in LPL dwell time. It is expected based on the model that the ECSA degradation over time

to be comparable for both ASTs (blue and yellow solid lines in Figure 4.6). However, the results of normalized ECSA from experimental results for AST 0.6-0.95V_10-3s deviates from the model prediction after 5000 cycles and demonstrate higher ECSA loss compared to what the model had anticipated, resulting in more ECSA degradation than AST 0.6-0.95V_3-3s which spends only 3 seconds at LPL=0.6 V (see blue circles/curve and yellow circles in Figure 4.6).

We believe the discrepancy observed between experimental ECSA results and the model for AST 0.6-0.95V_10-3s is due to its prolonged dwell time at lower potentials, i.e. 0.6 V. At low potentials, such as 0.6 V, which is associated with higher current densities as shown by the polarization curve in Figure 2.7, the electrochemical reactions in a PEM fuel cell including oxygen reduction reaction (Equation 1.2) proceed more rapidly to meet the increased demand for electrons. As a result, a greater amount of water is produced as a byproduct of the fuel cell operation. We hypothesize that this elevated water production plays a pivotal role in facilitating the mobility of Pt ions within the ionomer phase, providing Pt ions increased freedom to travel greater interparticle distances for re-deposition, which is not considered in the model. Therefore, dissolved Pt ions have a greater opportunity to reach larger Pt particles at grater distances for re-deposition, increasing the rate of Ostwald ripening.

This noticeable increase in ECSA degradation observed in experimental findings for AST 0.6-0.95V_10-3s due to enhanced Ostwald ripening is also supported by particle size measurements. Specifically, the average Pt particle size after 30,000 cycles for AST 0.6-0.95V_10-3s is recorded at 6.3 nm, whereas for AST 0.6-0.95V_3-3s, it measures 4.8 nm. This suggests a higher growth rate from Ostwald ripening mechanism for AST 0.6-0.95V_10-3s despite their comparable Pt ion concentration (yellow and blue curves in Figure 4.14h and Figure 4.14g, respectively). The comparable Pt ion concentration implies that the larger catalyst Pt particles observed in AST 0.6-0.95V_10-3s cannot be attributed to a higher rate of anodic dissolution. Instead, the above mentioned hypothesis of enhanced Ostwald ripening due to improved ion mobility, can justify the presence of larger Pt particles in AST 0.6-0.95V_10-3s compared to AST 0.6-0.95V_3-3s because it is a plausible explanation that under the same ion concentration, facilitated ion mobility will increase the likelihood of re-deposition of dissolved Pt ions, thereby promoting the growth of Pt particles.

Furthermore, this higher ion mobility in the AST 0.6-0.95V_10-3s can also increase the rate of Pt loss into the membrane, which is confirmed by the dark Pt-depleted region along the membrane interface. This Pt-depleted band is more pronounced for the AST 0.6-0.95V_10-3s than the AST 0.6-0.95V_3-3s despite their same Pt ion concentration (see Figure 4.10), which confirms that the migration rate of Pt ion species for AST 0.6-0.95V_10-3s must be higher so that with the same Pt ion concentration as AST 0.6-0.95V_3-3s, more Pt is lost into the membrane. Another observation that supports the greater migration rate of Pt ion species toward the membrane under ASTs with long dwell time at low LPL levels, i.e., 0.6 V, is the observed heterogeneous particle growth within the CL in AST 0.6-0.95V_10-3s. The particle size data in Table 4.3 reveals that the difference between the mean size of Pt particles located at the cathode-membrane interface and that of those located at cathode-GDL interface for AST 0.6-0.95V_10-3s is the highest among the three ASTs conducted at LPL of 0.6 V. In other words, the migration process of ionic species towards the cathode-membrane interface was enhanced due to facilitated Pt ion mobility in AST 0.6-0.95V_10-3s, making it easier for Pt ions to travel further distances within the CL and re-deposit at locations within the CL that are closer to membrane. This will result in the larger Pt particles at the cathode-membrane interface compared to the other side of CL (near GDL).

In summary, the higher rate of ECSA loss, as indicated by particle size data and SEM/STEM-EDX images, for ASTs with longer LPL dwell times at LPL = 0.8 V can be attributed to the higher ion concentration resulting from a slow oxide removal rate. However, for LPL = 0.6 V, the Pt ion concentration remains the same for ASTs with long and short LPL dwell times, as the oxide removal is very fast at LPL of 0.6 V according to the model. Therefore, there should be another mechanism, not captured in the model, to explain the greater rate of ECSA loss observed through both in-situ electrochemical diagnostics and post-mortem analyses for the AST with longer dwell time at 0.6 V compared to its counterpart with shorter LPL dwell time. The hypothesis in this study suggests that facilitated Pt ion mobility, due to excess water production during prolonged exposure to low potentials of 0.6 V, could contribute to the enhanced Ostwald ripening and the movement of Pt ions towards the membrane.

4.3. Performance Degradation

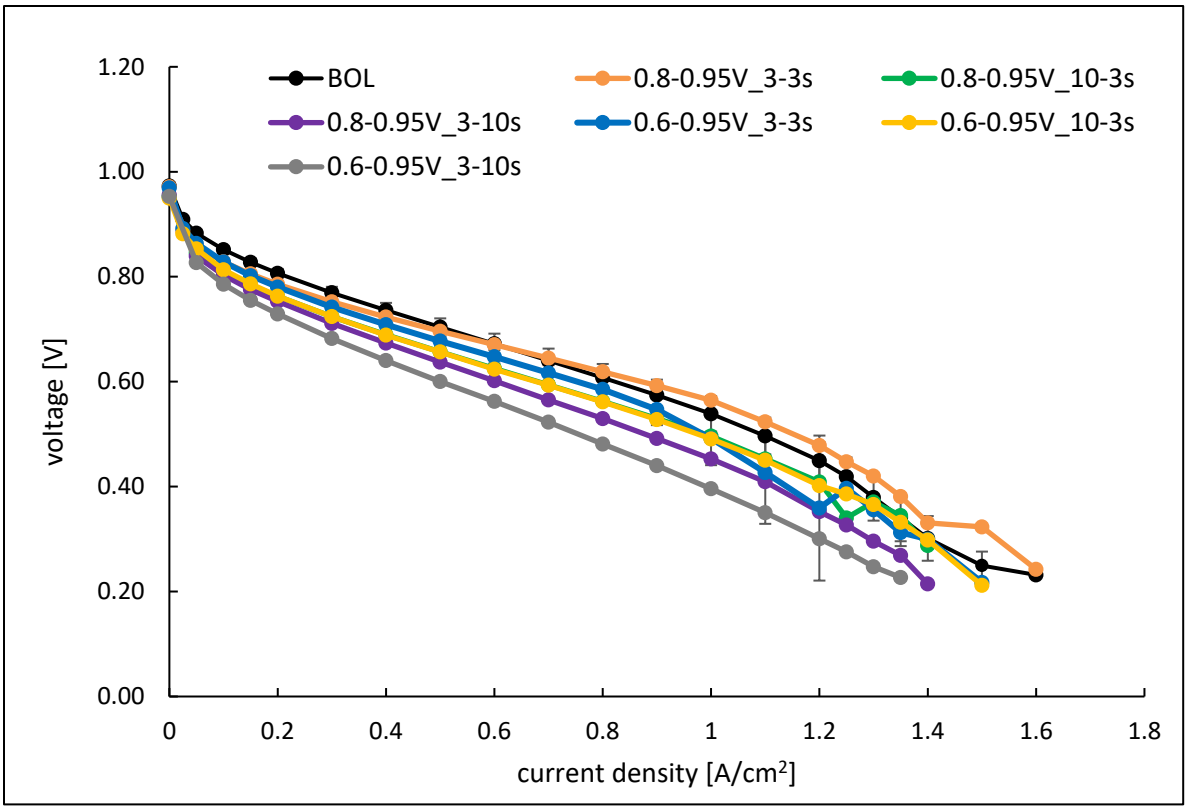

Figure 4.16 Polarization curves at BOL condition and after 20,000 voltage cycles. The BOL condition represents the average performance of all eight tested cells, and the baseline includes the average performance of three cells; the error bars of the baseline AST 0.6-0.95V_3-3s represent the standard deviation from three measurements.

Figure 4.16 displays the average polarization curve of all eight cells at BOL condition alongside the polarization curves of the cells after 20,000 voltage cycles. As previously noted in Section 4.1.1, beyond 0.6 A/cm², the mass transport region is reached, wherein even minor temperature fluctuations lead to a significant performance decline. Therefore, for comparison purposes, voltages below 0.6 A/cm² are considered, as they are less susceptible to testing conditions and thus more accurately reflect the performance degradation caused by ASTs. As expected, the BOL condition (black curve) exhibits the highest performance before 0.6 A/cm², surpassing that of all degraded cells.

Comparing polarization curve of cells degraded through ASTs an LPL of 0.8 V reveals a performance order consistent with their ECSA ranking in Figure 4.6. In other words, the harsher AST that induced greater ECSA loss also resulted in more pronounced

performance (voltage) losses compared to BOL. Consequently, the mildest AST at LPL of 0.8 V, 0.8-0.95V_3-3s (orange curve), which is characterized by a short LPL dwell time and short UPL dwell time, resulted in the lowest voltage loss. Conversely, the most severe test at an LPL of 0.8 V, AST 0.8-0.95V_3-10s (purple curve), caused the greatest voltage loss, while the AST denoted as 0.8-0.95V_10-3s (green curve), yielding a polarization curve between the two extremes. This is also the case for the three ASTs conducted at an LPL of 0.6 V. However, the superior performance of the cells subjected to AST 0.6-0.96V_3-3s (blue curve) in Figure 4.16, despite being more severely degraded, compared to cells degraded through AST 0.8-0.95V_10-3s and AST 0.8-0.95V_3-10s (green and purple curves, respectively), which exhibit less ECSA loss (see Figure 4.6), suggests that performance loss may not always correlate directly with ECSA loss.

This observation could be attributed to the higher specific activity of larger Pt particles. Specific activity refers to the catalytic activity per unit surface area of Pt (A/cm^2), indicating how efficiently the Pt surface catalyzes the reaction. As shown in Table 4.3, the Pt particles in MEAs degraded by AST 0.8-0.95V_10-3s (green curve) and AST 0.8-0.95V_3-10s (purple curve) experienced less particle growth compared to those in AST 0.6-0.95V_3-3s (blue curve), which had significantly larger Pt particles due to the Ostwald ripening mechanism, leading to a high rate of ECSA degradation (see Figure 4.6). The higher specific activity of larger Pt particles in MEAs exposed to AST 0.6-0.95V_3-3s (blue curve) partially offset its higher ECSA loss, resulting in lower voltage loss.

The reason for decreasing specific activity with decreasing particle size is that smaller particles have a higher ratio of less active edge and corner sites in comparison to their larger counterparts, leading to lower specific ORR activity. Furthermore, it is suggested that smaller particles have enhanced potential dependent adsorption of oxygenated species. The rise in oxophilicity in smaller particles results in a reduced specific activity during the ORR. This occurs because oxygenated species generated as intermediates during the ORR, such as OH, tend to adsorb onto the active sites crucial for O_2 adsorption, thereby hindering the ORR process (59,89–92).

Overall, determining which type of AST causes the most rapid performance degradation is challenging due to the complex interplay of various factors contributing to voltage loss. However, it is clear from the data that the ASTs with long exposure to high potentials, 0.6-0.95v_3-10s (grey curve) and 0.8-0.95V_3-10s (purple curve), results in

the highest voltage loss regardless of the LPL. This phenomenon may stem from a substantial portion of ECSA loss occurring during the ASTs with extended UPL dwell time due to material loss into the membrane. Such ECSA loss, originating from material loss rather than particle size growth, does not contribute to specific activity, and thus have a direct impact on performance degradation. It is worth noting that the LPL was found to be the most influential factor in determining ECSA loss. However, as mentioned above, depending on the source of ECSA loss—whether it is primarily from particle growth or to what extent material loss contributes to it—the effect of ECSA loss on voltage loss might be compensated. Therefore, UPL dwell time may play a more significant role in determining performance loss compared to LPL.

4.4. Membrane Degradation and Carbon Corrosion

This section will assess the degradation of the membrane and carbon support to ensure that the ASTs had minimal effect on them throughout the aging process, primarily targeting Pt catalyst degradation. For this purpose, the changes in cathode double-layer capacitance (C_{dl}), hydrogen crossover current density (i_x) and cell resistance(R_1) for all eight degraded cells were monitored. Ideally, under minimal carbon support degradation and membrane degradation (e.g. membrane thinning) these variables are expected to remain constant throughout the course of experiment (93,94). The results depicted in Figure 4.17 demonstrate that both the cathode double-layer capacitance and hydrogen crossover current density remain relatively stable throughout the load cycle degradation tests, indicating minimal degradation in both the membrane and carbon supports. Similarly, the cell resistance shown in Figure 4.18 maintains an overall constancy, suggesting no significant alteration in the ionic or electrical conductivity of the fuel cell components and their interfaces. In the analysis of thickness measurements, no significant reduction in cathode layer thickness was observed for the samples, and the error bars corresponding to the thickness of layers for all degraded MEAs overlap with BOL values as illustrated in Figure 4.19, indicating that carbon corrosion had a negligible effect on the degradation of the cathode. The heavy loss observed in ECSA for aged samples with a relatively constant trend in i_x, C_{dl}, R_1, and catalyst layer thickness over the course of ASTs aligns with the stress test's design, which aimed to induce controlled degradation primarily of the cathode Pt catalyst without causing major degradation in other fuel cell components, such as carbon support and membrane.

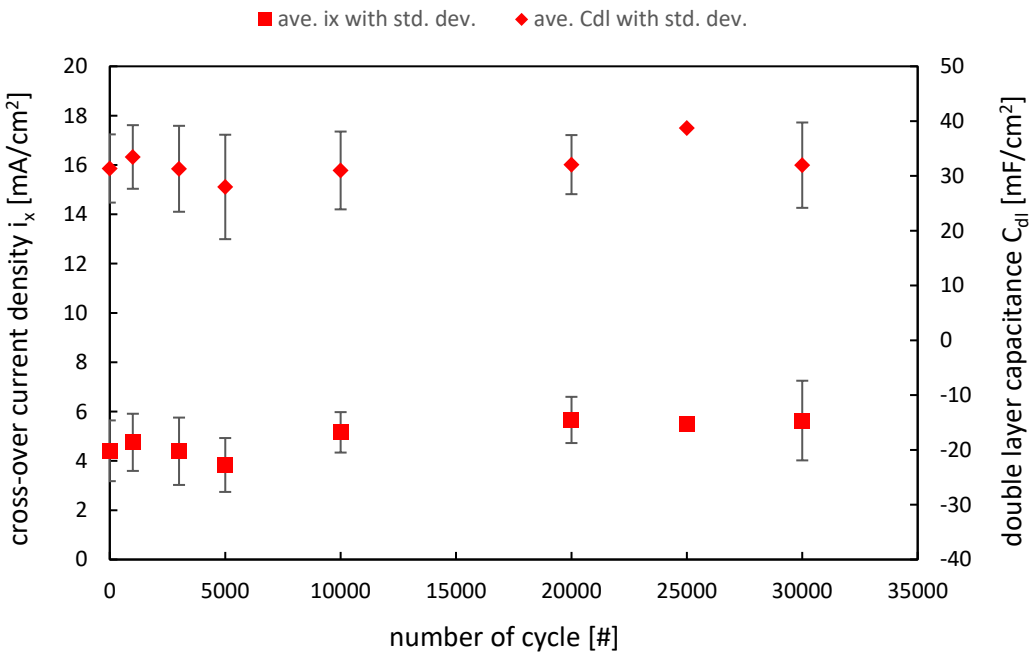

Figure 4.17. Average cathode double layer capacitance and hydrogen cross-over current density for aged cells at regular cycle intervals during the AST

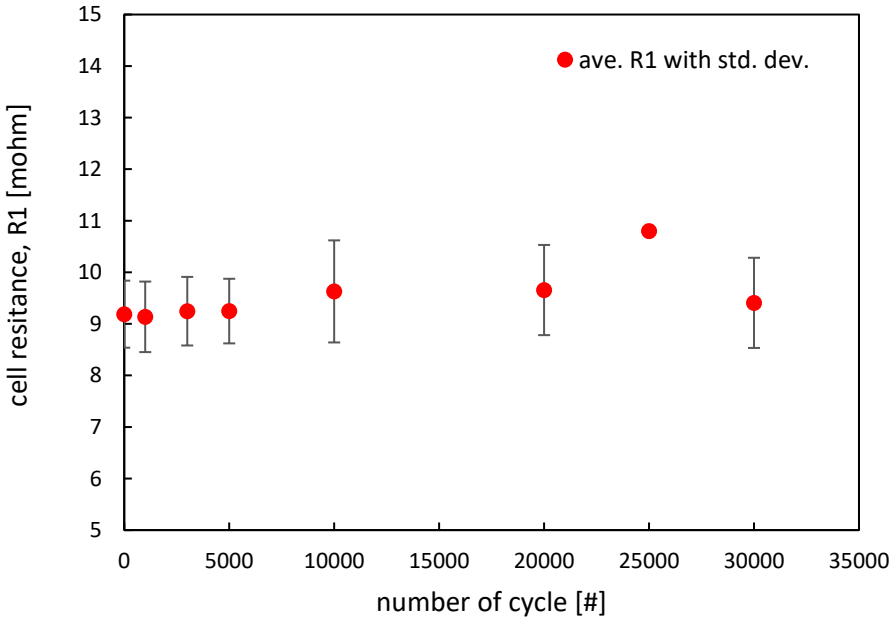

Figure 4.18. Average cell resistance for aged cells at regular cycle intervals during the AST

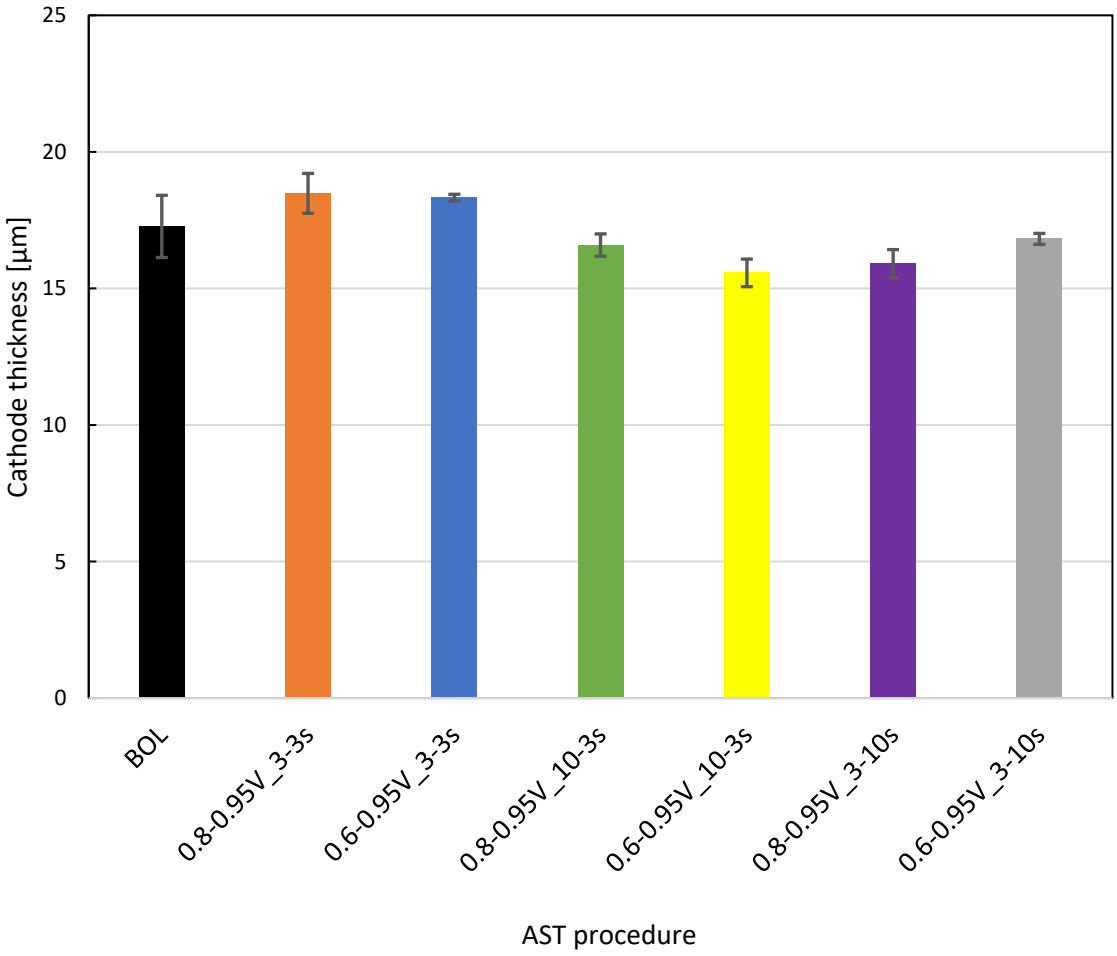

Figure 4.19. Cathode catalyst layer thickness extracted from SEM images for BOL and EOT; the error bars show the standard deviation of thickness measurements taken from three images, each captured at randomly selected locations on the same cross-sectioned MEA.

Chapter 5.

Conclusions

This thesis aimed to contribute towards enhancing the durability of PEMFCs, which represents a significant impediment to the widespread commercial adoption of fuel cell electric vehicles. The durability of fuel cells is often hindered by the degradation of their components. In this study, particular attention was given to the cathode electrode as it represents a critical component prone to degradation. The main objective was to systematically examine how varying cycle profiles in voltage cycling accelerated stress tests, specifically LPL and the dwell times of the cycles, affect the Pt ECSA degradation within the cathode catalyst layer. To achieve this, a novel set of eight accelerated stress test experiments was designed to complement existing literature findings and to provide deeper insights into the underlying mechanism of Pt loss during load cycle operation. The initial phase involved establishing degradation test protocols and testing capabilities, which included fuel cell fabrication using an ultrasonic spray coater and degradation and diagnostics protocol development employing fuel cell test equipment. This ensured the implementation of a consistent procedure throughout the study. Following that, procedures were developed for conducting post-mortem analyses using electron microscopy techniques. First, optimization was conducted for preparing MEA cross-sections by selecting suitable resin materials and adjusting grinder/polisher parameters to ensure high-quality SEM imaging. Subsequently, the protocol for preparing nanometer-sized MEA sections using ultramicrotomy was fine-tuned to facilitate optimal TEM imaging, particle size measurement, and elemental mapping by EDX.

The normalized ECSA to its initial value ($ECSA_{BOL}$) over the number of voltage cycles (NoC) during aging was showed that when UPL is set at OCV, the AST with LPL of 0.6 V exhibits greater degradation compared to the AST with LPL of 0.8 V, while holding other parameters constant across experiments. This trend holds true for both symmetric and asymmetric cases. The slower Pt oxide removal at LPL of 0.8 V, as per recently published theoretical models for Pt degradation, is attributed to the protection of bare Pt from dissolution at high potentials. Furthermore, the results indicated that at a fixed cycle number and fixed LPL dwell time, the AST with longer time at UPL induces more degradation at both LPL=0.6V and LPL=0.8V, likely due to higher Pt ion concentration

resulting from anodic dissolution of Pt during UPL. Regarding the effect of LPL dwell time, it was demonstrated that at a fixed cycle number and fixed UPL dwell time, the AST with longer LPL dwell time causes more degradation at both LPL=0.6V and LPL=0.8V. For an LPL of 0.8 V, this was attributed to the slow rate of oxide removal, while for LPL of 0.6 V, it was attributed to facilitated ion mobility.

Particle size measurements revealed larger mean catalyst Pt particles and a wider Pt particle size distribution in samples subjected to harsher AST, indicating Pt dissolution/redeposition as the dominant degradation mechanism. This hypothesis was supported by the non-uniform distribution of Pt within the catalyst layer, resulting in a Pt-depleted region in the cathode catalyst layer along the membrane, which was more pronounced in samples with higher ECSA loss. In this regard, the Pt-depleted region near the cathode-membrane interface was more prominent in samples with an LPL of 0.6 V compared to those with an LPL of 0.8 V. At each LPL level, the more degraded sample exhibited a more pronounced Pt-depleted region, with the order being the sample with a longer UPL dwell time followed by the sample with a longer LPL dwell time. In conclusion, the experimental data indicate that LPL emerged as the most influential factor in determining ECSA loss. It is important to note that in this study the UPL remained constant at OCV throughout the experiments, as mentioned earlier, in order to focus on exploring other parameters of the cycle profiles. However, according to the literature, high UPL value has been also reported as an important factor in Pt catalyst degradation (59,60). Thus, overall, to mitigate Pt degradation during fuel cell operation, it is recommended to avoid cycles with higher amplitude that cause voltage variations ranging from very low to very high potentials. This can be achieved by hybridizing the fuel cell stack with a battery (95), which serves as a buffer. The battery helps smooth out power demands and avoids cycles with high amplitude, particularly those involving low LPLs and high UPLs. This approach reduces the extreme voltage variations that can contribute to Pt degradation.

As mentioned above, after LPL, longer dwell times at UPL resulted in the most degradation, followed by longer dwell times at LPL. This suggests that platinum dissolution occurs not only during transient operations but also during dwell time at constant potentials. Although degradation from maintaining specific potentials is less significant compared to degradation caused by cycling through various potentials, this may be more pronounced for heavy-duty stacks. These stacks experience less frequent voltage changes due to road conditions, compared to light-duty vehicles, and therefore operate

for extended periods at potential limits, especially at the UPL, which highlights the importance of the degradation occurring at extended dwell times.

In addition to providing insight for real-world operation and fuel cell system design, the findings can be used for designing new ASTs that simulate the degradation occurring during real-world usage of automobiles. In this regard, for durability studies when UPL is set at OCV, it is recommended to employ AST cycles with lower LPLs and longer UPL dwell times. These conditions result in the most rapid Pt degradation, thereby reducing the overall testing time required.

Finally, the data on performance degradation revealed a general trend where higher ECSA losses, indicating harsher aging conditions, typically coincide with increased voltage losses. However, exceptions were observed, attributed to specific activity increases resulting from particle size growth. Therefore, further research is needed to better understand the correlation between Pt ECSA and performance losses in H_2/air systems, particularly for reliably predicting lifetime using voltage cycling ASTs.

5.1. Future Work

The existing approach to fuel cell fabrication could see enhancements through the adoption of advanced tools for synthesizing catalyst ink, such as ultrasonic stirring and/or homogenizer. Furthermore, employing direct film coating methods, such as doctor blade, instead of spray coating can offer benefits in uniformity, scalability, cost-effectiveness, and reduced waste (96,97). As a result, by improving fabrication process, it is possible to achieve a more uniform catalyst ink, thereby potentially enhancing fuel cell performance and reducing degradation rates. In this work, the ECSA was measured through hydrogen adsorption/desorption cyclic voltammetry as the primary metric to monitor Pt catalyst degradation. However, it has been reported that this method might lead to increasing errors in the quantification of the ECSA as the MEAs degrade more, and carbon monoxide stripping should be used for more accurate ECSA measurements of aged cathode electrodes (59,98,99). In addition to ECSA, additional diagnostics of the cathode catalyst layer that can measure other metrics such as mass/specific activity can also be adopted to provide more insight into the performance of the platinum cathode catalyst (59,67,69).

In order to gain a comprehensive understanding of the overall performance degradation during load cycling, it would be beneficial to investigate other factors contributing to performance loss. This could include measuring the proton conduction resistance of the cathode electrode and the oxygen transport resistance within the fuel cell system (59). Moreover, in the future, adopting a 1D model that accounts for spatial effects, such as platinum ion migration into the membrane and concentration gradients, may better fit the experimental results and offer a more comprehensive explanation of the mechanisms contributing to Pt degradation in these experiments.

Additionally, visualizing the distribution of liquid water within the cathode catalyst layer using X-ray computed tomography can offer valuable insights into the relationship between CCL degradation during load cycling and the distribution of liquid water across different LPL levels and combinations of dwell times (100). For post-mortem analyses, quantifying Pt loading and loss from the cathode layer can be achieved using STEM-EDX datasets. This approach enables more quantitative analysis of Pt loss to the membrane through migration from the cathode catalyst layer in various ASTs (83). Furthermore, Raman spectroscopy may be used in the future endeavours to investigate the carbon substrate and examine its degree of oxidation that could impact loss of catalytic activities (88).

References

1. Ripple WJ, Wolf C, Newsome TM, Galetti M, Alamgir M, Crist E, et al. World Scientists' Warning to Humanity: A Second Notice. BioScience. 2017 Dec 1;67(12):1026–8.

2. The Paris Agreement | UNFCCC [Internet]. [cited 2024 Mar 16]. Available from: https://unfccc.int/process-and-meetings/the-paris-agreement

3. The Greenhouse Effect and our Planet [Internet]. [cited 2024 Mar 16]. Available from: https://education.nationalgeographic.org/resource/greenhouse-effect-our-planet

4. US EPA O. Human Exposure and Health [Internet]. 2017 [cited 2024 Mar 16]. Available from: https://www.epa.gov/report-environment/human-exposure-and-health

5. Climate Change INFORMATION SHEETS.

6. US EPA O. Sources of Greenhouse Gas Emissions [Internet]. 2015 [cited 2024 Mar 16]. Available from: https://www.epa.gov/ghgemissions/sources-greenhouse-gas-emissions

7. Tellez-Cruz MM, Escorihuela J, Solorza-Feria O, Compañ V. Proton Exchange Membrane Fuel Cells (PEMFCs): Advances and Challenges. Polymers. 2021 Jan;13(18):3064.

8. Energy.gov [Internet]. [cited 2023 Nov 14]. Types of Fuel Cells. Available from: https://www.energy.gov/eere/fuelcells/types-fuel-cells

9. Energy.gov [Internet]. [cited 2023 Nov 14]. Comparison of Fuel Cell Technologies. Available from: https://www.energy.gov/eere/fuelcells/comparison-fuel-cell-technologies

10. O'Hayre RP, Cha SW, Colella WG, Prinz FB. Fuel cell fundamentals [Internet]. Third edition. Hoboken, New Jersey: John Wiley & Sons Inc; 2016. Available from: https://onlinelibrary.wiley.com/doi/book/10.1002/9781119191766

11. Trefilov AMI, Balan A, Stamatin I. Hybrid Proton-Exchange Membrane Based on Perfluorosulfonated Polymers and Resorcinol–Formaldehyde Hydrogel. Polymers. 2021 Nov 26;13(23):4123.

12. Ghassemzadeh L, Peckham TJ, Weissbach T, Luo X, Holdcroft S. Selective Formation of Hydrogen and Hydroxyl Radicals by Electron Beam Irradiation and Their Reactivity with Perfluorosulfonated Acid Ionomer. J Am Chem Soc. 2013 Oct 23;135(42):15923–32.

13. Huang X, Solasi R, Zou Y, Feshler M, Reifsnider K, Condit D, et al. Mechanical endurance of polymer electrolyte membrane and PEM fuel cell durability. J Polym Sci Part B Polym Phys. 2006;44(16):2346–57.

14. Shi S, Sun X, Lin Q, Chen J, Fu Y, Hong X, et al. Fatigue crack propagation behavior of fuel cell membranes after chemical degradation. Int J Hydrog Energy. 2020 Oct 16;45(51):27653–64.

15. Kusoglu A, Weber AZ. New Insights into Perfluorinated Sulfonic-Acid Ionomers. Chem Rev. 2017 Feb 8;117(3):987–1104.

16. Kim D, Jang Y, Choi E, Chae JE, Jang S. Reinforced Nafion Membrane with Ultrathin MWCNTs/Ceria Layers for Durable Proton-Exchange Membrane Fuel Cells. Membranes. 2022 Nov;12(11):1073.

17. Seo DC, Jeon I, Jeong ES, Jho JY. Mechanical Properties and Chemical Durability of Nafion/Sulfonated Graphene Oxide/Cerium Oxide Composite Membranes for Fuel-Cell Applications. Polymers. 2020 Jun;12(6):1375.

18. Mench MM. Fuel Cell Engines [Internet]. 1st ed. Wiley; 2008 [cited 2023 Nov 13]. Available from: https://onlinelibrary.wiley.com/doi/book/10.1002/9780470209769

19. Zhang X, Li H, Yang J, Lei Y, Wang C, Wang J, et al. Recent advances in Pt-based electrocatalysts for PEMFCs. RSC Adv. 2021 Apr 7;11(22):13316–28.

20. Karanfil G. Importance and applications of DOE/optimization methods in PEM fuel cells: A review. Int J Energy Res. 2020;44(1):4–25.

21. Ghosh PC. High platinum cost: obstacle or blessing for commercialization of low-temperature fuel cell technologies. Clean Technol Environ Policy. 2017 Mar 1;19(2):595–601.

22. Wu J, Liu H, Song Y, Wang Y. A modeling study of PEM fuel cells with novel catalyst monolayers under low platinum loading. J Mater Chem A. 2022 Feb 22;10(8):4076–86.

23. Chong L, Wen J, Kubal J, Sen FG, Zou J, Greeley J, et al. Ultralow-loading platinum-cobalt fuel cell catalysts derived from imidazolate frameworks. Science. 2018 Dec 14;362(6420):1276–81.

24. Bae SY, Mahmood J, Jeon IY, Baek JB. Recent advances in ruthenium-based electrocatalysts for the hydrogen evolution reaction. Nanoscale Horiz. 2020;5(1):43–56.

25. Wang Y, Ruiz Diaz DF, Chen KS, Wang Z, Adroher XC. Materials, technological status, and fundamentals of PEM fuel cells – A review. Mater Today. 2020 Jan 1;32:178–203.

26. Jayakumar A, Sethu SP, Ramos M, Robertson J, Al-Jumaily A. A technical review on gas diffusion, mechanism and medium of PEM fuel cell. Ionics. 2015 Jan 1;21(1):1–18.

27. Tayarani-Yoosefabadi Z, Bellerive J, Kjeang E. Multiscale stochastic modeling of microporous layers and bi-layer gas diffusion media for polymer electrolyte fuel cells. J Power Sources. 2023 Oct 15;581:233476.

28. Kim H, Lee YJ, Park GG, Park SH, Choi YY, Yoo Y. Fabrication of carbon paper containing PEDOT:PSS for use as a gas diffusion layer in proton exchange membrane fuel cells. Carbon. 2015 Apr 1;85:422–8.

29. Zhang X, Ma X, Shuai S, Qin Y, Yang J. Effect of micro-porous layer on PEM fuel cells performance: Considering the spatially variable properties. Int J Heat Mass Transf. 2021 Oct 1;178:121592.

30. US DOE. 3.4 Fuel Cells [Internet]. Multi-Year Research, Development, and Demonstration Plan; 2016. Available from: https://www.energy.gov/sites/prod/files/2016/06/f32/fcto_myrdd_fuel_cells_0.pdf

31. Lim BH, Majlan EH, Daud WRW, Husaini T, Rosli MI. Effects of flow field design on water management and reactant distribution in PEMFC: a review. Ionics. 2016;3(22):301–16.

32. Tang A, Crisci L, Bonville L, Jankovic J. An overview of bipolar plates in proton exchange membrane fuel cells. J Renew Sustain Energy. 2021 Apr 16;13(2):022701.

33. Chen Y. 4D in situ visualization of chemo-mechanical membrane degradation in fuel cells: Understanding and mitigating edge failures [Internet]. Simon Fraser University; 2020 [cited 2023 Nov 15]. Available from: https://summit.sfu.ca/item/20595

34. Li X, Sabir I. Review of bipolar plates in PEM fuel cells: Flow-field designs. Int J Hydrog Energy. 2005 Mar 1;30(4):359–71.

35. Cullen DA, Neyerlin KC, Ahluwalia RK, Mukundan R, More KL, Borup RL, et al. New roads and challenges for fuel cells in heavy-duty transportation. Nat Energy. 2021 May;6(5):462–74.

36. Marcinkoski J, Vijayagopal R, Adams J, James B, Kopasz J, Ahluwalia R. DOE Advanced Truck Technologies. 2019 Oct 31;

37. Papageorgopoulos DD. Fuel Cell Technologies Overview [Internet]. U.S. DOE Hydrogen Program 2023 Annual Merit Review and Peer Evaluation Meeting; 2023 Jun 6; Arlington, VA. Available from: https://www.hydrogen.energy.gov/docs/hydrogenprogramlibraries/pdfs/review23/fc000_papageorgopoulos_2023_o.pdf

38. Ous T, Arcoumanis C. Degradation aspects of water formation and transport in Proton Exchange Membrane Fuel Cell: A review. J Power Sources. 2013 Oct 15;240:558–82.

39. Urchaga P, Kadyk T, Rinaldo SG, Pistono AO, Hu J, Lee W, et al. Catalyst Degradation in Fuel Cell Electrodes: Accelerated Stress Tests and Model-based Analysis. Electrochimica Acta. 2015 Sep 10;176:1500–10.

40. Zhang S, Yuan XZ, Hin JNC, Wang H, Friedrich KA, Schulze M. A review of platinum-based catalyst layer degradation in proton exchange membrane fuel cells. J Power Sources. 2009 Dec 1;194(2):588–600.

41. Mittermeier T, Weiß A, Hasché F, Hübner G, Gasteiger HA. PEM Fuel Cell Start-up/Shut-down Losses vs Temperature for Non-Graphitized and Graphitized Cathode Carbon Supports. J Electrochem Soc. 2016 Dec 31;164(2):F127.

42. Li Y, Moriyama K, Gu W, Arisetty S, Wang CY. A One-Dimensional Pt Degradation Model for Polymer Electrolyte Fuel Cells. J Electrochem Soc. 2015 May 7;162(8):F834.

43. Darling RM, Meyers JP. Kinetic Model of Platinum Dissolution in PEMFCs. J Electrochem Soc. 2003 Sep 25;150(11):A1523.

44. Jahnke T, Futter GA, Baricci A, Rabissi C, Casalegno A. Physical Modeling of Catalyst Degradation in Low Temperature Fuel Cells: Platinum Oxidation, Dissolution, Particle Growth and Platinum Band Formation. J Electrochem Soc. 2019 Nov 27;167(1):013523.

45. Schneider P, Sadeler C, Scherzer AC, Zamel N, Gerteisen D. Fast and Reliable State-of-Health Model of a PEM Cathode Catalyst Layer. J Electrochem Soc. 2019 Mar 7;166(4):F322.

46. Ahluwalia RK, Papadias DD, Kariuki NN, Peng JK, Wang X, Tsai Y, et al. Potential Dependence of Pt and Co Dissolution from Platinum-Cobalt Alloy PEFC Catalysts Using Time-Resolved Measurements. J Electrochem Soc. 2018;165(6):F3024–35.

47. Baroody HA, Kjeang E. Predicting Platinum Dissolution and Performance Degradation under Drive Cycle Operation of Polymer Electrolyte Fuel Cells. J Electrochem Soc. 2021 Apr;168(4):044524.

48. Shojayian M, Kjeang E. Simulation of cathode catalyst durability under fuel cell vehicle operation –Effects of stack size and temperature. J Power Sources. 2024 Jan 30;591:233820.

49. Artyushkova K, Atanassov P, Dutta M, Wessel S, Colbow V. Structural correlations: Design levers for performance and durability of catalyst layers. J Power Sources. 2015 Jun 15;284:631–41.

50. Zhang H, Haas H, Hu J, Kundu S, Davis M, Chuy C. The Impact of Potential Cycling on PEMFC Durability. J Electrochem Soc. 2013;160(8):F840–7.

51. Stiegeler J, Mittermeier T, Tsikonis L, Lehre T, Vierrath S. Influence Factors of Platinum Dissolution in Proton Exchange Membrane Fuel Cells: A Sensitivity Study. J Electrochem Soc. 2024 May 1;171(5):054517.

52. Messing M. Empirical Modeling of Fuel Cell Durability: Cathode Catalyst Layer Degradation [Internet]. Simon Fraser University; 2017 [cited 2023 Nov 15]. Available from: https://summit.sfu.ca/item/17810

53. Kregar A, Gatalo M, Maselj N, Hodnik N, Katrašnik T. Temperature dependent model of carbon supported platinum fuel cell catalyst degradation. J Power Sources. 2021 Dec 1;514:230542.

54. Bi W, Fuller T. Temperature Effects on PEM Fuel Cells Pt/C Catalyst Degradation. ECS Trans. 2007 Sep 28;11(1):1235.

55. Debe MK, Schmoeckel AK, Vernstrom GD, Atanasoski R. High voltage stability of nanostructured thin film catalysts for PEM fuel cells. J Power Sources. 2006 Oct 27;161(2):1002–11.

56. Holby EF, Shao-Horn Y, Sheng W, Morgan D. New Understanding of Pt Surface Area Loss in PEMFC's: Temperature Effects. ECS Trans. 2010 Oct 1;33(1):369.

57. Coppo M, Siegel NP, Spakovsky MR von. On the influence of temperature on PEM fuel cell operation. J Power Sources. 2006 Sep 13;159(1):560–9.

58. Bi W, Sun Q, Deng Y, Fuller TF. The effect of humidity and oxygen partial pressure on degradation of Pt/C catalyst in PEM fuel cell. Electrochimica Acta. 2009 Feb 15;54(6):1826–33.

59. Bella RKFD, Stühmeier BM, Gasteiger HA. Universal Correlation between Cathode Roughness Factor and H2/Air Performance Losses in Voltage Cycling-Based Accelerated Stress Tests. J Electrochem Soc. 2022 Apr;169(4):044528.

60. Zihrul P, Hartung I, Kirsch S, Huebner G, Hasché F, Gasteiger HA. Voltage Cycling Induced Losses in Electrochemically Active Surface Area and in H2/Air-Performance of PEM Fuel Cells. J Electrochem Soc. 2016 Mar 9;163(6):F492.

61. Topalov AA, Katsounaros I, Auinger M, Cherevko S, Meier JC, Klemm SO, et al. Dissolution of Platinum: Limits for the Deployment of Electrochemical Energy Conversion? Angew Chem Int Ed. 2012;51(50):12613–5.

62. Borup RL, Davey JR, Garzon FH, Wood DL, Inbody MA. PEM fuel cell electrocatalyst durability measurements. J Power Sources. 2006 Dec 7;163(1):76–81.

63. Paik CH, Saloka GS, Graham GW. Influence of Cyclic Operation on PEM Fuel Cell Catalyst Stability. Electrochem Solid-State Lett. 2006 Dec 13;10(2):B39.

64. Messing M, Kjeang E. Empirical modeling of cathode electrode durability in polymer electrolyte fuel cells. J Power Sources. 2020 Mar 1;451:227750.

65. Uchimura M, Sugawara S, Suzuki Y, Zhang J, Kocha SS. Electrocatalyst Durability under Simulated Automotive Drive Cycles. ECS Trans. 2008 Oct 3;16(2):225.

66. Bernhard D, Kadyk T, Krewer U, Kirsch S. How platinum oxide affects the degradation analysis of PEM fuel cell cathodes. Int J Hydrog Energy. 2021 Apr 14;46(26):13791–805.

67. Kneer A, Wagner N, Sadeler C, Scherzer AC, Gerteisen D. Effect of Dwell Time and Scan Rate during Voltage Cycling on Catalyst Degradation in PEM Fuel Cells. J Electrochem Soc. 2018 Jul 18;165(10):F805.

68. Young AP, Colbow V, Harvey D, Rogers E, Wessel S. A Semi-Empirical Two Step Carbon Corrosion Reaction Model in PEM Fuel Cells. J Electrochem Soc. 2013 Feb 8;160(4):F381.

69. Uchimura M, Kocha SS. The Impact of Cycle Profile on PEMFC Durability. ECS Trans. 2007 Sep 28;11(1):1215.

70. Shojayian MS. Simulation of catalyst layer and membrane durability in polymer electrolyte membrane fuel cells under real-world vehicle operation [Internet]. Simon Fraser University; 2024 [cited 2024 Jul 14]. Available from: https://summit.sfu.ca/item/38069

71. Pei P, Chang Q, Tang T. A quick evaluating method for automotive fuel cell lifetime. Int J Hydrog Energy. 2008 Jul 1;33(14):3829–36.

72. Breitwieser M, Klingele M, Britton B, Holdcroft S, Zengerle R, Thiele S. Improved Pt-utilization efficiency of low Pt-loading PEM fuel cell electrodes using direct membrane deposition. Electrochem Commun. 2015 Nov 1;60:168–71.

73. Sassin MB, Garsany Y, Gould BD, Swider-Lyons KE. Fabrication Method for Laboratory-Scale High-Performance Membrane Electrode Assemblies for Fuel Cells. Anal Chem. 2017 Jan 3;89(1):511–8.

74. Serpico JM, Ehrenberg SG, Wnek GE, Tangredi TN. Gas diffusion electrode [Internet]. US5677074A, 1997 [cited 2023 Nov 15]. Available from: https://patents.google.com/patent/US5677074A/en

75. Liu W, Wan L, Liu J, Zhao M, Zou Z. Performance improvement of the open-cathode proton exchange membrane fuel cell by optimizing membrane electrode assemblies. Int J Hydrog Energy. 2015 Jun 15;40(22):7159–67.

76. Britton B, Holdcroft S. The Control and Effect of Pore Size Distribution in AEMFC Catalyst Layers. J Electrochem Soc. 2016 Jan 27;163(5):F353.

77. Yuan XZ, Zhang S, Sun JC, Wang H. A review of accelerated conditioning for a polymer electrolyte membrane fuel cell. J Power Sources. 2011 Nov 15;196(22):9097–106.

78. Ann R Cannon author. STAT2: modeling with regression and ANOVA / Ann R. Cannon, George W. Cobb, Bradley A. Hartlaub, Julie M. Legler, Robin H. Lock, Thomas L. Moore, Allan J. Rossman, Jeffrey A. Witmer. [Internet]. Second edition. W. H. Freeman; 2019 [cited 2024 May 7]. Available from: https://ebookcentral.proquest.com/lib/sfu-ebooks/detail.action?docID=6643881

79. Wang P, Liu H, Hou M, Zheng L, Yang Y, Geng J, et al. Estimating the Remaining Useful Life of Proton Exchange Membrane Fuel Cells under Variable Loading Conditions Online. Processes. 2021 Aug;9(8):1459.

80. Kurtz JM, Sprik S, Saur G, Onorato S. Fuel Cell Electric Vehicle Durability and Fuel Cell Performance [Internet]. 2019 Mar [cited 2024 Mar 13] p. NREL/TP--5400-73011,

1501675. Report No.: NREL/TP--5400-73011, 1501675. Available from: http://www.osti.gov/servlets/purl/1501675/

81. Ao Y, Laghrouche S, Depernet D, Chen K. Lifetime prediction for proton exchange membrane fuel cell under real driving cycles based on platinum particle dissolve model. Int J Hydrog Energy. 2020 Nov 13;45(56):32388–401.

82. Hiraoka F, Kohno Y, Matsuzawa K, Mitsushima S. A Simulation Study of Pt Particle Degradation During Potential Cycling Using a Dissolution/Deposition Model. Electrocatalysis. 2015 Jan 1;6(1):102–8.

83. Kneer A, Jankovic J, Susac D, Putz A, Wagner N, Sabharwal M, et al. Correlation of Changes in Electrochemical and Structural Parameters due to Voltage Cycling Induced Degradation in PEM Fuel Cells. J Electrochem Soc. 2018 Mar 31;165(6):F3241.

84. Hasché F, Oezaslan M, Strasser P. Activity, Stability, and Degradation Mechanisms of Dealloyed PtCu3 and PtCo3 Nanoparticle Fuel Cell Catalysts. ChemCatChem. 2011;3(11):1805–13.

85. Zhang J, Litteer BA, Gu W, Liu H, Gasteiger HA. Effect of Hydrogen and Oxygen Partial Pressure on Pt Precipitation within the Membrane of PEMFCs. J Electrochem Soc. 2007 Aug 8;154(10):B1006.

86. Ferreira PJ, O' GJ la, Shao-Horn Y, Morgan D, Makharia R, Kocha S, et al. Instability of Pt／C Electrocatalysts in Proton Exchange Membrane Fuel Cells: A Mechanistic Investigation. J Electrochem Soc. 2005 Oct 7;152(11):A2256.

87. Guilminot E, Corcella A, Charlot F, Maillard F, Chatenet M. Detection of Pt z + Ions and Pt Nanoparticles Inside the Membrane of a Used PEMFC. J Electrochem Soc. 2006 Dec 1;154(1):B96.

88. Sgarbi R, Idir WA, Labarde Q, Mermoux M, Wu P, Mainka J, et al. Does the platinum-loading in proton-exchange membrane fuel cell cathodes influence the durability of the membrane-electrode assembly? Ind Chem Mater. 2023 Oct 20;1(4):501–15.

89. Mayrhofer KJJ, Strmcnik D, Blizanac BB, Stamenkovic V, Arenz M, Markovic NM. Measurement of oxygen reduction activities via the rotating disc electrode method: From Pt model surfaces to carbon-supported high surface area catalysts. Electrochimica Acta. 2008 Feb 25;53(7):3181–8.

90. Gasteiger HA, Kocha SS, Sompalli B, Wagner FT. Activity benchmarks and requirements for Pt, Pt-alloy, and non-Pt oxygen reduction catalysts for PEMFCs. Appl Catal B Environ. 2005 Mar 10;56(1):9–35.

91. Kinoshita K. Particle Size Effects for Oxygen Reduction on Highly Dispersed Platinum in Acid Electrolytes. J Electrochem Soc. 1990 Mar 1;137(3):845.

92. Antoine O, Durand R. RRDE study of oxygen reduction on Pt nanoparticles inside Nafion®: H2O2 production in PEMFC cathode conditions. J Appl Electrochem. 2000 Jul 1;30(7):839–44.

93. Park JH, Yim SD, Kim T, Park SH, Yoon YG, Park GG, et al. Understanding the mechanism of membrane electrode assembly degradation by carbon corrosion by analyzing the microstructural changes in the cathode catalyst layers and polarization losses in proton exchange membrane fuel cell. Electrochimica Acta. 2012 Nov 30;83:294–304.

94. Li S, Wei X, Dai H, Yuan H, Ming P. Voltammetric and galvanostatic methods for measuring hydrogen crossover in fuel cell. iScience. 2022 Jan 21;25(1):103576.

95. Shojayian MS. Simulation of catalyst layer and membrane durability in polymer electrolyte membrane fuel cells under real-world vehicle operation [Internet]. Simon Fraser University; 2024 [cited 2024 Jun 24]. Available from: https://summit.sfu.ca/item/38069

96. Liu G, Peng S, Hou F, Wang X, Fang B. Preparation and Performance Study of the Anodic Catalyst Layer via Doctor Blade Coating for PEM Water Electrolysis. Membranes. 2023 Jan;13(1):24.

97. Patil GC. Doctor Blade: A Promising Technique for Thin Film Coating. In: Sankapal BR, Ennaoui A, Gupta RB, Lokhande CD, editors. Simple Chemical Methods for Thin Film Deposition: Synthesis and Applications [Internet]. Singapore: Springer Nature; 2023 [cited 2024 May 7]. p. 509–30. Available from: https://doi.org/10.1007/978-981-99-0961-2_12

98. Garrick TR, Moylan TE, Carpenter MK, Kongkanand A. Editors' Choice—Electrochemically Active Surface Area Measurement of Aged Pt Alloy Catalysts in PEM Fuel Cells by CO Stripping. J Electrochem Soc. 2016 Dec 13;164(2):F55.

99. Stühmeier BM, Pietsch MR, Schwämmlein JN, Gasteiger HA. Pressure and Temperature Dependence of the Hydrogen Oxidation and Evolution Reaction Kinetics on Pt Electrocatalysts via PEMFC-based Hydrogen-Pump Measurements. J Electrochem Soc. 2021 Jun;168(6):064516.

100. Aroge FA, Halter J, Lowe OC, MacDonald JA, Orfino FP, Dutta M, et al. Interactions between Catalyst Layer Degradation and Liquid Water Distribution in Polymer Electrolyte Fuel Cells. ECS Meet Abstr. 2023 Dec 22;MA2023-02(37):1787.

Appendix A.

Pt Degradation Model

In order to simulate the ECSA decay over time due to Pt degradation, Pt dissolution and redeposition, formation and removal of oxide coverage over Pt surface, and Pt ion generation during fuel cell ASTs were modeled using the Butler-Volmer kinetic approach presented in (43). The rate equation for each reaction specified above is utilized as follows:

Table A. 1. The rate equations for the Pt degradation reactions

Reaction rate equation	Description	Equation number
$r_{dis} = k_{dis}(T)(1 - \theta_{PtO}(r))\left[exp\left(\frac{\alpha_a nF}{RT}(\varphi(t) - \varphi_{dis}(r))\right) - k_r \frac{c_{Pt^{2+}}}{c_{Pt^{2+},ref}} exp\left(\frac{-\alpha_c nF}{RT}(\varphi(t) - \varphi_{dis}(r))\right)\right]$	Electrochemical Pt dissolution and redeposition	A. 1.
$r_{cdis} = k_{cdis}\theta_{PtO}\left(\frac{c_{H^+}}{c_{H^+,ref}}\right)^2$	Chemical Pt dissolution and redeposition	A. 2.
$r_{ox} = k_{ox}(T)\left[exp\left(-\frac{\omega\theta_{PtO}(r)}{RT}\right) exp\left(\frac{\alpha_a nF}{RT}(\varphi(t) - \varphi_{ox}(r))\right) - k_{ox,r}\theta_{PtO}(r)\left(\frac{c_{H^+}}{c_{H^+,ref}}\right)^2 exp\left(\frac{-\alpha_c nF}{RT}(\varphi(t) - \varphi_{ox}(r))\right)\right]$	Oxide coverage formation and removal	A. 3.

Next, the mass balance for different species should be used as follows to obtain the governing differential equations.

Table A. 2. The mass balance equations for different species in the Pt degradation model

Reaction rate equation	species	Equation number

$\frac{dr}{dt} = -\frac{M_{Pt}}{\rho_{Pt}}(r_{dis} + r_{cdis})$	Pt	A. 4.
$\frac{d\theta_{PtO}}{dt} = \left(\frac{r_{ox} - r_{cdis}}{\Gamma_{max}}\right) - \left(\frac{2\theta_{PtO}}{r}\right)\frac{dr}{dt}$	PtO	A. 5.
$\frac{dc_{Pt^{2+}}}{dt} = -\frac{m_v}{M_{Pt}}\left(\frac{dM_{dis}}{dt} - \frac{dM_{cdis}}{dt}\right)$	Pt ions	A. 6.

Then, the updated normalized ECSA at any time was calculated by treating the Pt catalyst as an ensemble of particle sizes and integrating the collective surface area as

$$\frac{ECSA(t)}{ECSA(0)} = \frac{\int_0^\infty r^2 f_N(r,t)dr}{\int_0^\infty r^2 f_N(r,0)dr} \quad \text{A. 7.}$$

The developed Pt degradation model has been rigorously validated with a variety of operating conditions including different UPLs, LPLs, temperatures, and potential cycles. The reader is referred to Ref. (48) for the details of the model and the validation results.